Functional characterization of *Arabidopsis thaliana* ROP GTPase activating proteins during cell division and pavement cell morphogenesis

Dissertation

der Mathematisch-Naturwissenschaftlichen Fakultät

der Eberhard Karls Universität Tübingen

zur Erlangung des Grades eines

Doktors der Naturwissenschaften

(Dr. rer. nat.)

vorgelegt von

Theresa Lauster

aus Kirchheim unter Teck

Tübingen

2021

Gedruckt mit Genehmigung der Mathematisch-Naturwissenschaftlichen Fakultät der Eberhard Karls Universität Tübingen.

Tag der mündlichen Qualifikation:	17.05.2021
Dekan:	Prof. Dr. Thilo Stehle
1. Berichterstatter:	Dr. Sabine Müller
2. Berichterstatter:	Prof. Dr. Gerd Jürgens

Danksagung

Vielen Dank Sabine, dass du mir nach meine Bachelor- und Masterarbeit auch noch die Chance gegeben hast bei dir zu promovieren und für all deine Unterstützung während der ganzen Zeit. Ich habe sehr viel von dir gelernt.

Danke Gerd das du die Zweitkorrektur meiner Arbeit übernommen hast und für die ganzen Tipps und Kommentare während meiner TAC Meetings.

Mein Dank geht auch an dich Steffi, danke, dass du immer an mich geglaubt hast und für mich da warst. Durch dich war immer gute Laune im Labor und mir wird es fehlen dich zu ärgern, was mit großer Wahrscheinlichkeit auf Gegenseitigkeit beruht. :) Wenn es sein muss, darfst du mich auch weiterhin Theresi nennen, nicht dass ich eine Wahl hätte….

Mein Dank geht auch an dich Pantelis, für deine ganze Unterstützung und große Hilfsbereitschaft. Auch wenn du immer viel um die Ohren hattest, konnte ich jeder Zeit zu dir kommen.

Danke natürlich auch an die ganze Entgen, meine Familien, mein Freund (der lange warten musste, aber ich bin dann jetzt endlich mal fertig :P) und alle Leute, die mich auf dem Weg zur Promotion unterstützt haben.

Zum Schluss noch ein spezieller Dank an dich Ron (alias Daniel), dass du mich jeden Tag aufs Neue motiviert hast den mit dir vereinbarten „Arbeitsplan zum Schreiben der Doktorarbeit“ auch einzuhalten^^

Table of contents

1. Zusammenfassung 1
2. Summary 3
3. List of publications 5
4. Personal contribution 6
5. Introduction 7
5.1 The plant cytoskeleton 7
5.2 Plant cell division 9
5.3 Pavement cell shape formation 10
5.4 *Arabidopsis* GTPase activating proteins 14
6. Objectives 18
7. Results and Discussion 19
7.1 Functional characterization of PHGAP1 and PHGAP2 in cell division 19
Discussion 29
7.2 Characterization of PHGAP functions during pavement cell shape establishment 34
8. Material and Methods 60
9. References 74
10. Appendix 83

1. Zusammenfassung

Zellteilung und Zellexpansion sind essentielle Prozesse in der Pflanzenentwicklung. Auch wenn die Funktionsweisen vieler Proteine in diesen Prozessen bereits charakterisiert wurden, gibt es immer noch viel zu erforschen. Zu Beginn der pflanzlichen Zellteilung markiert das Präprophaseband, ein Ring aus kortikalen Mikrotubuli, die zukünftige Zellteilungsebene. Die Position des Präprophasebandes dient in der letzten Phase der Zellteilung, der sogenannten Zytokinese, als Fusionsstelle der Zellplatte. Die zentrifugal wachsende Zellplatte wird von dem ebenfalls expandierenden Phragmoplast, bestehend aus bipolar angeordneten antiparallelen Mikrotubuli, vom Zentrum der Zelle zur Zellperipherie geführt und an der Fusionstelle mit der Parentalwand vereint. Allerdings wird das Präprophaseband schon vor der Metaphase wieder abgebaut. Zuvor werden Proteine wie das PHRAGMOPLAST ORIENTIERTE KINESIN 1 (POK1) am Präprophaseband angelagert und die Zellteilungsseite etabliert, die nun die positionelle Information der zukünftigen Zellteilungsebene auch während der Mitose und Zytokinese erhalten. In der vorliegenden Studie, identifizierten wir zwei *Arabidopsis thaliana* Pleckstrin Homologie Domäne enthaltende GTPase aktivierende Proteine, PHGAP1 und PHGAP2, als Interaktionspartner von POK1, eine der wichtigsten Komponenten der kortikalen Zellteilungsseite. Anders als POK1, das nur in teilungsaktiven Zellen vorzufinden ist, lokalisierten die PHGAPs in Interphase Zellen an der Plasmamembran und im Zytoplasma und begannen sich während der Metaphase POK-abhängig an der Zellteilungsebene anzureichern, wo sie bis zum Ende der Zytokinese verblieben. Weitere Experimente führten zu der Erkenntnis, dass PHGAP carboxy-terminale Fragmente, bestehend aus coiled coil Domänen, für Funktion und Lokalisation an der Zellteilungsebene wichtig waren. Weiterführende Interaktionsstudien und die Analyse von PHGAP Phospho-Mutanten deuteten darauf hin, dass die temporale Lokalisation von PHGAPs an der Zellteilungsebene von deren Phospho-Regulierung abhängig war. Überlappende Expressionsmuster von PHGAP1 und PHGAP2 und die Abwesenheit auffälliger Einzelmutanten Phänotypen wies auf deren redundante Funktionen hin. Die Analyse teilungsaktiver Zellen in der *phgap1 phgap2* Doppeltmutanten ergaben eine fehlerhafte Ausrichtung von Präprophasebändern und konsequenterweise Phragmoplasten, was auf eine Funktion von PHGAPs in der Präprophaseband Orientierung hindeutete. Allgemein sind GAPs dafür bekannt die Inaktivierung von Rho von Pflanzen (ROP) herbeizuführen, indem sie die Guanosintriphosphat (GTP) Hydrolyse dieser Signalproteine stimulieren. *In vivo* Interaktionsstudien ergaben, dass PHGAPs mit verschiedenen ROPs interagieren konnten, was den ersten Hinweis dafür liefert, dass nicht nur PHGAPs, sondern auch ROPs möglicherweise eine Rolle während der Zellteilung im Wurzelmeristem spielen.

Der zweite Teil dieser Arbeit beschreibt funktionelle Aspekte von PHGAP1 und PHGAP2 vermittelter Zellpolarität während der Entwicklung der Blattepidermiszellen. Für deren charakteristische Puzzleteil-artige Form sind zwei antagonistisch wirkende ROP-Signaltransduktionswege verantwortlich, die Zellpolarität etablieren und damit Wachstumsrichtungen bestimmen. In *phgap1 phgap2* Doppeltmutanten waren die sonst deutlich polarisierten Ein- und Ausbuchtungen der Epidermiszellen stark reduziert, was auf eine fehlerhafte Steuerung der oben angeführten ROP-Aktivitäten in *phgap1 phgap2* Doppeltmutanten hindeutete. Untersuchungen zeigten Interaktion von PHGAP2 und ROP2 und erhöhte Aktivität von ROP2 in *phgap1 phgap2* Doppeltmutanten. Diese Daten wiesen darauf hin, dass während der Epidermiszellentwicklung PHGAPs die ROP2 GTP-Hydrolyse stimulieren, was zur Deaktivierung von ROP führt. Eine detaillierte Lokalisations-Analyse zeigte eine Mikrotubuli-abhängige Anreicherung beider PHGAPs an den antiklinalen Seiten von Epidermiszell-Einbuchtungen. Die Menge an angereicherten PHGAPs in Einbuchtungen nahm mit deren Entwicklung zu, was in Korrelation mit einer zunehmenden Fläche steht in der die ROP2 Aktivität inhibiert werden muss, um die Zellpolarität aufrechtzuerhalten. Auch in Blattepidermiszellen zeigte sich der PHGAP carboxy-terminus für die Lokalisation an der antiklinalen Ansicht der Einbuchtungen verantwortlich. Eine Punktmutation in der PHGAP GTPase aktivierenden Protein Domäne beseitigte die Funktion der PHGAP Proteine zwar vollständig, hatte aber keinen Einfluss auf das spezifische Lokalisationsmuster. Insgesamt zeigen die Daten in dieser Arbeit wichtige Rollen der PHGAPs während der Zellteilung und während der Etablierung von Zellpolarität, die die zelluläre Morphogenese vorantreiben.

2. Summary

Cell division and cell expansion are fundamentally important processes of plant development. Although, many proteins have been functionally characterized and implicated in those processes, there is still a lot to investigate. In plant cell division, the future division site is marked by the preprophase band, a belt of cortical microtubules. In the final phase of cell division, called cytokinesis, serves the position of the preprophase band as fusion site of the cell plate. The centrifugal growing cell plate is guided by the expanding phragmoplast, a set of bipolar microtubules, from the centre towards the cell periphery and connects at the fusion site with the parental cell wall. However, the preprophase band is disassembled before metaphase. Prior to this, proteins such as the PHRAGMOPLAST ORIENTING KINESIN 1 (POK1) are recruited to the preprophase band to establish the division site and mark the future division plane throughout mitosis and cytokinesis. In the present thesis, we identified two *Arabidopsis thaliana* pleckstrin homology domain containing GTPase activating proteins, PHGAP1 and PHGAP2, as interaction partners of POK1, a core component of the cortical division site. Unlike POK1, which is only present in dividing cells, PHGAPs were localized at the plasma membrane and in the cytoplasm in interphase cells and started to accumulate in a POK-dependent manner at the division site during metaphase, where they remained till the end of cytokinesis. Further experiments revealed that the PHGAP carboxyl-terminus, containing coiled coil domain, was required for division site accumulation and function. Additionally, interactions studies and PHGAP phospho-mutant analysis suggested that the timely localization of PHGAPs at the division site was phospho-regulated. Overlapping expression patterns of PHGAP1 and PHGAP2 and a lack of single mutant phenotypes pointed to redundant functions. Analysis of *phgap1 phgap2* dividing double mutant cells revealed that preprophase bands and consequently phragmoplasts were misaligned, implicating a function of PHGAPs in preprophase band orientation. In general, PHGAPs are known to mediate Rho of plant (ROP) inactivation by stimulating the guanosine triphosphate (GTP) hydrolysis function of these signal proteins. *In vivo* interaction studies uncovered that PHGAPs were able to interact with several ROPs, providing the first evidence that not only PHGAPs but also ROP activity might play a role during root cell division.

The second part of this thesis describes functional aspects of PHGAP1 and PHGAP2 mediated cell polarity during pavement cell shape establishment. Two antagonistic ROP signal transduction pathways are responsible for their characteristic jigsaw puzzle form, involving the establishment of cell polarity and thereby determining growth direction. The distinct polarized lobe and indentation regions of epidermis cells, where drastically reduced in *phgap1 phgap2* double mutants, which pointed to miss regulation of the above mentioned ROP activity in *phgap1 phgap2*. Investigations revealed interaction of PHGAP2 with ROP2 and increased

ROP2 activity in *phgap1 phgap2* double mutants. These data indicated that PHGAPs stimulate ROP2 GTP-hydrolysis, leading in ROP inactivation during pavement cell development. Analysis of localization pattern uncovered that both PHGAPs accumulate in a microtubule-dependent manner on the anticlinal face in indentation regions. The amount of PHGAP accumulation in indentation regions increased with their development, which correlates with an increasing surface that has to be free of ROP2 activity to maintain cell polarity. Also in leaf pavement cells was the carboxyl-terminal domain of PHGAPs necessary for anticlinal face localization in indentation regions. A point mutation in the PHGAP GTPase activating domain abolished PHGAP function completely, but had no effect on the distinct localization pattern. Collectively, the data of this thesis describe significant roles for PHGAPs on the mechanisms orchestrating cell division and cell polarity establishment that promote cellular morphogenesis.

3. List of publications

Research article:

Putative RopGAPs impact division plane selection and interact with kinesin-12 POK1

Dorothee Stöckle, Arvid Herrmann, Elisabeth Lipka, **Theresa Lauster**, Richard Gavidia, Steffi Zimmermann and Sabine Müller

Nat Plants. 2016 Aug 8; 2:16120. doi: 10.1038/nplants.2016.120. PMID: 27501519.

Manuscript:

Cell polarity establishment requires spatial localization of GTPase activating proteins

Theresa Lauster, Dorothee Stöckle and Sabine Müller

4. Personal contribution

4.1 Putative RopGAPs impact division plane selection and interact with kinesin-12 POK1 (Stöckle et al., 2016)

In this research article, I performed the GUS reporter experiments for PHGAP2 and analysed the expression pattern in different tissues as part of my bachelor thesis (Figure S3). Furthermore, I was involved in the preparation of the immunolocalization samples used for the analysis of preprophase band and phragmoplast orientation in *phgap1 phgap2* and wild type root meristem (Figure 4).

4.2 Cell polarity establishment requires spatial localization of GTPase activating proteins (Lauster et al., in preparation)

In the manuscript, I performed all experiments, statistical analysis and established analysis methods in cooperation with Sabine Müller, with some exceptions. Dorothee Stöckle conducted the expression analysis in Figure S1. Pia Lotz performed the pavement cell analysis of *phgap1-1* and *phgap2-1* single and double mutants as part of her bachelor thesis under my supervision (Figure S1). Most of the final gene constructs were cloned by me or former lab members as indicated (Material and Methods). I wrote the initial draft and designed the initial figures.

5. Introduction

5.1 The plant cytoskeleton

The plant cytoskeleton consists of microtubules and actin filaments with important functions in many biological processes such as cell division and (polarized) growth. Microtubules consist of α- and β-tubulin heterodimers that assemble head-to-tail into long oligomers called protofilaments. Most commonly, thirteen of these protofilaments associate laterally forming a sheet that closes and becomes a hollow tube with a diameter of ~25 nm and variable length ranging from <1 µm up to >100 µm (Figure 1A, reviewed by Goodson and Jonasson, 2018). Microtubules are polar and have a dynamic plus end (exposed β-tubulin) and a less dynamic minus end (exposed α-tubulin). Growth (polymerization) of the highly dynamic microtubule plus ends occurs with a speed of 3-5 µm/min by addition of heterodimers (Vos et al., 2004). Guanosine triphosphate (GTP) bound αβ-tubulin heterodimers are added to the growing microtubule end and a delay in GTP-hydrolysis and phosphate release generates a GTP-rich cap. Older parts of the microtubule consist of guanosine diphosphate (GDP) bound β-tubulin, generated through GTP-hydrolysis (reviewed by Goodson and Jonasson, 2018). The GTP-rich cap stabilizes the protofilaments in the tubular form. Loss of the GTP-cap results in rapid depolymerisation (5-9 µm/min) of microtubule protofilaments, also known as shrinking (Goodson and Jonasson, 2018; Vos et al., 2004). The phase transition from growth to shrinking is termed catastrophe, whereas transitioning from shrinking to growth is referred to as rescue (Goodson and Jonasson, 2018). This behaviour is collectively described as dynamic instability of microtubules (Mitchison and Kirschner, 1984). Mechanisms that modulate microtubule nucleation or organization involve protein complexes, microtubule zippering at distinct angles, catastrophe upon contact or microtubule severing (Dixit and Cyr, 2004; Job et al., 2003; Lin et al., 2013; Martinez et al., 2020). A protein complex that is involved in the polymerization of new microtubules is the γ-tubulin ring complex (γ-TuRC), a nucleation machinery that serves as template for microtubule assembly and as minus end cap (Goodson and Jonasson, 2018; Job et al., 2003). Depending on the collusion angle, an encounter between two microtubules ends either in microtubule zippering (<40°) or in microtubule catastrophe/crossover (>40°) (Dixit and Cyr, 2004). Microtubule severing is mediated by katanin that severs existing microtubules at their branching points resulting in microtubule bundling (Lin et al., 2013).

Actin filaments consist of two helical actin polymer chains and have a diameter of ~7 nm (Figure 1B). Like the microtubule ends, the actin filament ends exhibit different assembly speeds. The faster growing end is termed barbed end, while the slower growing end is referred to as pointed end. Actin filament assembly can be separated in two steps, nucleation and elongation (Pollard and Cooper, 1986). During nucleation, actin monomers are assembled in dimers followed by trimer formation (Pollard et al., 2000). These unstable trimers are the

starting point for actin filament elongation, by the addition of adenosine triphosphate (ATP)-loaded actin monomers (Blanchoin et al., 2010; Pollard et al., 2000). After actin monomers are associated with the actin filament on the barbed end, ATP hydrolysis, followed by the release of inorganic phosphate occurs and generates depolymerisation susceptible adenosine diphosphate (ADP)-bound actin monomers at the pointed end (reviewed by Blanchoin et al., 2010).

Microtubules and actin filaments are able to disassemble on one end to sustain material for polymerisation on the opposite end, a process which is referred to as treadmilling (Neuhaus et al., 1983; Rodionov and Borisy, 1997). This dynamic microtubule and actin filament behaviour allows fast reorganization into bundles, arrays or mitotic structures (Mineyuki and Palevitz, 1990; Pickett-Heaps, 1969; Shaw et al., 2003; Staiger et al., 2009; Thomas et al., 2009).

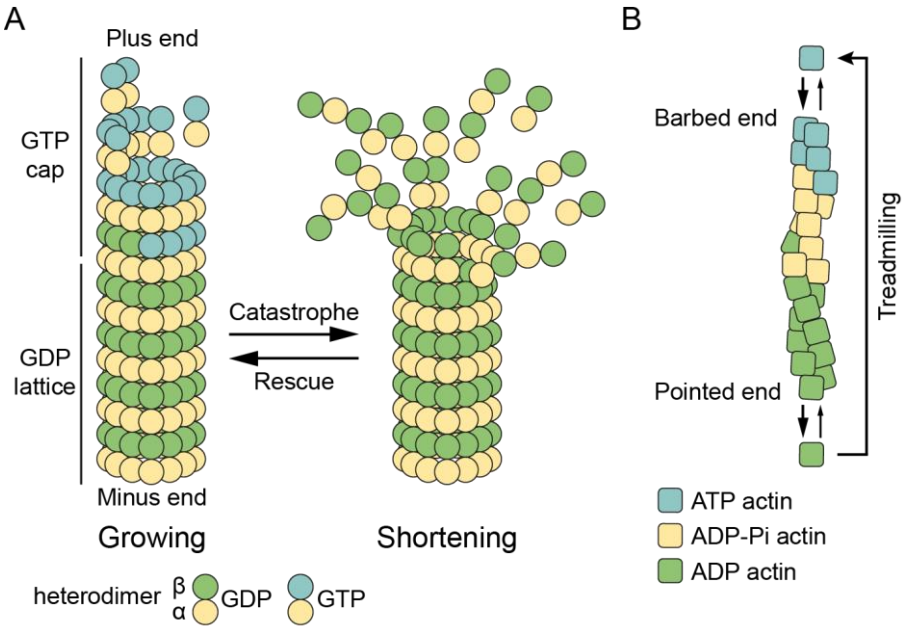

Figure 1: Microtubule and actin filament organization

(A) Microtubules are composed of 13 protofilaments forming a hollow tube. Subunits are heterodimers of α- and β-tubulin. Microtubules are polar structures with a fast growing plus end and a slow growing minus end by addition of heterodimers. The growing microtubule end contains a GTP-rich cap, GTP loaded α- and β-tubulin, while the "older" microtubule lattice comprises of GDP-bound β-tubulin (GDP lattice). Loss of the GTP-rich cap, results in rapid microtubule depolymerisation (shrinking). Transition between growth and shortening are termed catastrophe and rescue. (B) Actin filaments are consisting of two helical actin polymer chains, with a fast-growing barbed end (blue) and a slow-growing pointed end (green). Actin filaments elongate with the addition of ATP-bound actin monomers, followed by ATP hydrolysis and inorganic phosphate (Pi) release, generating depolymerisation susceptible ADP-bound actin monomers. Treadmilling describes the depolymerisation on one end of the filament to sustain grow on the other end. (Modified from Blanchoin et al., 2010; Goodson and Jonasson, 2018).

5.2 Plant cell division

Cell division is a fundamentally important process. Cells are divided either symmetrically, generating two equally formed daughter cells with identical fate or asymmetrically developing daughter cells with different size and fate, allowing the formation of specialized cell types and organs (Lipka et al., 2015). The cytoskeleton plays a major role during cell division and is part of the different mitotic structures. In addition to the spindle apparatus, which is common among eukaryotes, plant cells form two unique cytoskeletal structures during cell division, the preprophase band (PPB) and the phragmoplast (Pickett-Heaps, 1969; Staehelin and Hepler, 1996). In symmetrically dividing cells the nucleus migrates to the centre of the cell, followed by the formation of the belt-like PPB, that mark the future division site and consist of cortical microtubules and actin filaments (Figure 2, Pickett-Heaps, 1969; Smertenko et al., 2017). In prophase, the pro-spindle a bipolar structure is formed by the reorientation of perinuclear microtubules and the PPB is disassembled at the end of prophase (Masoud et al., 2013; Pickett-Heaps and Northcote, 1966). After nuclear envelope break down, the spindle apparatus emerges from the pro-spindle during metaphase and the chromosomes are aligned in the spindle mid zone (Masoud et al., 2013). The anaphase spindle separates the chromosomes and in telophase the phragmoplast an array of anti-parallel microtubules, actin filaments and associated endomembranes, starts to form (Müller and Jürgens, 2016; Smertenko et al., 2017; Staehelin and Hepler, 1996). During cytokinesis, the phragmoplast starts to expand from the centre of the cell towards the cell wall. Golgi-derived vesicles, containing cell plate biosynthesis material are transported along the microtubules towards the phragmoplast mid zone to form the new cell plate via vesicle fusion (Lipka et al., 2015; Müller and Jürgens, 2016). The phragmoplast is disassembled and cell division is terminated, after cell plate fusion with the parental cell wall.

To set up the PPB, microtubule associated proteins (MAPs), microtubule nucleation components and the protein phosphatase TTP complex are critical (Janski et al., 2012; Pastuglia et al., 2006; Spinner et al., 2013). The TTP complex consists of a heterotrimeric protein phosphatase 2A (PP2A) containing a variable scaffolding subunit A, the regulatory FASS B subunit and a variable catalytic C subunit, as well as TONNEAU 1 (TON1) and the variable TON1 RECRUITING MOTIF (TRM) that mediates cytoskeletal targeting of the complex (Camilleri et al., 2002; Drevensek et al., 2012; Spinner et al., 2013). The TTP complex likely regulates MAP activity (Lipka et al., 2015). Mutation of TTP complex components resulted in a lack of PPB formation and more or less severe division plane orientation defects (Schaefer et al., 2017; Spinner et al., 2013; Torres-Ruiz and Jürgens, 1994; Traas et al., 1995). Before PPB disassembly a number of division site resident proteins, TANGLED (TAN), the PHRAGMOPLAST ORIENTING KINESIN (POK) 1, POK2 and RanGAP1 begin to accumulate at the division site and potentially finalize the setup of the cortical division zone (CDZ), a cortical

region that preserves the positional information of the selected division plane throughout mitosis and cytokinesis (Herrmann et al., 2018; Lipka et al., 2014; Müller et al., 2006; Walker et al., 2007; Xu et al., 2008). These division site markers remain at the CDZ until the end of cytokinesis. However, the CDZ including TAN, POK1, POK2 and RanGAP1 narrows to the cell plate fusion site (CPFS) during telophase (Smertenko et al., 2017). POK1, POK2, TAN and other CDZ markers are proposed to guide the phragmoplast towards the cortical division site in late cytokinesis, ensuring the insertion of the new cell plate at the position predicted by the PPB/CDZ (Müller and Jürgens, 2016). Loss of POKs or TAN function caused phragmoplast misguidance and consequently miss positioned cell walls (Cleary and Smith, 1998; Lipka et al., 2014; Müller et al., 2006). In addition to the CDZ localization, POK2 accumulates also at the phragmoplast mid zone, where it interacts with MAP65-3 at the microtubule overlap promoting timely rapid phragmoplast expansion (Herrmann et al., 2018).

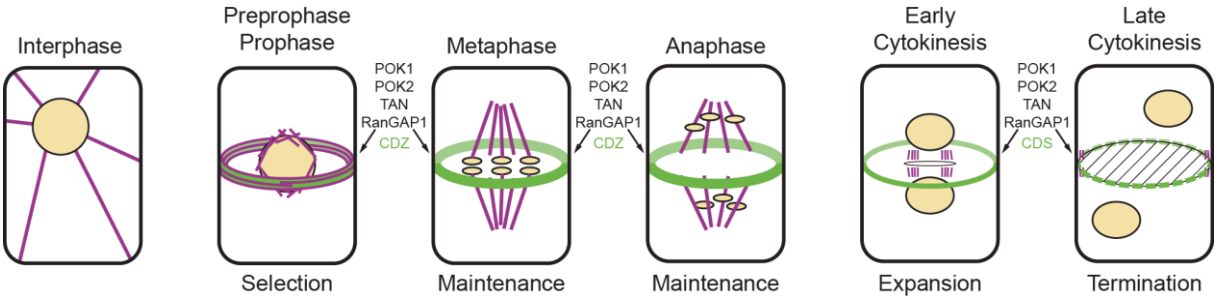

Figure 2: Plant cell division stages

Centring of the nucleus and formation of the equatorial preprophase band (PPB), a belt-like structure consisting of microtubules (magenta) and actin filaments, during preprophase/prophase. Division site resident proteins (green, PHRAGMOPLAST ORIENTING KINESIN (POK)1, POK2, TANGLED (TAN) and RanGAP1) co-localize with the PPB and establish the cortical division zone (CDZ) throughout mitosis and cytokinesis. The preprophase band is disassembled after prophase. The spindle apparatus is built during metaphase and the chromosomes are aligned. Chromosomes are separated by the spindle during anaphase. The phragmoplast is formed in early cytokinesis and expands centrifugally from the centre of the cell towards the division site. New cell plate is inserted at the site occupied by division site resident proteins (discontinuous green circle, modified from Lipka et al., 2015)

5.3 Pavement cell shape formation

Not only cell division is essential for correct formation of plant organs. Also polarized growth plays an important role in cellular morphogenesis. For instance, during monopolar growth of root hairs and pollen tubes as well as in multipolar growing leaf epidermis pavement cell differentiation. *Arabidopsis thaliana* pavement cells exhibit a characteristic puzzle shaped structure with interdigitating lobes and indentation regions. Over the years, many theories have been proposed to explain why pavement cells are formed like puzzle pieces. This particular shape might be important for the correct spacing of stomata and trichomes (Glover, 2000), to keep the leaf flat for optimal light capturing (Galletti and Ingram, 2015) or to increase leaf epidermis stability (Jacques et al., 2014; Lee et al., 2000). It might also aid to overcome

reversible deformations of the tissue (Sotiriou et al., 2018). Another plausible hypothesis is that the jigsaw puzzle form prevents pavement cells from bulging and bursting through mechanical stress that acts on the cell walls due to their turgor pressure (Sapala et al., 2018).

Although the exact cause of pavement cell puzzle shaping remains indistinct, several discoveries were made that revealed their formation process, which involves polarized growth. Pavement cell development can be separated into three stages (Figure 3A, Fu et al., 2002). In stage I at the beginning of their development, pavement cells are uniform in shape without visible curvatures (Fu et al., 2002). In stage II, lobes and indentations start to form and the cell shape changes (Fu et al., 2002). Pavement cells in stage III contain further pronounced lobe and indentation regions and moreover lobe regions often contain secondary lobes (Fu et al., 2002).

Rho of plants (ROPs) were identified as key players of polarized growth, including multipolar pavement cells. *Arabidopsis thaliana* contains 11 ROPs with various expression domains and functions. It is essential for polarized growth, that ROPs as small molecular switches cycle between an active GTP-bound state and inactive GDP-bound state (Figure 3B, Wittinghofer and Pai, 1991). In general, ROPs are regulated by three groups of proteins. ROPs are activated by guanine nucleotide exchange factors (GEFs) that catalyse the GDP to GTP exchange (Basu et al., 2008; Berken et al., 2005; Gu et al., 2006). ROP inactivation is mediated by GTPase activating proteins (GAPs) by stimulating the GTP-hydrolysis function of ROPs (Hwang et al., 2008; Klahre and Kost, 2006; Wu et al., 2000). The third group of regulators are guanine GDP dissociation inhibitors (GDIs) which are involved in GDP-ROP recycling from the plasma membrane in the cytoplasm and GDP-ROP stabilization until their reactivation (Kost, 2008).

Two ROP signalling pathways are involved in the establishment of pavement cell puzzle shape. In lobe regions, active ROP2 and the functionally redundant protein ROP4 are localized at the plasma membrane where they interact with the effector Cdc42- and Rac-interactive binding (CRIB) motif-containing protein 4 (RIC4) leading to actin filament accumulation and lobe outgrowth (Figure 3C, Fu et al., 2005; Fu et al., 2002). In indentations regions, active ROP6 interacts with another effector, RIC1 to induce microtubule bundling (Fu et al., 2005; Fu et al., 2009). RIC1 interacts with the microtubule severing protein KATANIN 1 (KTN1), that severs microtubule at their branching points resulting in microtubule reorganization into well-ordered parallel bundles (Lin et al., 2013). The bundling of microtubules in indentation regions supresses curvature outgrowth (Fu et al., 2005). ROP2-RIC4 and ROP6-RIC1 pathways act antagonistically (Fu et al., 2009). Active ROP2 sequesters RIC1 from microtubules preventing microtubule bundling in lobe regions, while overexpression of RIC1 inhibits ROP2-RIC4 interaction (Fu et al., 2009). Lobe outgrowth in one cell and growth inhibition in the indentation

region of the neighbouring cell points to a spatiotemporally regulated function of both pathways and to intercellular communication (Fu et al., 2005).

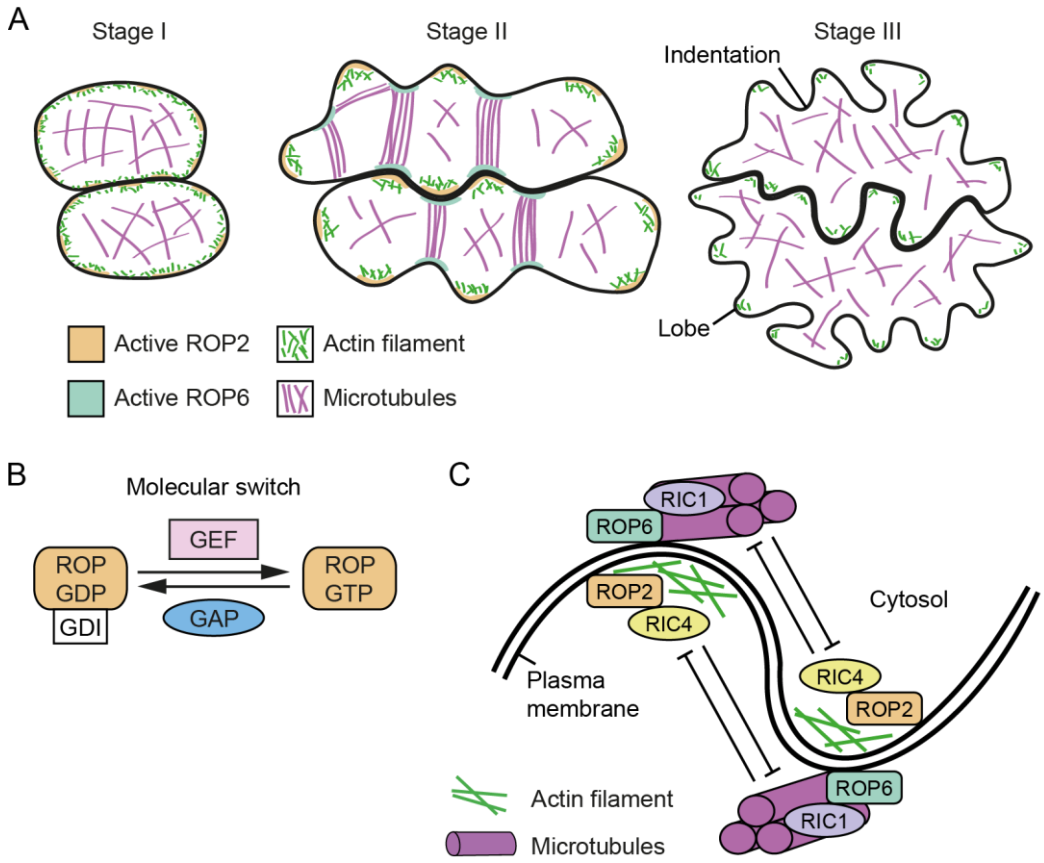

Figure 3: Model of pavement cell development and ROP regulation

(A) Pavement cell developmental stages: Cells in Stage I are uniform and start to form lobe and indentation regions in Stage II. Cell expansion and lobe formation continues in Stage III to build complex pavement cells. (B) Model of ROP activity regulation through GEF, GAP and GDI. (C) ROP2-RIC4 and ROP6-RIC1 antagonistic signalling pathways induce actin filament accumulation in lobes and microtubule bundling in indentation regions, respectively (A, Stage II). Growth promotion in lobes and growth suppression in indentations leads to the formation of pavement cells. (Modified from Craddock et al., 2012; Yalovsky et al., 2008)

It is still not fully understood how the two antagonistic pathways are activated during pavement cell shape establishment and what kind of external cues might be involved in the initiation of the differentiation process. Two hypotheses have been proposed. The plant hormone auxin is thought to be the first candidate that activates the antagonistic ROP2 and ROP6 pathways in an AUXIN-BINDING PROTEIN 1 (ABP1) dependent manner (Xu et al., 2010). Also, ROP2 was identified as critical factor for PIN1 targeting to the plasma membrane in lobe regions where PIN1 functions in auxin export (Xu et al., 2010). Furthermore, FYPP1, a phytochrome-associated serine/threonine protein phosphatase 2A (PP2A), and Ser/Thr protein kinase PINOID (PID) have been shown to regulate the phosphorylation status of PIN1 in pavement cells. Depending on the phosphorylation status, PIN1 is localized to the lobe (hypo-

phosphorylated) or indentation (hyper-phosphorylated) region functioning as a polarity switch between lobes and indentations (Li et al., 2011). It has been also shown that auxin induces the interaction of the plasma membrane localized transmembrane receptor-like kinase 1 (TMK1) with ABP1 leading to activation of ROP signalling (Xu et al., 2014). Further analysis of TMK1 and ROP6 lead to the following model: Auxin signalling induce lipid nanodomains and TMK1 clustering which in turn promotes the stabilization of larger ordered lipid nanodomains (Pan et al., 2020). ROP6 is then recruited to this large lipid nanodomains and its activation induce microtubule reorganization, that restricts the diffusion of TMK1 ordered lipid nanodomains in a positive feedback loop (Pan et al., 2020). It was proposed that the accumulation of active ROP6 in nanodomains eventually leads to the formation of polarized ROP6 domains that initiate indentation formation (Pan et al., 2020). ABP1 was proposed to be a key component in auxin signalling and essential for plant development (Xu et al., 2014; Xu et al., 2010), but analysis of *abp1* knockout mutants revealed that ABP1 does not play a major role in this process (Gao et al., 2015). Furthermore, a detailed analysis revealed that *pin1-1* exhibit no pavement cell phenotype and PIN1 was expressed in the leaf margins, but not in developing pavement cells (Belteton et al., 2018). Therefore, it remains questionable whether ROP2 and ROP6 pathways are activated via PIN1 and ABP1-dependent auxin signalling.

The second theory proposes that there are no molecular external signals involved and biophysical cues such as mechanical stress, cell geometry and cell wall reinforcement are sufficient for jigsaw puzzle shaping. Computational modelling predicted that curvature formation is induced by turgor pressure that generates compressive stress on the pavement cell wall, resulting in mechanical cell wall buckling (Bidhendi et al., 2019). Furthermore, demethylated pectin was identified to increase wall stiffness on a future indentation side, leading to growth suppression on the indentation side without affecting growth on lobe side (Altartouri et al., 2019). This differential expansion on lobe and indentation sides and the resulting cell wall buckling generate local stress hotspots in the cell wall (Altartouri et al., 2019; Bidhendi et al., 2019). Cells respond to localized stress by aligning microtubules along the maximal tensile stress direction (Hamant et al., 2008). Therefore, parallel microtubule bundles are recruited to cell wall stress hotspots which later evolve into pronounced indentation regions (Bidhendi et al., 2019). This notion is supported by another computational model showing that in stage II pavement cells, indentation regions with parallel aligned microtubules, experience the highest mechanical stress (Fu et al., 2005; Sampathkumar et al., 2014). Microtubule bundling in indentation regions facilitate local cell wall reinforcement by cellulose deposition resulting in further cell wall stiffening, which in turn is necessary for proper lobe formation (Altartouri et al., 2019; Bidhendi et al., 2019; Paredez et al., 2006).

However, not only initiation of ROP2-RIC4 and ROP6-RIC1 pathways, but also regulation and restriction of ROP activity to their assigned regions is important for proper pavement cell shape

establishment, since constitutive expression or overexpression of ROP2 and ROP6 led to a loss of the complex jigsaw puzzle shape (Fu et al., 2002; Fu et al., 2009). So far, only two regulators have been identified in pavement cell development the GEF SPIKE1 (SPK1) and the guanine GDP dissociation inhibitor GDI1. *spk1* mutants displayed a severe loss of pavement cell shape complexity and interaction analysis in petals revealed that SPK1 interacts with ROP2, ROP4 and ROP6 (Basu et al., 2008; Liang et al., 2019; Ren et al., 2016). GDI1 also interacted with ROP2 and ROP6 and the reduction in pavement cell shape complexity after GDI1 overexpression indicate a role of GDI1 in ROP2 and ROP6 regulation (Wu et al., 2013). However, the exact function of SPK1 and GDI1 in ROP2 and ROP6 regulation during pavement cell development still needs to be determined. Besides, which GAPs are involved in the inactivation of ROP2 and ROP6 is still unknown.

5.4 *Arabidopsis* GTPase activating proteins

Arabidopsis thaliana contains two groups of GAPs, ROPGAPs with six members and ROP1 Enhancer (REN)GAPs with three members, both sharing a central GAP-domain that is necessary for ROP inactivation (Figure 4A, Eklund et al., 2010; Hwang et al., 2008; Wu et al., 2000). Additionally, ROPGAPs possess at the amino (N)-terminus a CRIB domain, which was shown to enhance ROP-ROPGAP binding and to mediate subcellular localization (Figure 4B, (Klahre and Kost, 2006; Schaefer et al., 2011; Wu et al., 2000). RENGAPs, also called PHGAPs, lack the N-terminal CRIB-domain and instead contain a pleckstrin homology (PH)-domain proposed to facilitate phosphoinositide binding (Hwang et al., 2008; Kulich et al., 2020; Lemmon, 2008). Furthermore, at their carboxy (C)-termini PHGAPs and ROPGAP4 exhibit a number of predicted coiled coil domains, which are thought to be critical for protein-protein interactions and in case of REN1 for vesicle association (Hwang et al., 2008).

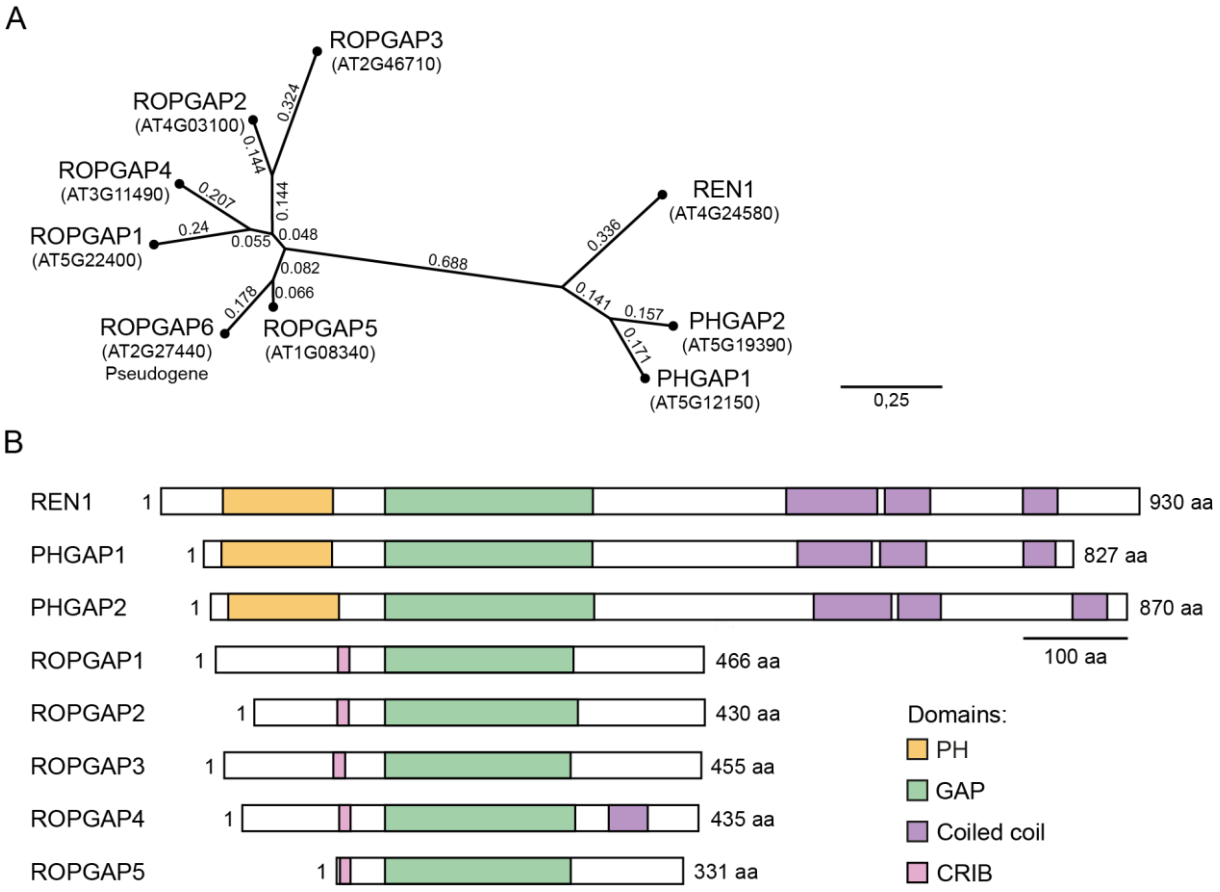

Figure 4: Phylogenetic tree and protein domain architecture of ROPGAPs and PHGAPs

(A) Unrooted tree depicting phylogenetic relationships between ROPGAPs and PHGAPs. The tree was constructed with CLC Main Workbench 8.0 using the coding DNA sequence (CDS) and neighbour joining method. (B) Protein domain organization of PHGAPs and ROPGAPs. They display an N-terminal pleckstrin homology (PH) or Cdc42- and Rac-interactive binding (CRIB) domain, the central GTPase activating (GAP) domain and at the C-terminus a number of coiled coil domains. ROPGAP6 is annotated as a pseudogene, thus is not depicted. Protein domain predictions were extracted from UniProt (https://www.uniprot.org/) and using Paircoil2 (http://cb.csail.mit.edu/cb/paircoil2/paircoil2-like.html).

ROPGAP1 was characterized as regulator of pollen tube tip growth, restricting ROP1 activity on the tip (Fu et al., 2001; Hwang et al., 2010). ROP1 is a key component of polarized pollen tube growth in *Arabidopsis thaliana*, *Nicotiana benthamiana* and *Pisum sativum* (Kost et al., 1999; Li et al., 1999; Lin and Yang, 1997). Active ROP1 is localized at the pollen tube tip, where it interacts with RIC3 and RIC4 (Gu et al., 2005). ROP1-RIC4 interaction leads to actin filament assembly, which promotes exocytic vesicle accumulation but inhibits exocytosis (Gu et al., 2005; Lee et al., 2008). ROP1-RIC3 interaction increases Ca^{2+} levels, resulting in actin filament disassembly and consequently allowing fusion of exocytic vesicles (Gu et al., 2005; Lee et al., 2008). Besides, *Arabidopsis thaliana* ROPGAP2 dimerizes via its GAP domain and forms a 2:2 complex with ROPs (Schaefer et al., 2011). ROPGAP2 showed no tissue specific expression pattern, but had the highest binding affinity to ROP1, ROP7 and ROP9 (Schaefer et al., 2011). However, whether ROPGAP2 functions in the inactivation of those ROPs during

pollen tube tip growth (ROP1), in stomatal opening or during late stage of xylem differentiation (ROP7) or throughout embryo development and lateral root formation (ROP9) has to be clarified (Brembu et al., 2005; Li et al., 1999; Nibau et al., 2013; Wang et al., 2017). ROPGAP3 is also expressed in pollen tubes, but its implication in pollen tube growth has not been further analysed (Hwang et al., 2010). ROPGAP4 negatively regulates the activation of ROP2 under O_2 deprivation (Baxter-Burrell et al., 2002). Furthermore, ROPGAP1 and ROPGAP4 seem to function in responses to pathogens, since *ropgap1* and *ropgap4* showed enhanced susceptibility to *Erysiphe cruciferarum* a virulent powdery mildew fungus (Huesmann et al., 2011). In addition, ROPGAP3 and ROPGAP4 have redundant functions in the inactivation of ROP11 during secondary cell wall formation in xylem cells (Nagashima et al., 2018; Oda and Fukuda, 2012). Not only ROPGAP3 and ROPGAP4, but also ROPGAP5 is upregulated during xylem differentiation, however its exact function has not been characterized in detail (Oda and Fukuda, 2012; Ohashi-Ito et al., 2010). ROPGAP6 has been annotated as a pseudogene and has probably no biological relevance (Tair database entry, https://www.arabidopsis.org/servlets/TairObject?id=31244&type=locus).

Apart from ROPGAP1, the PHGAP REN1 plays a major role in the regulation of ROP1 activity during pollen tube growth (Hwang et al., 2008; Hwang et al., 2010). Based on their findings, Hwang et al. suggested that REN1 is associated with exocytic vesicles via its C-terminal domain and is transported to the pollen tube tip after ROP1-RIC4 induced actin filament accumulation (Gu et al., 2005; Hwang et al., 2008; Lee et al., 2008). After ROP1-RIC3 induced increase in cytosolic Ca^{2+} levels and actin filament disassembly, REN1 reaches the plasma membrane after exocytic vesicle fusion where it inactivates the active ROP1 (Gu et al., 2005; Hwang et al., 2008; Lee et al., 2008). Following ROP1 inactivation, REN1 cycles back to the cytosol allowing reactivation of ROP1 at the tip (Hwang et al., 2008). Regulation of ROP1 activity is essential for proper pollen tube tip growth (Gu et al., 2005; Hwang et al., 2008; Lee et al., 2008).

In contrast, the REN1 relatives, PHGAP1 and PHGAP2 that are closely related, showed an overlapping expression in leaf primordia, young leaves and mature stomata (Lauster, 2013; Stöckle, 2015). Furthermore, PHGAP1 is expressed in the root epidermis and cortex, as well as in the sporophytic tissue adjacent to the micropylar pole in ovules (Stöckle, 2015). In addition, PHGAP2 is expressed in the root vasculature and the entire ovule (Stöckle, 2015). PHGAPs were initially identified in a yeast-two-hybrid (Y2H) screen as interaction partners of POK1 (Stöckle et al., 2016). PHGAP1 was shown to co-localize with POK1 at the cortical division site during cytokinesis, suggesting a role for PHGAP1 during cell division (Stöckle, 2015). Overlapping expression patterns of PHGAP1 and PHGAP2 and the lack of single mutant phenotypes pointed to redundant functions (Stöckle, 2015). *phgap1-1 phgap2-1* double mutants displayed cell division phenotypes during embryo development, suggesting that

PHGAP2 is also participating in cell division (Stöckle, 2015). Furthermore, *phgap1-1 phgap2-1* double mutants exhibited a reduced number of fertilized ovules and displayed a male gametophyte dependent transmission defect (Stöckle, 2015). Although pollen tube growth was not affected in *phgap1-1 phgap2-1*, the large number of non-germinated pollen grains observed in double mutants could be the cause of the male gametophytic defect (Stöckle, 2015). PHGAP2 was not able to complement *ren1-4* pollen tube elongation defects, indicating that PHGAP2 has probably no function during pollen tube tip growth and cannot substitute REN1 function (Stöckle, 2015). PHGAP1 and PHGAP2 showed not only functions related to cell division. In particular, the generation of more lancet-shaped leaves and the lack of pavement cell shape complexity in *phgap1-1 phgap2-1* pointed to an additional function during leaf morphogenesis and development of leaf epidermal pavement cells (Stöckle, 2015). Furthermore, it was shown that PHGAP2 interacts with ROP2, ROP4 and ROP6 that are involved in pavement cell development (Stöckle, 2015). In addition, substitution of a conserved arginine to leucine in the GAP domain (PHGAP1^{R203L} and PHGAP2^{R198L}), that abolished PHGAP function, prevented *phgap1-1 phgap2-1* pavement cell phenotype restoration, implicating the requirement of a functional PHGAP for cell shape establishment (Stöckle, 2015). Moreover, water loss and water uptake experiments indicated that PHGAP1 and PHGAP2 seem to be important for water homeostasis, but not required for water transport (Stöckle, 2015).

6. Objectives

ROPs are small molecular switches that play major roles in several developmental processes. However, their function has to be spatiotemporally controlled, as defective regulation results in severe phenotypical abnormalities.

Recently, two ROP inactivators, PHGAP1 and PHGAP2, were identified in a yeast-two-hybrid screen as interaction partners of POK1. PHGAP1 and POK1 co-localized at the division site during cytokinesis and the *phgap1-1 phgap2-1* double mutant exhibits cell division defects in embryo development pointing towards a functional implication of PHGAPs in cell division. The first goal of this thesis was to further functionally characterize PHGAPs and to get an insight into their implication throughout cell division. Our approaches included the investigation of the functional requirement of different PHGAP domains, potential phosphor-regulation of PHGAPs activity and the localization patterns of these deletion and phospho-mutants.

Interestingly, in addition to cell division defects, *phgap1-1 phgap2-1* displays also a loss of pavement cell shape complexity that could not be restored when the GAP function was compromised by amino acid substitution (PHGAP1^{R203L} and PHGAP2^{R198L}). This result underlines the necessity of PHGAP activity throughout the development of *Arabidopsis* leaf epidermal cells. The latter process relies on the function of the two antagonistic ROP-mediated signalling pathways involving ROP2/4 and ROP6, whereas PHGAP2 was shown to interact with all ROPs involved. Therefore, the second aim of this thesis was to investigate the role of PHGAPs in regulation of ROP activity. Considering that PHGAP2 was able to interact with those ROPs in general, the question arises whether PHGAPs act also as ROP inactivators in both pathways during pavement cell development. Furthermore, specific aspects of PHGAP participation in differentiation of *Arabidopsis* leaf epidermis cells remain unclear. To answer these questions, we employed detailed phenotypic *phgap* mutant and PHGAP localization pattern analysis, investigated the cytoskeletal organization in *phgap1-1 phgap2-1* and performed further interaction assays with potential ROP candidates. In summary, the present thesis aimed at unravelling the role of PHGAPs in morphogenetic mechanisms in plants.

7. Results and Discussion

7.1 Functional characterization of PHGAP1 and PHGAP2 in cell division

PHGAP1 and PHGAP2 function in a POK-dependent manner in cell division plane selection

Cell division is a fundamental process for proper plant development. Therefore, it is critical that cell division is correctly conducted. Loss of two kinesin-12 class motor proteins, POK1 and POK2, resulted in phragmoplast guidance defects, mispositioning of the cell plate and consequently formation of misshaped cells and organs (Lipka et al., 2014). POK1 is essential for the establishment of the CDZ/CPFS and the maintenance of other CDZ markers like TAN and RanGAP1 (Lipka et al., 2014; Walker et al., 2007; Xu et al., 2008). In the research article entitled 'Putative RopGAPs impact division plane selection and interact with kinesin-12 POK1' we identified the first GTPase activating proteins, namely PHGAP1 and PHGAP2, to be involved in cell division (Stöckle et al., 2016). As noted above, PHGAP1 and PHGAP2 were initially found as interaction partners of POK1 in a Y2H screen (Stöckle et al., 2016). In this article we confirmed the interaction of PHGAPs with truncated POK1 C-terminal fragments ($POK1^{1213\text{-}2066}$ and $POK1^{1683\text{-}2066}$) performing a mating-based split-ubiquitin interaction assay and ratiometric bimolecular fluorescent complementation (rBiFC) experiments (Grefen et al., 2009).

POK1 starts to accumulate at the CDZ during prophase and remains there until the end of cytokinesis (Lipka et al., 2014). To analyse the localization pattern of PHGAPs during cell division, we expressed the cDNA constructs *pUBN:GFP-PHGAP1* and *pUBN:GFP-PHGAP2* as well as the full genomic construct *pPHGAP2:GFP-PHGAP2* in wild type *Arabidopsis* plants. In interphase, GFP-PHGAP1 and GFP-PHGAP2 were localized in the cytoplasm and at the plasma membrane. Analysis of the distribution of PHGAPs in different cell division stages revealed, that unlike POK1, PHGAP1 and PHGAP2 started to accumulate at the division site during meta-/anaphase forming a ring-like structure and remained there throughout cytokinesis. Co-expression studies of YFP-POK1 and RFP-PHGAP1 confirmed co-localization of YFP-POK1 rings and RFP-PHGAP1 rings. Next, to examine whether PHGAP localization at the division site is POK-dependent, we expressed PHGAPs in the *pok1-1 pok2-3* double mutant background. Although, PHGAP1 and PHGAP2 displayed still cytoplasmic and plasma membrane localization, they did not accumulate at the CDZ/CPFS in the absence of POK1. These results indicate that POK function is required for PHGAP recruitment to the division site.

To characterize the role of PHGAPs during cell division, we analysed *phgap1-1 phgap2-1* double mutants, since the single mutants showed no obvious phenotype. The *Arabidopsis* root meristem is highly organized, displaying well-ordered cell wall patterns. Knockdown of *PHGAPs* in *phgap1-1 phgap2-1* resulted in moderate reduction of root growth and modest cell

wall positioning defects compared to the wild type. However, *phgap1-1 phgap2-1* cell division defects were not as severe as in *pok1-1 pok2-3* double mutants and a *pok1-1 pok2-3 phagp1-1 phgap2-1* quadruple mutant showed no obviously enhanced phenotype compared to *pok1-1 pok2-3*. Further, cell division defects were also observed in early embryo development of *phgap1-1 phgap2-1*. Taken together these results suggest redundant functions of PHGAP1 and PHGAP2 in cell division plane positioning in the root meristem and in early embryo development.

Afterwards, we determined the importance of PHGAPs during cell division by investigating the organization of mitotic structures in *phgap1-1 phgap2-1*. We observed misaligned preprophase bands in addition to misaligned phragmoplasts in *phgap1-1 phgap2-1*, albeit PHGAPs are not accumulated at the CDZ during prophase. Analysis of POK1 localization in *phgap1-1 phgap2-1* revealed co-alignment of POK1 signal with the mispositioned PPBs, indicating that POK1 is still recruited to the division site predicted by the PPB. Further analysis of the deviation angle, using POK1 as division site marker, confirmed the positioning defects of PPBs and phragmoplasts in *phgap1-1 phgap2-1*. This division site defects in *phgap1-1 phgap2-1* could be rescued by the expression of *pPHGAP2:GFP-PHGAP2*, suggesting that PHGAPs function in division plane selection and correct PPB placement.

Furthermore, we investigated whether PHGAP localization depends on GAP function. Therefore, we mutated the conserved catalytic arginine in the GAP domain generating *pUBN:GFP-PHGAP1*^{R203L} and *pUBN:GFP-PHGAP2*^{R198L} and we expressed the constructs in the *phgap1-1 phgap2-1* background. Inhibition of GAP function had no effect on the timely localization of PHGAPs at the CDZ/CPFS during cell division. However, the root growth, cell wall positioning and misaligned PPB/phragmoplast defects in *phgap1-1 phgap2-1* could not be rescued without a functional GAP domain, underlying the importance of the latter domain for PHGAP activity.

Our results allowed us to conclude that PHGAPs participate in preprophase band positioning acting upstream of POK1, however they still require POK function for their accumulation at the CDZ/CPFS during meta-/anaphase. Our finding that two GTPase activating proteins functioning in division plane selection, revealed the first hint towards potential ROP activity in cytoskeletal reorganization at the division site during cell division.

PHGAP C-terminal domain is essential for division site and plasma membrane localization

PHGAP1 and PHGAP2 contain three different domains, the N-terminal PH domain, the central GAP domain and predicted coiled coil domains at the C-terminus. As mentioned early, mutating the catalytic arginine in the GAP domain abolished PHGAP function, but not localization during cell division (Stöckle et al., 2016). Since, the closest homolog of PHGAP1 and PHGAP2, REN1, was neither able to localize to the pollen tube apex nor could the pollen tube phenotype of *ren1-1* be restored when the coiled coil domain containing C-terminal part was absent, we tried to gain more insights into the importance of the PHGAP1 and PHGAP2 C-terminus for division site localization during cell division (Hwang et al., 2008). Thus, we generated different deletion mutants and I examined their spatiotemporal localization pattern (Figure 5A). To identify the different cell division stages, *pUBN:GFP-PHGAP1*$^{1-459}$, *pPHGAP2:GFP-PHGAP2*$^{1-764}$ and *pPHGAP2:GFP-PHGAP2*$^{1-566}$ were co-expressed with the microtubule reporter *pUBN:RFP-MBD* or alternatively the plasma membrane was stained with the fluorescent dye FM4-64 (Figure 5B, D and F). To analyse in more detail plasma membrane localization of the truncated protein, we generated plot profiles across the plasma membrane (Figure 5C, E and G). Deletion of the complete C-terminus of PHGAP1 and PHGAP2 (PHGAP1$^{1-459}$ and PHGAP2$^{1-566}$) resulted in a complete loss of division site and plasma membrane localization (Figure 5B, C, F, G and H). Interestingly, when only the last predicted coiled coil domain was deleted from PHGAP2 (PHGAP2$^{1-764}$) the protein was still able to localize to the plasma membrane, but the accumulation at the cortical division site was severely affected (Figure 5D, E and H). Further investigation of the root meristem organization revealed, that GFP-PHGAP2$^{1-764}$, like the full length GFP-PHGAP2, was able to restore the oblique cell wall phenotype in *phgap1-1 phgap2-1*, although it did not accumulate at the division site (Figure 5I). In contrast, GFP-PHGAP2$^{1-566}$ still displayed oblique cell walls in the root meristem and was not able to restore *phgap1-1 phgap2-1* (Figure 5I). These results indicate, that the coiled coil domain-containing C-terminal part of PHGAP1 and PHGAP2 is essential for accumulation at the division site and plasma membrane localization.

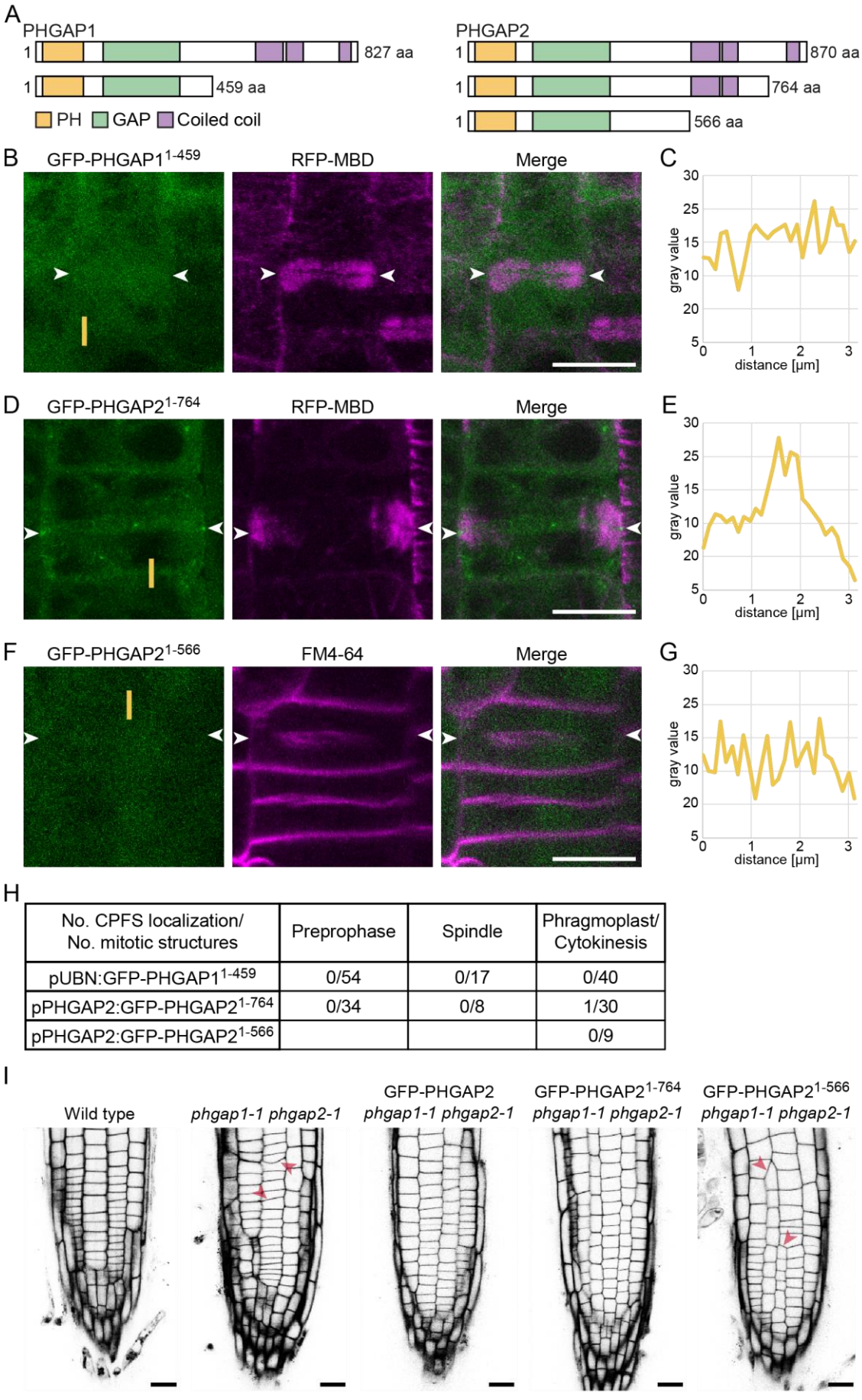

H

No. CPFS localization/ No. mitotic structures	Preprophase	Spindle	Phragmoplast/ Cytokinesis
pUBN:GFP-PHGAP1 1-459	0/54	0/17	0/40
pPHGAP2:GFP-PHGAP2 1-764	0/34	0/8	1/30
pPHGAP2:GFP-PHGAP2 1-566			0/9

Figure 5: PHGAP C-terminal domain is essential for division site localization

(A) Protein domain architecture of PHGAP1 and PHGAP2 illustrating the N-terminal pleckstrin homology (PH)-domain, the central conserved GTPase activating protein (GAP) domain and coiled coil domains at the C-terminus (predicted by UniProt, https://www.uniprot.org/ and Paircoil2, http://paircoil2.csail.mit.edu). C-terminal deletion mutants are shown. (B, D and F) Z-Projections of cytokinetic cells of double mutant root meristems expressing (B) *pUBN:GFP-PHGAP1*$^{1-459}$ (*phgap1-1/*+ *phgap2-1/*+ segregating background), (D) *pPHGAP2:GFP-PHGAP2*$^{1-764}$ (*phgap1-1/*+ *phgap2-1/*+ segregating background) or (F) *pPHGAP2:GFP-PHGAP2*$^{1-566}$ (*phgap1-1 phgap2-1*) seven days after sowing (DAS). The microtubule reporter (B and D) *pUBN:RFP-MBD* or the membrane dye (F) FM4-64 were used to distinguish between different cell division stages. Arrow heads mark the position of the cell plate fusion site (CPFS), where accumulation of PHGAP signal is expected. Note that only GFP-PHGAP2$^{1-764}$ (D) is faintly accumulated at the division site. Scale bars 10 µm. (C, E and G) Plot profiles displaying the GFP-PHGAP signal intensity (gray value) along the yellow line shown in B, D and F, respectively. Note the peak in (E) GFP-PHGAP2$^{1-764}$ indicating plasma membrane localization and its absence in (C) GFP-PHGAP1$^{1-459}$ and (G) GFP-PHGAP2$^{1-566}$. (H) Table summarizing the number (no.) of observed CPFS localizations/mitotic structure of GFP-PHGAP1$^{1-459}$ (17 seedlings from four experiments), GFP-PHGAP2$^{1-764}$ (6 seedlings from one experiment) and GFP-PHGAP2$^{1-566}$ (2 seedlings from one experiment) in different cell division stages. (I) Representative single plane images of the root meristem cell wall pattern of seedlings stained with propidium iodide (10 mg/ml) seven DAS. Depicted are wild type, *phgap1-1 phgap2-1* and *pPHGAP2:GFP-PHGAP2*, *pPHGAP2:GFP -PHGAP2*$^{1-764}$ and *pPHGAP2:GFP -PHGAP2*$^{1-566}$ expressed in *phgap1-1 phgap2-1* double mutants. Arrows (red) point to oblique cell walls. Scale bars 20 µm.

PHGAP1 and PHGAP2 form homo- and heterodimers

Previously, ROPGAP2 was shown to dimerize via its GAP domain and to form a 2:2 complex with ROPs (Schaefer et al., 2011). To investigate, whether PHGAP1 and PHGAP2 form homo- or heterodimers, we performed a mating-based split-ubiquitin experiment using full length PHGAP1 and PHGAP2 and different deletion mutants (Figure 6A-B). Both PHGAPs were able to interact with themselves or the other PHGAP despite the absence of N-terminal or C-terminal domains (Figure 6A, C-D). A lack of PHGAP2 C-terminal predicted coiled coil domains (PHGAP2$^{1-764}$ and PHGAP2$^{1-566}$) resulted in enhanced interaction with full length PHGAPs. These data indicate that PHGAPs are able to form homo- and heterodimers, probably in a similar way as ROPGAP2 via their central GAP domain, since the absence of the N- or C-terminus had no effect on interaction.

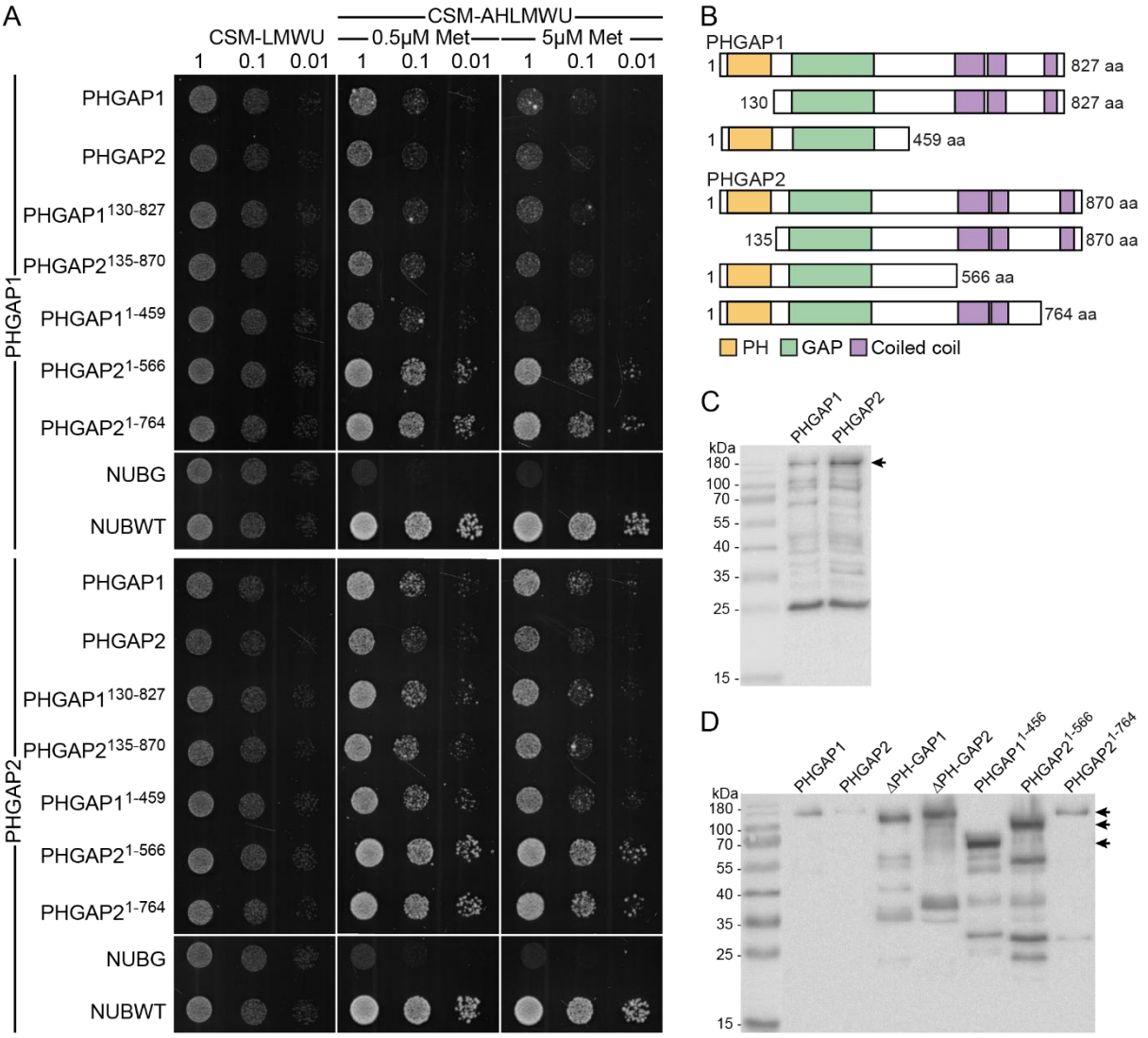

Figure 6: PHGAP1 and PHGAP2 form homo- and heterodimers

(A) Yeast mating-based split-ubiquitin system (SUS) assays were performed using PHGAP1 and PHGAP2 as baits (-Cub fusion) and PHGAP1, PHGAP2, PHGAP1$^{130-827}$, PHGAP2$^{135-870}$, PHGAP1$^{1-456}$, PHGAP2$^{1-566}$ and PHGAP2$^{1-764}$ as preys (NubG- fusion). Yeast diploids of bait plus prey or bait plus controls (NUBG, negative control and NUBWT, positive control) were spotted onto CSM-Leu-, Met-, Trp- , Ura- (CSM-LMWU) medium to confirm mating and on CSM-Ade-, His-, Leu-, Met-, Trp-, Ura- (AHLMWU) with 0.5 µM or 5 µM methionine to test for interaction. Colonies correspond to culture concentration 1, 0.1 and 0.001 at OD_{600} from left to right. Control plates and interaction plates were scanned after 24 h and 48 h, respectively. (B) Protein domain architecture of full length PHGAP1 and PHGAP2 and the deletion mutations used in (A). (C and D) Western blots showing the expression of the baits (C) PHGAP1 (152 kDa) and PHGAP2 (157 kDa) (arrow) and the preys (D) PHGAP1 (100 kDa), PHGAP2 (105 kDa), ΔPH-GAP1 (86 kDa), ΔPH-GAP2 (90 kDa), PHGAP1$^{1-456}$ (59 kDa), PHGAP2$^{1-566}$ (70 kDa) and PHGAP2$^{1-764}$ (93 kDa) (arrows, upper bands) used in (A). Shown are the data from one of two replicates of the assay with similar results (second assay, Haller, 2019).

Phospho-regulation affects the timely localization of PHGAPs at the cortical division site

Phosphorylation as posttranslational modification is regulating the activity of proteins (reviewed in Hodges et al., 2013). PHGAP1 and PHGAP2 contain several predicted phosphorylation sites (Figure 7A, PhosPhAt 4.0, phosphat.uni-hohenheim.de/phosphat.html). To investigate, whether PHGAPs are phospho-regulated, the serine at amino acid position 447 of PHGAP2 was mutated to glutamic acid generating a phospho-mimic mutant and to alanine creating a phospho-deficient mutant. Both mutants, GFP-PHGAP2^{S447E} and GFP-PHGAP2^{S447A}, were co-expressed with the microtubule reporter RFP-MBD under the control of the ubiquitin promoter in the *phgap1-1/+ phgap2-1/+* double mutant background. The microtubule reporter was used to distinguish between different cell division stages and GFP-PHGAP2^{S447E}/GFP-PHGAP2^{S447A} division site accumulation was analysed throughout mitosis and cytokinesis. The phospho-mimic version GFP-PHGAP2 ^{S447E} displayed a localization pattern comparable to wild type PHGAP2, started accumulating at the division site during metaphase (Figure 7B (left panels) and 7C, Stöckle et al., 2016). However, missing phosphorylation at amino acid position 447, led to an earlier arrival of GFP-PHGAP2^{S447A} at the cortical division site, showing already co-localization with the preprophase band during preprophase/prophase (Figure 7B (right panels) and 7C). These results suggest that the phosphorylation status of PHGAP2 might be related to the timely localization of PHGAP2 at the division site during cell division.

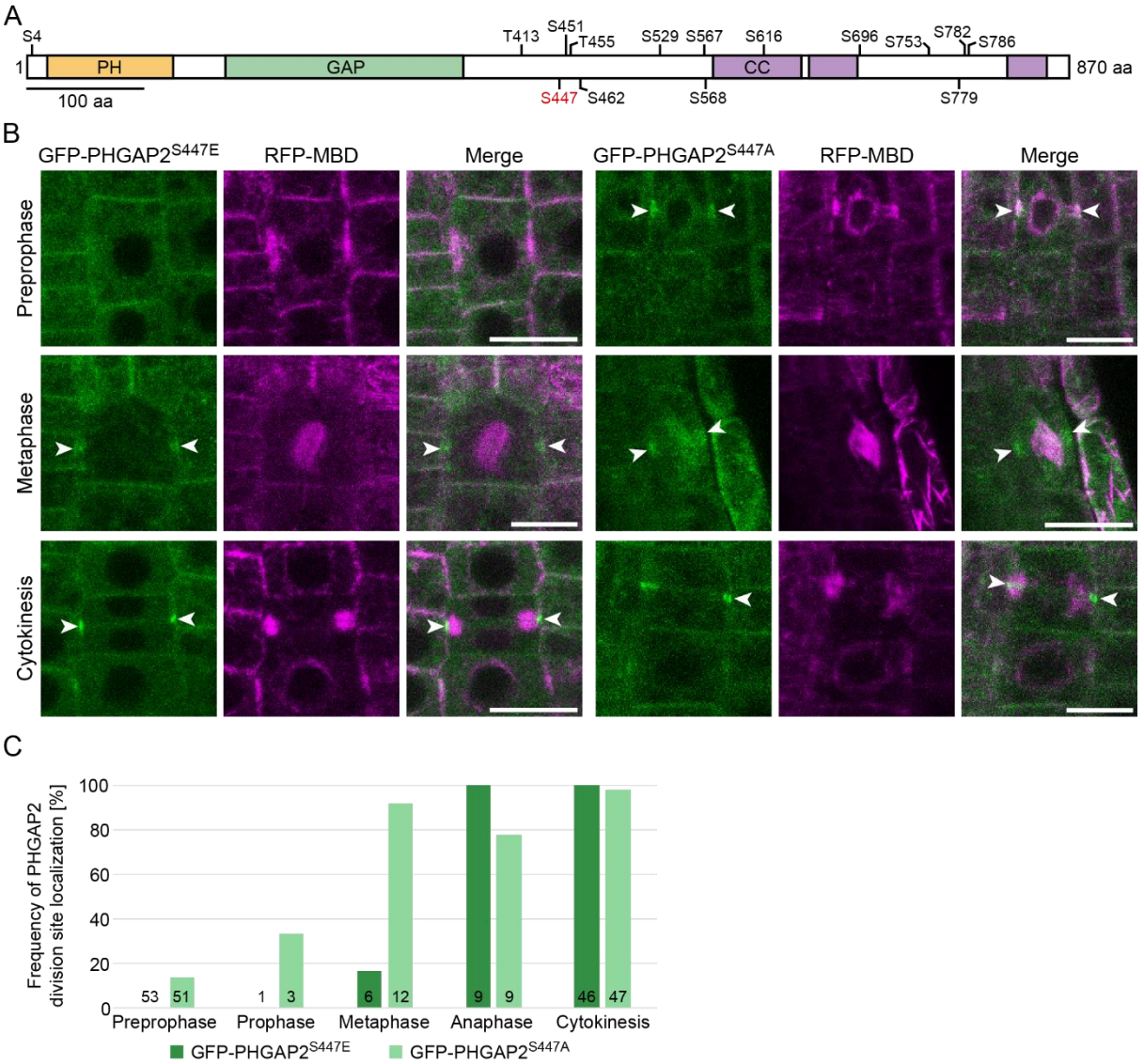

Figure 7: Phospho-deficiency of S447 affects the timely accumulation of PHGAP2 at the cortical division site

(A) Protein domain architecture of PHGAP2 with N-terminal pleckstrin homology (PH) domain, central GAP domain and C-terminal coiled coil (CC) domains. Position of the different phosphorylation sites are marked and the mutated position is highlighted (red, PhosPhAt 4.0, phosphat.uni-hohenheim.de/phosphat.html). (B) Z-Projection of *phgap1-1/+ phgap2-1/+* root cells in different cell division stages expressing *pUBN:GFP-PHGAP2*^{S447E} (phosphor-mimic) and *pUBN:GFP-PHGAP2*^{S447A} (phospho-deficient) seven days after sowing (DAS), respectively. The microtubule reporter *pUBN:RFP-MBD* was co-expressed to identify cell division stages. Arrow heads mark PHGAP2 localization at the cortical division site. Scale bars 10 µm. (C) Bar plot representing the frequency of PHGAP2 accumulation at the cortical division site in different cell division stages. The total number of cells analysed per cell cycle stage is indicated within the bars (13-16 seedlings from two to three experiments).

Considering the potential importance of PHGAPs phosphorylation status, the question arises: which proteins are involved in the phospho-regulation of PHGAPs during cell division? Possible candidates for phospho-regulation are components of the TTP-complex required for preprophase band formation (Azimzadeh et al., 2008; Schaefer et al., 2017; Spinner et al.,

2013; Torres-Ruiz and Jürgens, 1994; Traas et al., 1995). These are TONNEAU1 (TON1), the TON1 recruiting motif (TRM) proteins and the protein phosphatase 2A (PP2A) heterotrimeric holoenzyme with FASS as a regulatory subunit (Camilleri et al., 2002; Kirik et al., 2012; Spinner et al., 2013; Torres-Ruiz and Jürgens, 1994; Traas et al., 1995). A previous study of the *trm6 trm7 trm8* (*trm678*) triple mutant revealed, apart from the lack of PPB formation, also a delayed recruitment of POK1 to the division site (Schaefer et al., 2017). To assess, whether PHGAP2 localization at the division site is also delayed in *trm678*, *pPHGAP2:GFP-PHGAP2* was expressed in *trm678* or *phgap1-1 phgap2-1* mutants followed by immune-detection of GFP and microtubules and analysis of the localization pattern. GFP-PHGAP2 expressed in the *phgap1-1 phgap2-1* double mutant background functioned as control and exhibited, as expected, accumulation of GFP-PHGAP2 at the division site during metaphase and cytokinesis (Figure 8A (left panels) and 8B). However, recruitment of GFP-PHGAP2 to the division site was delayed in *trm678*, suggesting a role of the TTP complex in PHGAP2 regulation (Figure 8A (right panels) and 8B).

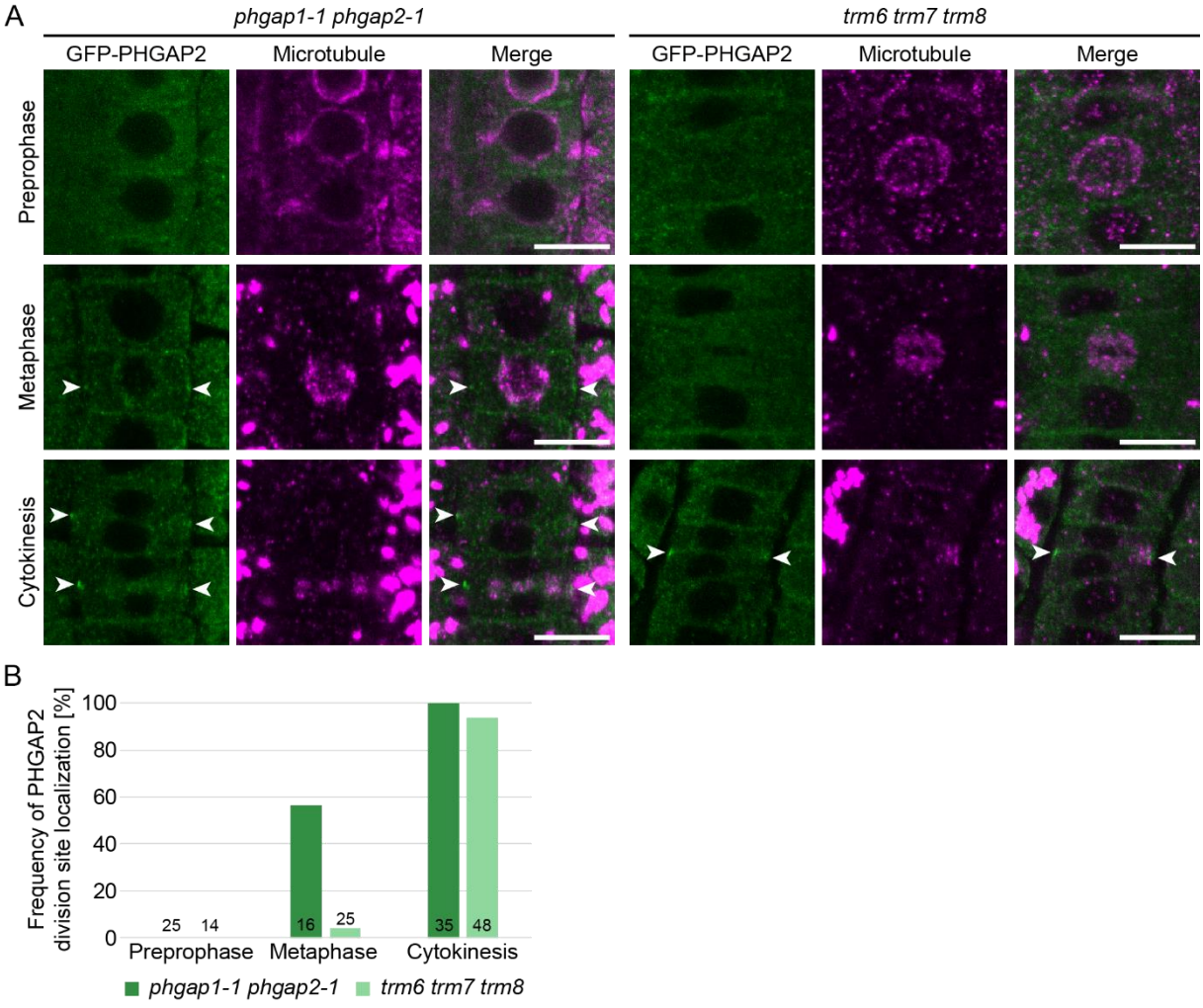

Figure 8: PHGAP2 accumulation at the cortical division site is delayed in *trm6 trm7 trm8* triple mutants

(A) Z-Projections of *phgap1-1 phgap2-1* and *trm6 trm7 trm8* root meristem cells in different cell division stages expressing *pPHGAP2:GFP-PHGAP2* six days after sowing (DAS). Arrow heads mark PHGAP2 accumulation at the cortical division site. Immuno-detection was used to visualize PHGAP2 (green, anti-GFP, anti-rabbit Alex488) and microtubules (magenta, anti-tubulin, anti-rat Cy3). Scale bars 10 µm. (B) Bar plot comparing the frequency of GFP-PHGAP2 division site localization in dividing cells in *phgap1-1 phgap2-1* (9 seedlings) and *trm6 trm7 trm8* (17 seedlings). Numbers indicate the total number of cells analysed per cell cycle stage of one experiment.

A part of the TTP-complex, the scaffolding subunit PP2AA3 was tested as interaction partner of PHGAP1 and PHGAP2. We performed a mating based split-ubiquitin assay using PHGAP1 and PHGAP2 as 'baits' and PP2AA3 as 'prey'. PP2AA3 was found to interact strongly with PHGAP1 as well as PHGAP2, implicating a role for PP2AA3 in PHGAP dephosphorylation (Figure 9A-B).

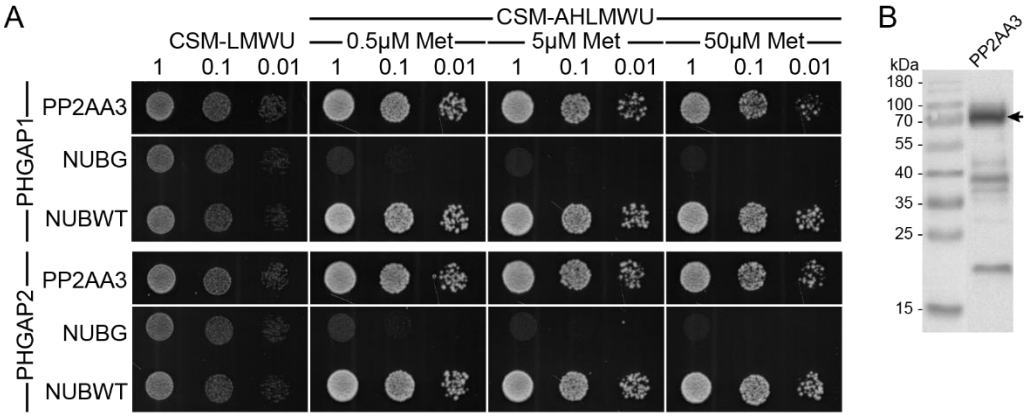

Figure 9: PHGAP1 and PHGAP2 interact with the phosphatase PP2AA3

(A) Yeast mating-based split-ubiquitin system (SUS) assay was performed using PHGAP1 and PHGAP2 as baits (-Cub fusion) and PP2AA3 as prey (NubG- fusion). Yeast diploids of bait plus prey or bait plus controls (NUBG, negative control and NUBWT, positive control) were spotted on CSM-Leu-, Met-, Trp-, Ura- (CSM-LMWU) medium to verify mating. Protein interactions were examined by colony growth on CSM-Ade-, His-, Leu-, Met-, Trp-, Ura- (AHLMWU) with the addition of 0.5 µM, 5 µM or 50 µM methionine. Colonies correspond to culture concentration 1, 0.1 and 0.001 at OD_{600} from left to right. Control plates and experimental plates were scanned after 24 h and 48 h, respectively to monitor colony growth. (B) Western blot confirmed the expression of the prey PP2AA3 (74 kDa, arrow) used in (A). Western blot showing the expression of the baits PHGAP1 and PHGAP2 is depicted in Figure 6C. The assay was performed twice with similar results (second assay, Haller, 2019).

Discussion

Potential functions of PHGAPs during cell division

In our previous study, we identified the first GAPs, PHGAP1 and PHGAP2, to be involved in cell division in *Arabidopsis* (Stöckle et al., 2016). Knockdown of *PHGAP1* and *PHGAP2* in *phgap1-1 phgap2-1* resulted in a fairly mild cell division phenotype compared to *pok1-1 pok2-3* (Stöckle et al., 2016). This could be due to the amount of PHGAP2 that is still active in the double mutant, since the *PHGAP2* transcript was not fully abolished in *phgap2-1* (Stöckle et al., 2016). Another reason could be, that the gene expression of PHGAP1 and PHGAP2 in the root tissue are overlapping, but they are not identical (Stöckle, 2015; Stöckle et al., 2016). There could be also redundant functions with members of the CRIB domain-containing ROPGAPs, the second group of ROP inactivators in *Arabidopsis* (Schaefer et al., 2011). Redundancy among the two GAP groups has been already shown for REN1 and ROPGAP1 during pollen tube tip growth (Hwang et al., 2010). However, so far there was no ROPGAP identified in cell division. PHGAP1 and PHGAP2 accumulated in a POK-dependent manner at the division site during metaphase where they remained until the end of cytokinesis (Stöckle et al., 2016). This observation, together with the presence of obliquely oriented phragmoplasts in *phgap1-1 phgap2-1*, would suggest a function of PHGAPs in phragmoplast guidance. However, *phgap1-1 phgap2-1* displayed not only oblique phragmoplasts, but also oblique PPBs (Stöckle et al., 2016). In addition, POK1 was recruited to the division site predicted by these oblique PPB (Stöckle et al., 2016). Therefore, the oblique phragmoplasts are most likely a downstream effect of the already misaligned PPBs/division sites in *phgap1-1 phgap2-1*, indicating that PHGAPs are required for the correct positioning of the PPB/division sites. In contrast to POK1, which is specifically expressed in cell division (Lipka et al., 2014), PHGAPs displayed also cytosolic and plasma membrane localization in interphase cells. Therefore, PHGAPs have probably also other functions beyond cell division. The question arises now, why are PHGAPs recruited to the division site in metaphase and what might be their function there, if they are not mediating the guidance of the phragmoplast. Since the cell division phenotype in *phgap1-1 phgap2-1* is most likely caused by the already mispositioned PPBs, it is necessary to dissect the function of PHGAPs during PPB positioning and their activities at the division site from metaphase. In this direction, one approach would be to introduce a PHGAP version in *phgap1-1 phgap2-1* that is degraded before cytokinesis to observe the effects on the remaining cell division process.

Are PHGAPs functioning as ROP inactivators during cell division?

In general, GAPs are known to mediate ROP inactivation by stimulating the GTP-hydrolysis function of ROPs and are therefore key players in ROP regulation (Hwang et al., 2008; Klahre and Kost, 2006; Wu et al., 2000). Are PHGAPs then inactivating ROP activity during cell division? The functional requirement of the PHGAP GAP domain for cell division plane selection and the ability of PHGAPs to interact with ROPs, indeed implies a role for PHGAPs in ROP inactivation during cell division (Stöckle et al., 2016). So far, it is unknown which ROPs are involved in cell division in the root meristem. Until now, only ROP3 has been described to play a role in cell division. Loss of ROP3 activity affected embryo development in a comparable manner to *phgap1-1 phgap2-1*, suggesting a role for PHGAPs in ROP3 inactivation during embryo formation (Huang et al., 2014; Stöckle et al., 2016). However, ROP3 is only expressed in the quiescent centre, columella stem cells, in columella cell layers and stele cells of the root meristem (Huang et al., 2014). Therefore, ROP3 has only some overlap in expression pattern with PHGAPs in the root meristem and is probably not the only potential target of PHGAP inactivation during root cell division. *Arabidopsis*, contains 10 other ROPs that could be considered as inactivation targets of PHGAPs. To analyse, whether ROPs function during cell division at all, one could use the CRIB domain of the ROP interactor RIC1, that was shown to bind to active ROPs (Klahre and Kost, 2006). RFP-CRIB-RIC1 expressed under the Ubiquitin promoter was labelling active ROPs at the plasma membrane and in the cytosol in the root meristem and leaf pavement cells (Späth, 2017). However, to identify ROPs participating in cell division, RFP-CRIB-RIC1 should be expressed under a cell division specific promoter followed by immunoprecipitation mass spectrometry (IP-MS) analysis. A second approach could be the detailed analysis of *rop* mutants regarding cell division defects. It is likely that ROPs functioning in cytoskeletal reorganization in mitotic and cytokinetic structures or vesicle trafficking during cell division, as they fulfil this function also in other developmental processes (reviewed in Craddock et al., 2012). Therefore, one possible PHGAP function in cell division might be the regulation of ROP activity in PPB orientation. As mentioned above, PHGAPs function not only in PPB positioning, they are also accumulated at the division site from metaphase to the end of cytokinesis. Actin is diminished at the division site from prometaphase through anaphase, known as the actin-depleted zone (ADZ) (Cleary and Smith, 1998; Mineyuki and Palevitz, 1990). Although, the time frames of PHGAP accumulation and actin depletion at the division site are not completely overlapping, it might be possible that PHGAPs mediate inactivation of ROPs at the division site to create the ADZ. Indeed, ROP1 activity decrease actin filament accumulation during pollen tube tip growth, where ROP1-RIC3 interaction led to an increase in Ca^{2+} level followed by actin filament disassembly (Hwang et al., 2008). A first attempt to investigate PHGAP involvement in ADZ establishment could be to analyse actin localization in dividing *phgap1-1 phgap2-1* double mutant cells.

Requirement of PHGAP domains for function and localization

PHGAPs contain three different domains: at the N-terminus a pleckstrin homology domain, a central GAP domain and at the C-terminus predicted coiled coil domains (Hwang et al., 2008). Pleckstrin homology domains are known for their phosphoinositide binding ability (Lemmon, 2008). Recently, this binding ability was confirmed for PHGAP1 and PHGAP2 as they were found to bind to phosphatidylinositol 4-phosphate (PtdIns(4)P), PtdIns(5)P, PtdIns(3,5)P_2 and PtdIns(4,5)P_2 (Krieger, 2014; Kulich et al., 2020). Additionally, PHGAP1 was binding to PtdIns(3)P and PHGAP2 to PtdIns(3,4)P_2, PtdIns(3,4,5)P_3 and phosphatidic acid (Krieger, 2014; Kulich et al., 2020). However, whether the PH domain is important for PHGAP function during cell division has still to be clarified. A functional GAP domain was important for PHGAP function during cell division, but was not required for division site localization (Stöckle et al., 2016). Analysis of PHGAP coiled coil domain deletion mutants revealed that the whole C-terminal part was needed for PHGAP1 and PHGAP2 function and localization at the division site and for plasma membrane localization in general. Since the root meristem phenotype was most likely caused by already misoriented PPBs/division sites, these results propose that plasma membrane localization of PHGAPs prior cell division, is required for correct PPB orientation establishment. Though, when only the last predicted coiled coil domain was absent, GFP-PHGAP2$^{1\text{-}764}$ was still able to localize at the plasma membrane and to rescue the root meristem mutant phenotype, but localization at the division site was impaired. This would suggest that, either POK1-dependent recruitment of PHGAPs during metaphase is not important for further cell division or, what is more likely, this further confirms redundancy with ROPGAPs as already indicated by the mild *phgap1-1 phgap2-1* phenotype. To confirm these hypotheses, PPB and phragmoplast orientation in the root meristem should be analysed in *pPHGAP2:GFP-PHGAP2$^{1\text{-}764}$ phgap1-1 phgap2-1* rescue lines and *ropgap* mutants.

Therefore, our data suggests that there are two possible functions for the PHGAP coiled coil domains. Either they are needed for transport of the protein to the localization sites or they are required for interaction with unknown plasma membrane bound proteins and POK1 at the division site. For the closest homolog of PHGAPs, REN1, Hwang et al., suggested that REN1 is associated with exocytic vesicles via its C-terminal domain and reaches the plasma membrane of the pollen tube apex via vesicle trafficking (Hwang et al., 2008). Hence, it is possible that also the PHGAP coiled coil domain is necessary for vesicle association and transport to the plasma membrane and division site. To test the second hypothesis, a yeast-mating-based split ubiquitin assay was performed to analyse which PHGAP1 and PHGAP2 domains are required for interaction with the POK1 coiled coil domain containing C-terminal part (Lotz, 2018). POK1$^{1683\text{-}2066}$ was not interacting with PHGAP1 and PHGAP2 when the PH domain or the last predicted coiled coil domain of PHGAP2 was absent (Lotz, 2018). However, POK1$^{1213\text{-}2066}$ was able to interact with PHGAP1 and PHGAP2 independently of the absence

or presence of the PH domain or the coiled coil domains (Lotz, 2018). This would suggest that the PHGAP1 and PHGAP2 coiled coil domain is not necessarily needed for interaction with POK1 and that the interaction is probably facilitated by the central GAP domain. In contrast, in the Y2H screen, where PHGAPs were initially identified as interaction partners of POK1, POK1$^{1683-2066}$ was interacting with C-terminal fragments of PHGAP1 and PHGAP2 (Sabine Müller, unpublished data). Collectively, these data would support the view that the transport of PHGAPs towards the cortical division site and possibly not the interaction with POKs is mediated by the PHGAP C-terminus, but further studies are required *in planta*.

Furthermore, PHGAP1 and PHGAP2 were able to form homo- and heterodimers in a split-ubiquitin assay independently despite the absence of the N-terminal or C-terminal domains. This would suggest, that PHGAP1 and PHGAP2 probably dimerize via their GAP domain, which was already previously shown for ROPGAP2 (Schaefer et al., 2011). It would be interesting to further investigate if PHGAPs dimerize also *in planta* and whether the dimerization is required for function. ROPGAP2 was not only able to dimerize, but was also shown to form a 2:2 complex with ROPs (Schaefer et al., 2011). Further analysis might reveal whether PHGAP1 and PHGAP2 form also a 2:2 complex with ROPs or how they interact with POKs.

Are PHGAPs phosphoregulated?

PHGAP1 and PHGAP2 contain several predicted phosphorylation sites, suggesting potential phospho-regulation of these proteins. Mutation of one of those phosphorylation sites (S447), in which created a phospho-deficient mutant (S447A), resulted in earlier arrival of PHGAP2 at the division site, as it was already accumulated at the CDZ during preprophase. This would suggest, that phosphorylation is important for the timely localization of PHGAPs at the division site. However, PHGAPs contain several potential phosphorylation sites, so further characterization of PHGAP function with additional mutated phosphorylation sites would help to clarify any importance of the phosphorylation status of those sites. In general, phosphorylation is mediated by kinases, but which kinase might be involved in PHGAP phosphorylation is still elusive. However, our experiments revealed that the phosphatase complex TTP might be involved in the dephosphorylation of PHGAPs. Indeed, PHGAP1 and PHGAP2 were interacting with the scaffolding subunit A of the TTP-complex, PP2AA3. Additionally, PHGAP2 accumulation as well as POK1 recruitment at the division site was delayed in *trm6 trm7 trm8* mutants (Schaefer et al., 2017; present thesis). TRM mediates targeting of the TTP complex to the cytoskeleton (Drevensek et al., 2012). Therefore, late POK-dependent PHGAP2 arrival at the division site could be either a downstream effect of already delayed POK1 recruitment to the CDZ in *trm6 trm7 trm8* or caused by absent PHGAP2 dephosphorylation by a mislocalized TTP-complex as the TRM mediated targeting function is

missing (Schaefer et al., 2017; Stöckle et al., 2016). Abolished TON1, FASS or TRM6-8 function leads to a lack of PPB formation, which was not the case in *phgap1-1 phgap2-1* double mutants (Schaefer et al., 2017; Spinner et al., 2013; Torres-Ruiz and Jürgens, 1994; Traas et al., 1995). However, our previous results pointed to a function for PHGAPs in PPB orientation rather than in PPB formation. So far, it is also unclear whether missing phosphorylation of PHGAPs also interferes with PPB orientation. Further analysis of PPB orientation in GFP-PHGAP2^{S447A} *phgap1-1 phgap2-1* should be performed in order to clarify the latter. All in all, phosphorylation-deficiency leads to early PHGAP accumulation at the division site, while probably absent dephosphorylation results in later PHGAP recruitment, suggesting that the PHGAP phosphorylation status has to be timely regulated.

7.2 Characterization of PHGAP functions during pavement cell shape establishment

Manuscript: Cell polarity establishment requires spatial localization of GTPase activating proteins

Theresa Lauster[1], Dorothee Stöckle[2], Sabine Müller[1]

[1]Developmental Genetics
Centre for Plant Molecular Biology (ZMBP)
University of Tübingen
Auf der Morgenstelle 32
72076 Tübingen

[2]Plant Cell Biology
Department of Plant and Microbial Biology
University of Zurich
Zollikerstrasse 107
8008 Zürich

Abstract

Regulation of polarized growth is essential for proper formation of several plant organs and tissues, including pollen tubes, root hairs and leaf pavement cells. Rho of plants (ROPs), acting as small molecular switches, are key players in this process. During differentiation of *Arabidopsis thaliana* leaf epidermis, ROP2 and ROP6 have antagonistic functions in the formation of the characteristic pavement cell jigsaw puzzle shape by inducing the reorganization of the cytoskeleton in lobe and indentation regions, respectively. Here, we identified two pleckstrin homology (PH) containing GTPase activating proteins (GAPs), PHGAP1 and PHGAP2, that function redundantly during the morphogenesis of pavement cells. In general, GAPs mediate ROP inactivation by stimulating their intrinsic GTP-hydrolysis function. Loss of *PHGAP1* and *PHGAP2* function in the *phgap1 phgap2* double mutant resulted in a severe reduction of pavement cell shape complexity. Both PHGAPs were recruited, in a microtubule dependent manner, on the anticlinal face of pavement cell indentation regions. PHGAPs interacted specifically with ROP2 likely fine tuning its activity. Consistently, increased active ROP2 levels in *phgap1 phgap2* double mutant support the view that PHGAPs inactivate ROP2 in pavement cell indentations regions. In conclusion, PHGAP-mediated regulation of ROP2 activity in this region is important for correct polarity establishment and proper puzzle shape cell formation.

Results

PHGAP1 and PHGAP2 function redundantly in pavement cell shape establishment

PHGAP1 and PHGAP2 showed expression in several polar growing organs like primary and lateral roots, root hairs and young leaves (Stöckle et al., 2016). To investigate whether PHGAPs play a role in polarized growth we analysed different *phgap* mutant alleles (Figure S1A). Semi-quantitative RT-PCR was used to assess the PHGAP transcript levels in the different T-DNA insertion lines. It was found that expression of PHGAP was completely abolished in *phgap1-2* and *phgap2-2* (Figure S1C-D), while in *phgap1-1* and *phgap2-1* was drastically reduced (Stöckle et al., 2016). *phgap* single mutants displayed no obvious phenotype, therefore, we generated different *phgap1-1 phgap2-1*, *phgap1-2 phgap2-2* and *phgap1-1 phgap2-2* double mutant combinations. 10-day old *phgap1 phgap2* double mutant seedlings, especially *phgap1-1 phgap2-1*, displayed more lancet-shaped cotyledons in comparison to wild type (Figure 1A). The cotyledon width/length ratio was determined revealing that all *phgap1 phgap2* double mutant combinations had a statistically significant smaller width/length ratio compared to wild type, with that of *phgap1-1 phgap2-1* being the most affected (Figure 1B). During 8-leaf stage of *phgap1-1 phgap2-1* plants it was found that not only the shape of cotyledons was affected, but also that the shape of emerging young leaves was slightly altered in comparison to wild type leaves (Figure 1C). These alterations in cotyledon and leaf shape of *phgap1 phgap2* double mutants led us to focus on the involvement of PHGAP1 and PHGAP2 during multipolar growth of pavement cells. As a first step, we examined individual characteristics of pavement cell shape (area, perimeter, circularity) of 10-day old cotyledon pavement cells. *phgap1-1* and *phgap2-1* cotyledon pavement cells displayed no phenotypical differences compared to wild type (Figure S1E-H). *phgap1-2* and *phgap2-2* pavement cells showed a considerably significantly smaller perimeter and larger circularity than wild type, while their area was not affected (Figure S1I-L). The single mutant pavement cell phenotype of *phgap1-2* and *phgap2-2* was fairly mild. Therefore, we analysed the pavement cell shape of different *phgap1 phgap2* double mutant combinations (10-day old cotyledons) to investigate whether PHGAPs have redundant functions in pavement cell formation (Figure 1D-G, 1J-L). *phgap1 phgap2* double mutants showed a significantly smaller perimeter (Figure 1K) and a higher circularity (Figure 1L), while pavement cell area (Figure 1J) was not affected in comparison to wild type. The double mutant combination *phgap1-1 phgap2-1* showed the most severe phenotype, displaying a dramatic loss of pavement cell shape complexity and therefore, was used for further studies (Figure 1E). The pavement cell phenotype in *phgap1-1 phgap2-1* could be fully restored by expressing either *pPHGAP1:GFP-gPHGAP1* (Figure 1H, 1M-O) or *pPHGAP2:GFP-gPHGAP2* (Figure 1I, 1P-R). PHGAP1 and PHGAP2 share at the amino (N) terminal a pleckstrin homology (PH) domain, a central GTPase activating protein (GAP) domain containing a functionally critical and conserved

arginine (Figure S1B). At the carboxy (C) terminal coiled coil domains are predicted. Interestingly, loss of pavement cell shape complexity could not be rescued with *pPHGAP1:GFP-PHGAP1*^{R203L} (Figure S1M) or *pPHGAP2:GFP-gPHGAP2*^{R198L} (Figure S1N) where the function of the GAP domain was abolished by the substitution of the conserved arginine (R) by leucine (L). Taken together, these data indicate that PHGAP1 and PHGAP2 act redundantly and that their catalytic function is important for pavement cell shape establishment.

Microtubule organization in *phgap1-1 phgap2-1* pavement cells was only mildly affected compared to wild type

GAPs are known inactivators of ROPs in various developmental processes. ROP2 and ROP6 have been reported to act in antagonistic cell polarity signalling pathways, leading to reorganization of the cytoskeleton required for the establishment of the characteristic pavement cell jigsaw puzzle form (Fu et al., 2005; Fu et al., 2002; Fu et al., 2009). As pavement cell complexity is dramatically reduced in *phgap1-1 phgap2-1* (Figure 1E), the question arises whether PHGAP1 and PHGAP2 interfere with ROP2 or ROP6 function during pavement cell shape establishment. First, we compared the microtubule organization in pavement cells of *phgap1-1 phgap2-1* and wild type. Therefore, using the microtubule reporter *35S:GFP-MAP4* (Marc et al., 1998), we examined microtubule orientation in neck regions and central cell regions (region outside of lobe and indentation, Figure S2) of the periclinal face in 3-day old *phgap1-1 phgap2-1* and wild type pavement cells. We determined the microtubule anisotropy with the ImageJ plugin Fibril Tool (Boudaoud et al., 2014). As previously reported (Sampathkumar et al., 2014), wild type pavement cells displayed a statistically significant higher anisotropy in neck regions compared to central regions where microtubule bundles were more randomly oriented (Figure 2A-B). However, the microtubule orientation in *phgap1-1 phgap2-1* neck and central regions was comparable to their orientation in wild type (Figure 2A-B). In addition, we analysed the microtubule density in lobes compared to the respective indentation regions, since it was previously reported that the amount of microtubules is reduced in wild type lobe regions (Armour et al., 2015). We measured the mean fluorescent intensity in lobes and the corresponding indentation regions in neighbouring cells of 3-day old wild type and *phgap1-1 phgap2-1* cotyledon pavement cells and calculated the lobe/indentation signal intensity ratio. The lobe/indentation signal intensity ratio was significantly higher in *phgap1-1 phgap2-1* compared to wild type, indicating that the difference in microtubule density between lobe and indentation regions was less pronounced in the double mutant (Figure 2C-D). In a scenario where PHGAP1 and PHGAP2 deactivate ROPs during polarity establishment in pavement cells, we would expect the target ROP to be locked in its GTP-bound form and rendered constitutively active in *phgap1-1 phgap2-1*. It has been previously described that

constitutive expression of ROP6 leads to parallel microtubule orientation, while constitutive expression of ROP2 results in randomly oriented microtubules in developing pavement cells (Fu et al., 2002; Fu et al., 2009). To test the hypothesis described above, we constitutively expressed ROP2 and ROP6 and analysed the overall microtubule anisotropy in 3-day old pavement cells and compared it with *phgap1 phgap2* double mutants and wild type of the same age. We found no statistically significant difference in microtubule anisotropy between wild type and *phgap1-1 phgap2-1* and between *phgap1-1 phgap2-1* and *ca-rop2* (Figure 2E-F). However, the microtubule anisotropy of *phgap1-1 phgap2-1* pavement cells was significantly different from *ca-rop6* which showed the highest anisotropy (Figure 2E-F). In summary these data show that the microtubule organization in *phgap1-1 phgap2-1* is only slightly affected in contrast to wild type and resembled the microtubule orientation of *ca-rop2* and not *ca-rop6*, pointing to ROP2 as inactivation target of PHGAP1 and PHGAP2.

PHGAP1 and PHGAP2 interact with ROP2 and active ROP2 protein levels are elevated in *phgap1-1 phgap2-1*

Based on the results described above, we wanted to investigate whether active GTP-bound ROP2 and ROP6 protein levels were increased in *phgap1-1 phgap2-1*. Thus, we performed pull-down experiments using the ROP effector RIC1 (His-MBP-RIC1 conjugated beads), conjugated to agarose beads and *Arabidopsis* leaf/hypocotyl protein extracts stably expressing HA-mCherry-ROP2 or HA-mCherry-ROP6 (Figure 3A-B, S3D-G). RIC1 was previously shown to pull-down only active ROPs (Wu et al., 2001). The protein amount of active ROP2 was increased in *phgap1-1 phgap2-1* double mutant compared to wild type, while the active ROP6 protein levels were not affected (Figure 3C). To conclude, which ROP is interacting with PHGAP1 and PHGAP2 we conducted co-immunoprecipitation experiments in *Arabidopsis* and performed mating-based split-ubiquitin interaction assays in yeast (Grefen et al., 2009). Using protein extracts from 5-day old seedlings, we observed that HA-mCherry-ROP2 could be immunoprecipitated with GFP-PHGAP2 (Figure 3D), while HA-mCherry-ROP6 was not (Figure 3E). Additionally, PHGAP1 and PHGAP2 were found to interact with ROP2, but not with ROP6 in mating-based split-ubiquitin interaction assay (Figure S3A-C). These data indicate that PHGAP1 and/or PHGAP2 interact and inactivates ROP2 but not ROP6.

PHGAP1 and PHGAP2 are enriched in apices of undulating indentation regions

For further characterization of PHGAP1 and PHGAP2 function, we examined their subcellular localization using the full genomic constructs *pPHGAP1:GFP-PHGAP1* and *pPHGAP2:GFP-PHGAP2* (Stöckle et al., 2016) expressed in *phgap1-1 phgap2-1* background. Both PHGAPs were non-uniformly distributed along the plasma membrane of 3-day old cotyledon pavement cells. Both PHGAP1 and PHGAP2 showed local enrichments along the plasma membrane

(Figure 4A and S4A). A three-dimensional (3D) reconstruction of GFP-PHGAP1 or GFP-PHGAP2 expressing pavement cells confirmed that localized PHGAP stripes were most pronounced along the anticlinal face (Figure 4B-C, S4B). We examined this localization pattern in more detail and discovered that the GFP-PHGAP1 stripes were not restricted to the anticlinal face but continued into the periclinal face, although there the stripes rapidly faded (Figure 4D-E). Furthermore, the 3D analysis showed that GFP-PHGAP1 enrichments reside on the indentation side and not on the lobe side of a curvature between neighbouring cells (Figure 4D-E).

We were wondering when during pavement cell development PHGAP1 and PHGAP2 start to accumulate along the anticlinal face. Thus, we investigated the timing of GFP-PHGAP1 and GFP-PHGAP2 arrival along the anticlinal face with respect to the developmental stage of the pavement cells. Therefore, we determined the curvature fitting circle, in which curvatures at the beginning of their bulging possessed a larger fitting circle compared to curvatures that were already well pronounced (Figure 4F). Based on the ratio of the sector size divided by the radius, the curvatures were classified into classes representing different stages (Figure 4G). Curvature class I denotes straight cell walls, while classes II-V cover different degrees of bulging (Figure 4H-I). Different curvatures of 2-3-day old cotyledon pavement cells were analysed by generating a plot profile (Belteton et al., 2018), that represents GFP-PHGAP accumulation (peaks) relative to the anticlinal face of a selected curvature (Figure 4K-L). The curvature was further subdivided in three regions: the ‘apex’ which is defined as the central 50% at full width half maximum (FWHM) of the curvature, the ‘flank’ region representing the remaining 12.5% on either apex site at FWHM and ‘outside’ that covers the remaining curvature region (Figure 4J; Belteton et al., 2018). GFP-PHGAP1 and GFP-PHGAP2 anticlinal face analysis revealed that straight pavement cell walls already displayed GFP-PHGAP1 and GFP-PHGAP2 accumulation and that these GFP-PHGAP1 and GFP-PHGAP2 peaks were predominantly localized in the apex region, some in the flank region and only a minor proportion outside of curvatures in classes I-V (Figure 4M and S4C). Furthermore, we observed that the amount of GFP-PHGAP1 and GFP-PHGAP2 peaks (apex and flank region) was considerably increased with increasing curvature bulging (Figure 4N and S4D). However, we also noticed that, irrespective of the stage, not all curvatures exhibited a visible GFP-PHGAP1 and GFP-PHGAP2 accumulation along the anticlinal face (Figure S4E-F). Taken together the data indicate that PHGAP1 and PHGAP2 accumulate already on straight pavement cell walls on the anticlinal face. Furthermore, PHGAPs accumulate predominantly in apex regions of indentations with an increasing amount of PHGAP stripes with progressive curvature formation.

PHGAP localize along the anticlinal face of developing pavement cells in a microtubule dependent manner

PHGAP1 and PHGAP2 localization on the anticlinal face of pavement cells is reminiscent of microtubule distribution (Belteton et al., 2018). Therefore, we co-expressed GFP-PHGAP1 and the microtubule reporter RFP-MBP (Lipka et al., 2014) in *phagp1-1 phgap2-1* double mutants and investigated their subcellular localization in cotyledon pavement cells. GFP-PHGAP1/microtubule plot profiles were used to determine the co-localization frequency of both signals in apex, flanking region or outside of a curvature. GFP-PHGAP1 and microtubules co-localized along the anticlinal face, showing clear overlapping signal peaks in the generated plot profiles (Figure 5A-B). About 70-80% of GFP-PHGAP1 peaks displayed clear co-localization, around 20% showed a partial overlap and only 0-2% were not co-localized with microtubule bundles in all regions (Figure 5C). Moreover, mutation of the conserved arginine (R) to leucine (L) in GFP-PHGAP1^{R203L} and GFP-PHGAP2^{R198L} had no effect on anticlinal face accumulation or co-localization with microtubules indicating that a functional GAP domain is not required for localization (Figure S5A).

To assess whether GFP-PHGAP1 localization along the anticlinal face was microtubule dependent, we used the microtubule depolymerizing drug Oryzalin (Morejohn et al., 1987). 24 h after treatment with 100 µm Oryzalin or mock treatment respectively, we counted the GFP-PHGAP1 and microtubule peaks in anticlinal face plot profiles. Most of the microtubule bundles on the anticlinal face were depolymerized in the presence of Oryzalin and the GFP-PHGAP1 accumulation was also lost, indicating that PHGAP localization on the anticlinal face is microtubule dependent (Figure 5D and S5B). This suggest also that microtubules are present at the anticlinal face prior PHGAPs. To confirm the latter, we analysed microtubule and GFP-PHGAP1 and GFP-PHGAP2 signal distribution along the anticlinal face of straight cell walls. Only 50-70% of the analysed straight cell walls that showed microtubule bundles displayed also GFP-PHGAP1 and GFP-PHGAP2 signals, while the signals were never detected along anticlinal faces without co-localizing microtubule signal (Figure 5E). These results underline that PHGAP1 and PHGAP2 are recruited to pre-existing microtubules on the anticlinal face.

Considering that ROP2 is known to induce actin filament accumulation in lobe regions during pavement cell development (Fu et al., 2005; Fu et al., 2002) and that we identified ROP2 as interaction partner of PHGAP1 and PHGAP2, we further investigated whether PHGAPs co-localize with actin filaments. We co-expressed GFP-PHGAP1 and the actin reporter LifeAct-RFP (Cvrčková and Oulehlová, 2017) in *phgap1-1 phgap2-1* double mutant background and examined their subcellular localization pattern in pavement cells. Reconstructions of the anticlinal faces revealed that GFP-PHGAP1 and LifeAct-RFP did not co-localize and that the signal peaks in the plot profile generated were not overlapping (Figure S6A-B). Co-localization frequency analysis in apex, flank or outside of the curvatures revealed that most of the GFP-

PHGAP1/LifeAct-RFP peaks did not overlap (86-96%), some showed a partial overlap (2-14%) and only 2% in the flank region displayed co-localization (Figure S6C). Furthermore, we treated 3-day old GFP-PHGAP1/Life-Act-RFP expressing seedlings with the actin filament disrupting drug Latrunculin B (LatB) for 24 h (Spector et al., 1983) to investigate any PHGAP1 localization dependency on actin filaments. Most of the actin filaments on the periclinal face were effectively destroyed after treatment with 1 µM LatB for 24 h (Figure S6D). By counting the number of GFP-PHGAP1 and LifeAct-RFP peaks in anticlinal face plot profiles, we discovered that the few actin filaments present along the anticlinal face were dramatically reduced by LatB treatment (Figure S6E). However, the number of GFP-PHGAP1 peaks on the anticlinal face was only slightly affected by LatB (Figure S6E) as GFP-PHGAP1 accumulation was clearly visible along the anticlinal faces (Figure S6F). The GFP-PHGAP1 distribution in apex, flank and outside of curvatures was also not affected by LatB treatment (Figure S6G). These data indicate that PHGAP accumulates on the anticlinal face independently of the actin cytoskeleton.

PHGAP2 C-terminal domain is required for pavement cell shape establishment and anticlinal face localization

It has been previously shown, that the C-terminal part of the PHGAP1 and PHGAP2 homolog REN1 is important for REN1 localization at the apical plasma membrane in pollen tube elongation (Hwang et al., 2008). Thus, we tested whether the PHGAP1 and PHGAP2 C-terminal part was important for anticlinal face localization and pavement cell shape establishment by generating two PHGAP2 truncated versions. In the first (*pPHGAP2:GFP-gPHGAP2*$^{1-764}$) the last predicted coiled coil domain was deleted and in the second (*pPHGAP2:GFP-gPHGAP2*$^{1-566}$) the entire C-terminal part was absent (Figure 6A). Expression in the *phgap1-1 phgap2-1* double mutant background and pavement cell shape analysis in 10-day old cotyledons revealed, that GFP-PHGAP2$^{1-764}$ was fully rescuing the *phgap1-1 phgap2-1* pavement cell phenotype, while expression of GFP-PHGAP2$^{1-566}$ was insufficient for rescue (Figure 6B-E). Furthermore, we investigated whether GFP-PHGAP2$^{1-764}$ and GFP-PHGAP2$^{1-566}$ were co-localizing with the microtubule reporter RFP-MBD along the anticlinal face in 3-day old cotyledon pavement cells. GFP-PHGAP2$^{1-764}$ showed a distribution comparable to full length GFP-PHGAP2, co-localizing with microtubules on the anticlinal face (Figure 6F). In contrast, GFP-PHGAP2$^{1-566}$ displayed only diffuse localization but no distinct accumulation along the anticlinal face (Figure 6G), indicating that the C-terminal domain is critical for anticlinal face recruitment and consequently for pavement cell shape establishment.

Discussion

In this study, we showed that PHGAP1 and PHGAP2 have essential functions during pavement cell shape establishment. Both PHGAPs co-localized with microtubules on the anticlinal face of pavement cell indentations. Accumulation of PHGAPs on the anticlinal face was dependent on microtubules but independent of actin filaments. Increased active ROP2 protein levels in *phgap1-1 phgap2-1* point to compromised inactivation of ROP2 and the interaction analysis confirmed that PHGAPs interacted with ROP2. During pavement cell morphogenesis ROP2 and ROP6 activity has to be tightly controlled and restricted to lobe and indentation region, respectively as overexpression of either ROP2 or ROP6 leads to severe loss of pavement cell shape complexity (Fu et al., 2002; Fu et al., 2009). Taken together our results support the view that PHGAP1 and PHGAP2 redundantly inactivate ROP2 in indentation regions of pavement cell, creating ROP2 activity gradients that are necessary for the maintenance of cell polarity (Figure 7). Consequently, the inactivation of ROP2 by PHGAP1 and PHGAP2 allows ROP6 to bundle microtubules within indentation regions. The amount of PHGAP1 and PHGAP2 accumulation on the anticlinal face increases proportionally with increasing curvature bulging, which is in line with an increasing indentation surface that has to be free of ROP2 activity.

Are PHGAP1 and PHGAP2 initiating the formation of the curvature?

PHGAP1 and PHGAP2 started to appear on the anticlinal faces of epidermal cells already before lobe initiation was recognizable. This raises the question whether PHGAP1 and PHGAP2 initiate the formation of curvatures. The microtubule dependency of PHGAP1 and PHGAP2 localization and the fact that we observed straight anticlinal cell walls with microtubules in the absence of PHGAP1 and PHGAP2 accumulation, suggest that microtubule bundles are recruited first. Recently, Pan et al. showed that auxin induced nanoclustering of the transmembrane receptor kinase 1 (TMK1) leads to active ROP6 nanoclustering and consequently to local microtubule bundling which in turn restrict diffusion of TMK1 nanoclusters in a positive feedback loop (Pan et al., 2020). Furthermore, this positive feedback loop is thought to lead to the formation of polarized ROP6 domains prior the beginning of curvature bulging (Pan et al., 2020). This would suggest that curvature formation includes first the auxin-TMK1 induced recruitment of active ROP6 that leads to microtubule reorganization, followed by the accumulation of PHGAP1 and PHGAP2 and restriction of ROP2 activity. Inhibition of ROP2 activity in indentation regions is essential because the active ROP2 sequesters the effector RIC1 from microtubules and thereby prevents microtubule bundling (Fu et al., 2009). Since ROP6 is recruited to TMK1 nanoclusters localized in indentation regions, it is probably not necessary to have other GAPs that inactivate ROP6 in lobe regions, lacking those nanoclusters (Pan et al., 2020). Another mechanism proposed for initiation of lobe formation

is that mechanical stress, caused by differences in wall stiffness and resulting differential expansion of future lobe and indentation regions, acts upon the future curvature side (Altartouri et al., 2019; Bidhendi et al., 2019). This locally generated stress hotspots reaching the maximum tension in indentation regions leads to the alignment of microtubule bundles (Bidhendi et al., 2019; Hamant et al., 2008; Sampathkumar et al., 2014). Therefore, it would be interesting to examine whether PHGAP accumulation is triggered in response to mechanical stress. Overall, although PHGAP1 and PHGAP2 do not initiate curvature formation, their recruitment and activity seem to be critical for cell polarity maintenance and subsequent differentiation of epidermal cells.

Which proteins recruit PHGAP1 and PHGAP2 to the anticlinal face and what specifies the ROP inactivation target?

PHGAP1 and PHGAP2 decorated only a portion of microtubules along the anticlinal cell faces. This suggests that there must be additional proteins or regulation steps involved in defining the side of PHGAP1 and PHGAP2 enrichment. Furthermore, since PHGAPs are able to interact with several ROPs, there must be also a tightly regulated process that specifies their ROP target in space and time (Stöckle et al., 2016). Recently, characterization of ARMADILLO REPEAT ONLY (ARO) proteins revealed that they act as scaffolds for active ROPs and RENGAP/PHGAPs during root hair and trichome development (Kulich et al., 2020). AROs bound to anionic phospholipids at the plasma membrane, where they formed a complex with PHGAPs and active ROPs (Kulich et al., 2020). Loss of ARO function in *aro2 aro3 aro4* among others resulted in loss of ROP2 polarization at the plasma membrane during root hair growth, suggesting compromised regulation of ROP2 activity and distribution (Kulich et al., 2020). Interestingly, ARO1-4 interacted with PHGAP1 and PHGAP2 however the *aro2aro3aro4* triple mutant displayed no pavement cell phenotype indicating that AROs have probably no function during pavement cell shape establishment and are not involved in PHGAP1 and PHGAP2 targeting to indentation regions (Kulich et al., 2020). Another possible candidate for PHGAP1 and PHGAP2 microtubule dependent accumulation on the anticlinal face of indentation regions could be IQ67 DOMAIN 5 (IQD5). *iqd5* loss-of-function mutants displayed also a disturbance of pavement cell shape complexity, although it was not as severe as in *phgap1-1 phgap2-1* double mutants (Liang et al., 2018; Mitra et al., 2019). Furthermore, IQD5 co-localizes with cortical microtubules in vegetative tissues and is probably involved in cellulose deposition and Ca^{2+} signalling in pavement cell growth as well as in the regulation of microtubule dynamics (Liang et al., 2018; Mitra et al., 2019). However, IQD5 is decorating all cortical microtubules, therefore it seems less likely that IQD5 mediates polar accumulation of PHGAP1 and PHGAP2. To clarify, whether or not PHGAP1 and PHGAP2 bind directly to microtubules, a microtubule co-sedimentation assay would clarify the matter. Even if PHGAP1 and PHGAP2 were able to

bind to microtubules, a mechanism must exist that pre-determines the side of PHGAP1 and PHGAP2 accumulation along the anticlinal face.

Our experiments showed that the C-terminal containing coiled coil domain of PHGAP2 was necessary for localization and for the rescue of the double mutant pavement cell phenotype. As already mentioned, the C-terminus of REN1 was important for apical pollen tube localization, but not for interaction with ROP1 and is proposed to mediate exocytic vesicle association (Hwang et al., 2008). Therefore, it is also possible that PHGAP1 and PHGAP2 get transported via exocytic vesicles to the anticlinal face. This would suggest that absence of PHGAP2$^{1\text{-}566}$ from the indentation side is probably a result of defective protein transport rather than inability of a protein-protein interaction. However, the exocytic vesicle transport in pollen tubes could be abolished by Latrunculin B treatment resulting in a loss of apical REN1 localization (Hwang et al., 2008; Lee et al., 2008). Our Latrunculin B treatment experiment in pavement cells revealed that PHGAP1 stripe localization was not affected along the anticlinal face, which would speak against PHGAP recruitment via exocytic vesicles. As the experiment was conducted with pavement cells that displayed already curvature formation, it is still possible that the initial recruitment of PHGAPs towards the anticlinal face is exocytic vesicle dependent and that PHGAP1 and PHGAP2 remain at the anticlinal face after accumulation. The proportional increase of PHGAP1 and PHGAP2 stripes with increasing curvature bulging suggest that recruitment towards the anticlinal face occurs also in later developmental stages. To assess whether PHGAP1 and PHGAP2 are constantly recruited towards the anticlinal face or only at particular time points a fluorescence recovery after photobleaching (FRAP) analysis could be conducted.

PHGAP1 and PHGAP2 might be also regulated via phosphorylation, as phosphorylation of GDI1 by CPK3 was important for the interaction of GDI1 with ROP2 and ROP6 and consequently for pavement cell development (Wu et al., 2013). PHGAP1 and PHGAP2 contain several predicted phosphorylation sites (PhosPhAt 4.0 (phosphat.uni-hohenheim.de/phosphat.html)), but whether phosphorylation is necessary for their function during pavement cell shape establishment remains to be determined.

Possible PHGAP1 and PHGAP2 function in other polar growing tissues

As PHGAP1 and PHGAP2 probably function in polarity establishment in pavement cells, the question arises whether they perform a similar role during differentiation of other polar growing cell types like pollen tubes or root hairs. Pollen tube growth was not affected in *phgap1-1 phgap2-1* and *pUBN:GFP-PHGAP2* was not able to complement *ren1-4* pollen tube elongation defects, indicating that PHGAP2 does not interfere with pollen tube tip growth (Stöckle, 2015). Only PHGAP1, but not PHGAP2, was expressed in root hairs, implying a role for PHGAP1 in

polarized root hair growth. However, even though the *phgap1-1 phgap2-1* double mutant shows no obvious root hair phenotype, a detailed root hair analysis should be conducted.

Not only investigating the potential role of PHGAP1 in root hairs, but also to investigate PHGAP1 and PHGAP2 regulation and searching for components that specify PHGAP1 and PHGAP2 accumulation on the anticlinal face in pavement cells, could give further insides into PHGAP-mediated cell polarity maintenance.

.

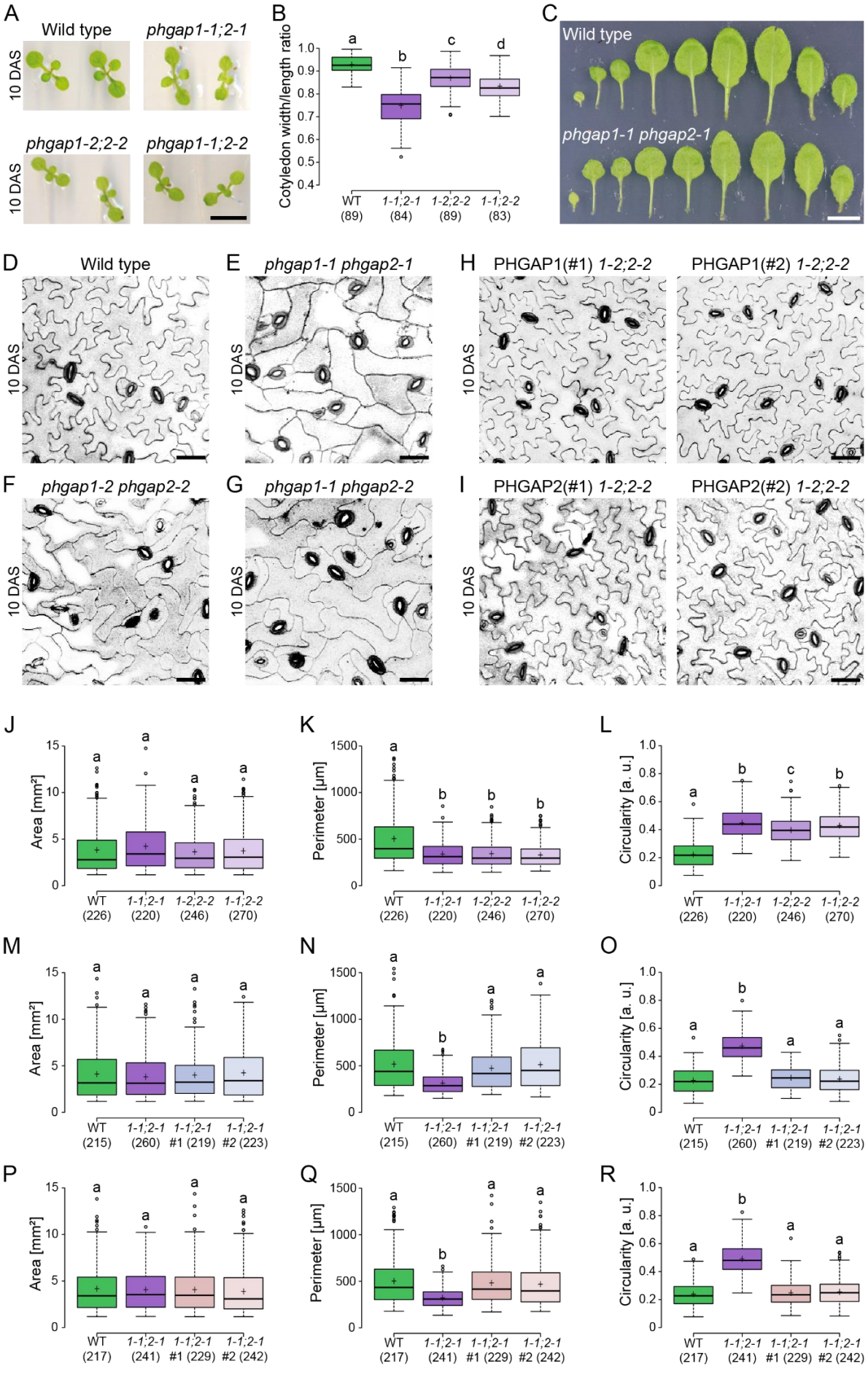
A
Wild type
phgap1-1;2-1
phgap1-2;2-2
phgap1-1;2-2
10 DAS
10 DAS
B
Cotyledon width/length ratio
a
b
c
d
WT (89)
1-1;2-1 (84)
1-2;2-2 (89)
1-1;2-2 (83)
C
Wild type
phgap1-1 phgap2-1
D
Wild type
E
phgap1-1 phgap2-1
H
PHGAP1(#1) 1-2;2-2
PHGAP1(#2) 1-2;2-2
F
phgap1-2 phgap2-2
G
phgap1-1 phgap2-2
I
PHGAP2(#1) 1-2;2-2
PHGAP2(#2) 1-2;2-2
10 DAS
J
Area [mm²]
K
Perimeter [µm]
L
Circularity [a. u.]
WT (226)
1-1;2-1 (220)
1-2;2-2 (246)
1-1;2-2 (270)
M
N
O
WT (215)
1-1;2-1 (260)
1-1;2-1 #1 (219)
1-1;2-1 #2 (223)
P
Q
R
WT (217)
1-1;2-1 (241)
1-1;2-1 #1 (229)
1-1;2-1 #2 (242)

Figure 1: Phenotypic analysis of different *phgap1 phgap2* mutants

(A) Wild type seedlings and seedlings of different *phgap* mutant allele combinations (*phgap1-1 phgap2-1*, *phgap1-2 phgap2-2*, *phgap1-1 phgap2*-2) 10 days after sowing (DAS). Scale bar 5 mm. (B) Boxplot comparing the width/length ratio of cotyledons from wild type and *phgap* double mutants as indicated in (A). The number (n) of analysed cotyledons from 50 seedlings per genotype is indicated (One-Way-Anova: $F=131.36$, $p<0.0001$, Post Hoc Test: Tukey HSD). Data represent one of two biological replicates with similar results. (C) Cotyledon and first eight leaves (from left to right) of 25-day old wild type and *phgap1-1 phgap2-1* plants. Scale bar: 5 mm. (D-I) Z-Projection of cotyledon pavement cells 10 DAS, stained with propidium iodide (D) wild type, (E) *phgap1-1 phgap2-1*, (F) *phgap1-2 phgap2-2*, (G) *phgap1-1 phgap2-2*, (H) *phgap1-1 phgap2-1* expressing *pGAP1:GFP-gGAP1* (independent lines #1 and #2) and (I) *phgap1-1 phgap2-1* expressing *pGAP2:GFP-gGAP2* (independent lines #1 and #2). Scale bars 50µm. (J-R) Boxplots comparing various pavement cell shape features ((J) Area, (K) Perimeter, (L) Circularity) between wild type and the different *phgap* double mutant allele combinations (shown are the data from one of two biological replicates with similar results), (M-O) *pGAP1:GFP-gGAP1* (#1 and #2) complementation of *phgap1-1 phgap2-1* and (P-R) *pGAP2:GFP-gGAP2* (#1 and #2) complementation of *phgap1-1 phgap2-1* (displayed are the data from one experiment including two independent rescue lines). Number (n) of pavement cells analysed from 5 seedlings per line are indicated (Kruskal-Wallis, Post Hoc: Dunn's-Test, Benjamini-Hochberg-adjusted p-values). Boxplots: + represents the sample mean, different letters indicate significant statistical differences between genotypes.

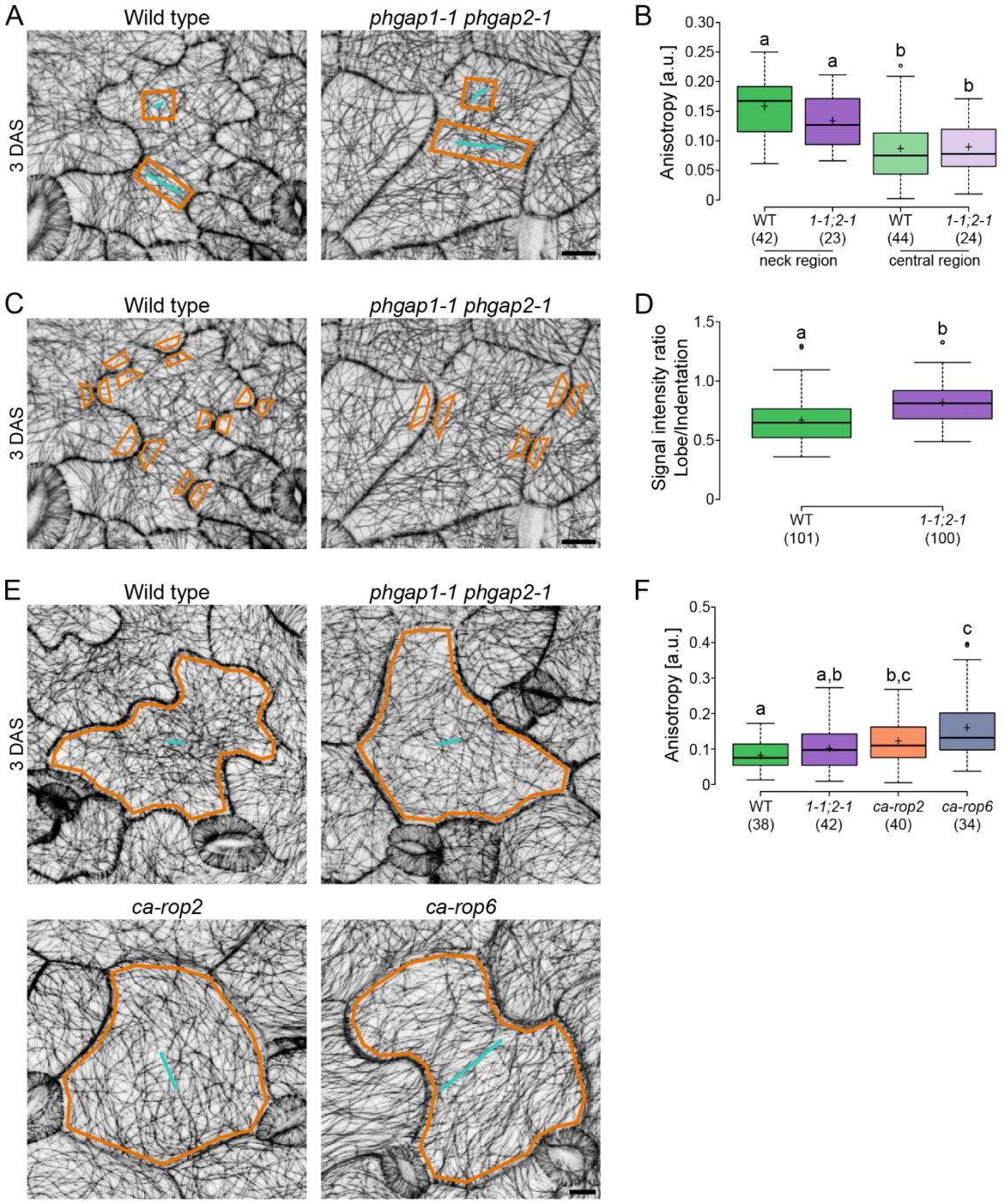

Figure 2: Microtubule organization in developing *phgap1-1 phgap2-1* double mutant pavement cells

(A, C, E) Microtubule organization in pavement cells of seedlings as indicated, expressing microtubule reporter *p35S:GFP-MAP4* (Marc et al., 1998). (A, E) Microtubule anisotropy (turquoise line) in a region of interest (orange selection) in pavement cells three days after sowing (DAS) was analysed using the ImageJ plugin Fibril Tool (Boudaoud et al., 2014). Scale bars 10 µm. (B) Boxplot displaying the microtubule anisotropy in the neck region and the anisotropy in the central region of wild type (WT) and *phgap1-1 phgap2-1* (*1-1;2-1*) pavement cells shown in (A). Regions (number in brackets) from WT (5 seedlings) and *1-1;2-1* (3 seedlings) were analysed (One-Way-Anova: F=17.94, p<0.0001, Post Hoc Test: Tukey HSD). (C) Regions (orange boxes) in lobes and opposing indentation regions of wild type and *phgap1-1 phgap2-1* double mutant seedlings three DAS were selected to compare the mean fluorescent intensity using ImageJ. Scale bar 10 µm. (D) Boxplot comparing the mean signal intensity ratio between lobe and indentation as selected in (C) for WT (5 seedlings) and *1-1;2-1* (3 seedlings). The number of analysed Lobe/Indentation pairs is shown in brackets. (Welch two sample T-test: t=5.99,

p<0.0001). (F) Boxplot illustrating the microtubule anisotropy in pavement cells (number of analysed cells in brackets) in WT (4 seedlings), *1-1;2-1* (4 seedlings), *ca-rop2* (7 seedlings) and ca-rop6 (4 seedlings) shown in (E) (One-Way-Anova: F=8.82, p<0.0001, Post Hoc Test: Tukey HSD). Images are maximum z-projections. The data from a single experiment is shown. Boxplots: + represents the sample mean, different letters indicate significant statistical differences between analysed regions/genotypes.

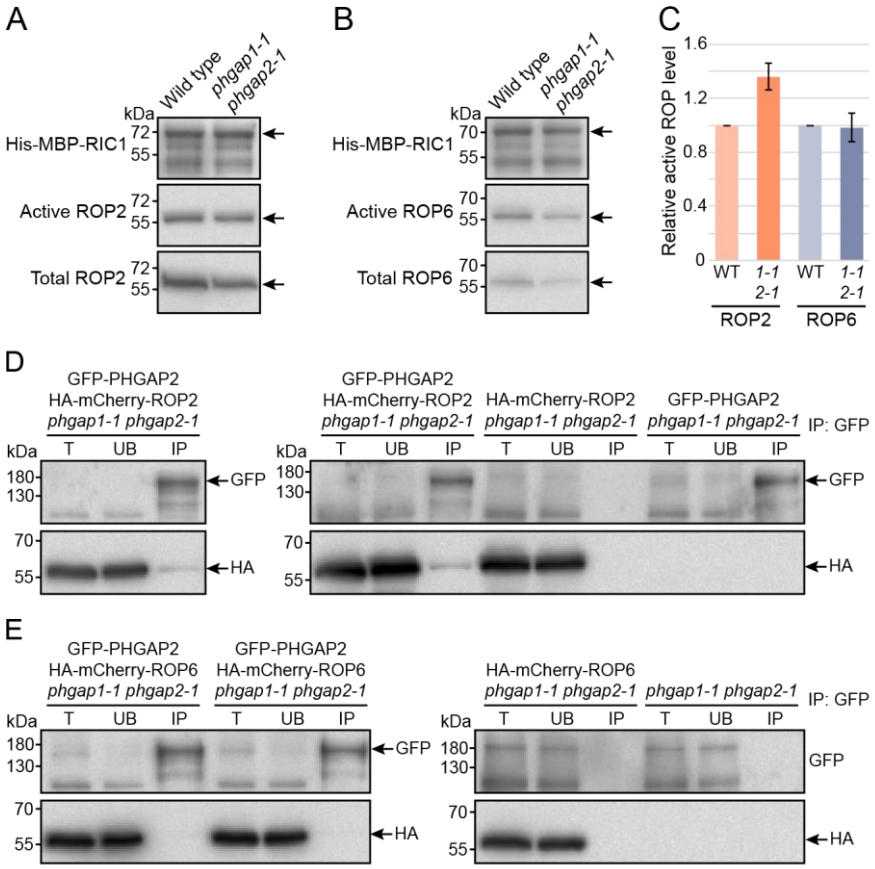

Figure 3: Active ROP2 levels are elevated in *phgap1-1 phgap2-1* and PHGAP2 interacts with ROP2

(A and B) Pull-Down experiments to determine amounts of active ROP2 and active ROP6. His-MBP-RIC1 conjugated beads were used to pull-down (A) active HA-mCherry-ROP2 or (B) active HA-mCherry-ROP6 from total protein extracts prepared from leaves/hypocotyls of wild type and *phgap1-1 phgap2-1* 5-day old seedlings. Arrows mark the His-MBP-RIC1 (69 kDa), the active and the total HA-mCherry-ROP2 (54 kDa) and HA-mCherry-ROP6 (54 kDa) respectively on western blots. (C) Quantification of relative active ROP levels (amount of active ROP divided by the amount of total ROP) in wild type (WT) and *phgap1-1 phgap-2-1* (*1-1; 2-1*) double mutant, shown in (A and B). Relative active ROP level of ROP2 and ROP6 in wild type was set as “1”, respectively. The mean values ± SD from three biological replicates are shown. (D and E) Co-immunoprecipitation (Co-IP) of GFP-PHGAP2 and (D) HA-mCherry-ROP2 and (E) HA-mCherry-ROP6 in the *phgap1-1 phgap2-1* double mutant background. Anti-GFP conjugated agarose beads were used to immunoprecipitate GFP-PHGAP2 (126 kDa) and HA-mCherry-ROP2 and HA-mCherry-ROP6, that were co-expressed in 5-day old seedlings. Seedlings expressing only HA-mCherry-ROP2, HA-mCherry-ROP6 or GFP-PHGAP2 served as negative controls. Displayed is 1/230 of the total (T) amount of protein that was used for Co-IP, 1/346 of unbound protein (UP) that was not immunoprecipitated and ½ of immunoprecipitated protein (IP). Two of three biological replicates are shown in (D) and (E).

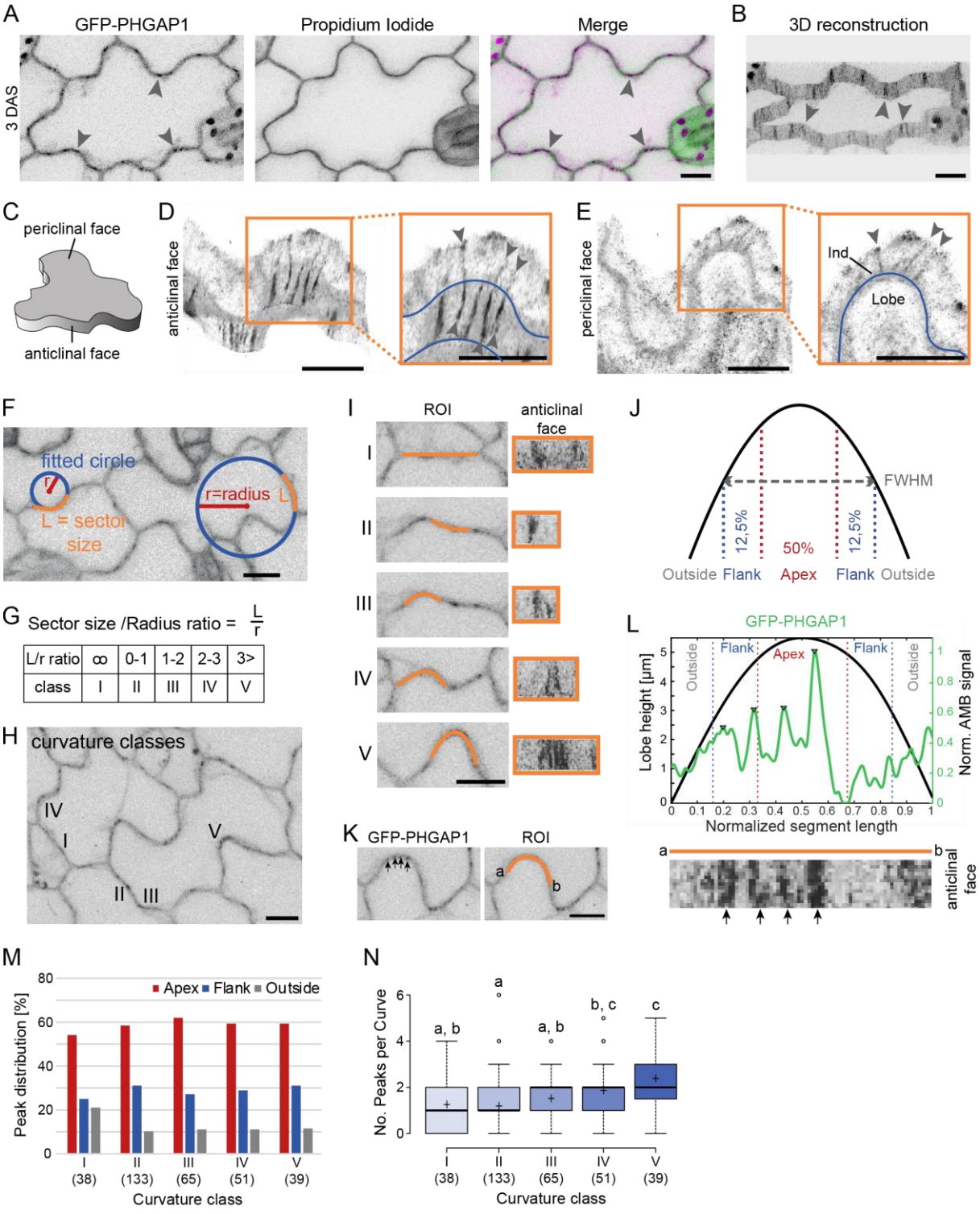

Figure 4: PHGAP1 localization in developing pavement cells

(A) Maximum z-projection (anticlinal face in top view) of GFP-PHGAP1 localization in cotyledon pavement cells three days after sowing (3 DAS). Propidium iodide (10 µg/ml) staining visualized the cell wall. GFP-PHGAP1 localizes along the cell periphery and in dotted accumulations (arrow heads). (B) Three-dimensional (3D) reconstruction of the anticlinal face of the cell in (A). GFP-PHGAP1 accumulations (arrow heads) correspond to dots in (A). (C) Schematics illustrating the periclinal and anticlinal cell face. (D-E) 3D reconstruction of GFP-PHGAP1 localization on (D) anticlinal and (E) periclinal face. Blue lines in (D) mark the upper and lower edge of the anticlinal face, while the blue line in (E) designate the position of the cell wall. GFP-PHGAP1 strip-like accumulations extend from the anticlinal face into the periclinal face (arrow heads) of the indentation (Ind) but not of the lobe. (F)

Drawing illustrating the parameters (sector size, radius, fitted circle) that were assessed for classification of wall curvature degree. Circles were fitted to curvatures of lobe/indentations. More pronounced curvatures show a smaller fitting circle compared to those being at the beginning of their development. (G) Curvatures were classified in different classes I-V (table) according to their sector size/radius ratio (formula). Curvature class I represents straight cell walls, while classes II-V encompass different degrees of bulging. (H) Overview and (I) representative images of the different curvature classes I-V. Depicted are the GFP-PHGAP1 signal in top view (left) and the region of interest (ROI) used to generate the anticlinal face view (right). (J) Draft displaying the different curvature regions that were analysed in the following. The apex is defined as the central 50% at full width half maximum (FWHM) of a curvature. The flank represents the 12,5% on either side of the apex at FWHM. The remaining regions are specified as outside of a curvature. (K) GFP-PHGAP1 accumulations (arrow) along the curvature. a and b delimit ROI used for the generation of the plot profile in (L). (L) Plot profile illustrating correlation between curvature and GFP-PHGAP1 fluorescent signal peaks along the anticlinal face of the ROI in (K). GFP-PHGAP1 peaks (triangles) correspond to arrows in (K) and lower panel in (L). (M) Bar chart of GFP-PHGAP1 peak distribution across curvature classes. GFP-PHGAP1 was predominantly localized in the apex region across all curvature classes. In total, 66 cells of 12 seedlings were analysed 2-3 DAS. Displayed are the data from two experiments. Number of analysed curves for each class are indicated in brackets. (N) Boxplot showing the number of GFP-PHGAP1 peaks per curvature (total number in brackets) in each class. Only peaks in apex and flank region of a curvature were considered. + represents the sample mean, different letters indicate significant statistical differences between curvature classes (Kruskal-Wallis Chi^2=39.552, $p<0.0001$, Post Hoc: Dunn's Test, Bonferroni adjusted p-values). Scale bar in panels A, B, D-F, H, I, K indicates 10 µm.

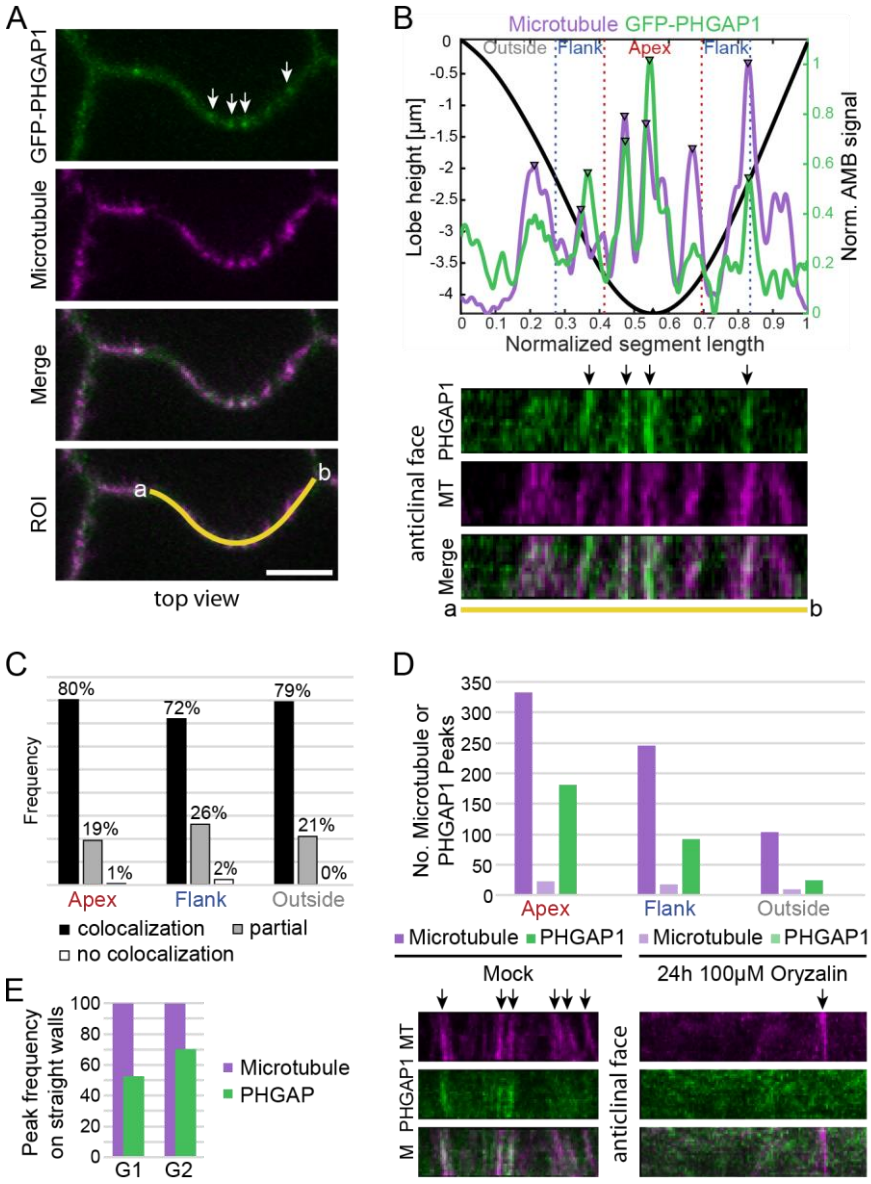

Figure 5: PHGAP localization on anticlinal faces is microtubule dependent

(A) Z-projection of GFP-PHGAP1 accumulation (arrows) and microtubule (RFP-MBD). A region of interest (ROI, a to b) was selected to generate the anticlinal face view and the plot profile in (B). Scale bar 5 µm. (B) Plot profile (top) displaying the GFP-PHGAP1 (arrows) and microtubule (MT) signal peaks along the anticlinal face (a to b) of the ROI selected in (A). (C) Bar chart displaying the frequency of GFP-PHGAP1 peaks that showed co-localization, partial overlap or did not co-localize with microtubule peaks in apex, flank or outside of a curvature. Note that the majority of GFP-PHGAP1 peaks were co-localize with microtubules. In total, 30 anticlinal face segments from 13 cells in 5 seedlings were analysed in a single experiment. (D) PHGAP and microtubule peak frequency in absence and presence of Oryzalin. 3-day old seedlings were transferred on solid medium containing 100 µM Oryzalin or mock for 24 h. Numbers of microtubule and GFP-PHGAP1 peaks were counted in the plot profiles. Lower panels depict representative anticlinal face images of GFP-PHGAP1, microtubules (MT) and merge (M) without and after Oryzalin treatment. Note that a few microtubules persist after Oryzalin treatment, while GFP-PHGAP1 accumulation was abolished completely. In total, 30 anticlinal face segments from 13 cells in 5 seedlings of the Mock control and 47 anticlinal face segments from 17 cells, 5 seedlings on Oryzalin plates were analysed in a single experiment. (E) Frequency of microtubule and GFP-PHGAP1 (G1, 3 seedlings, 19 cell walls) or GFP-PHGAP2 (G2, 2 seedlings, 10 cell walls) signal peaks accumulating on the anticlinal face of straight cell walls. Only 52% and 70% of microtubule bundles associate with either PHGAP1 or PHGAP2, respectively.

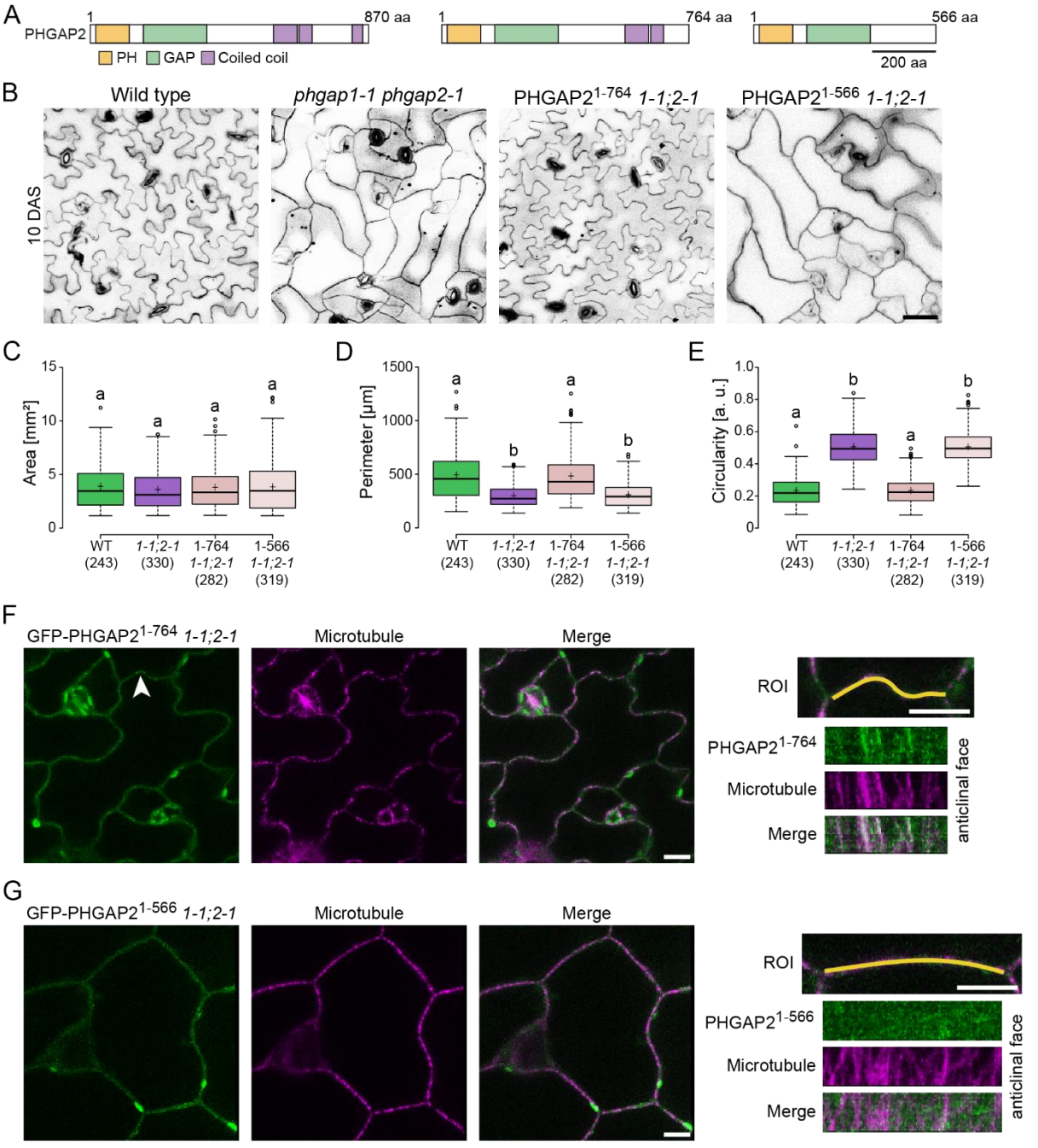

Figure 6: PHGAP2 C-terminal domain is required for pavement cell shape establishment and anticlinal face localization

(A) Protein domain architecture of full length PHGAP2 and of the deletions excluding the coiled coils. In PHGAP2$^{1-764}$, the last coiled coil domain was deleted, while in PHGAP2$^{1-566}$ the entire C-terminal region was missing. (B) Z-Projection of cotyledon pavement cells 10 days after sowing (DAS), stained witch propidium iodide (10 µg/ml) from wild type seedlings, *phgap1-1 phgap2-1*, and *phgap1-1 phgap2-1* expressing either *pPHGAP2:GFP-PHGAP2$^{1-764}$* or *pPHGAP2:GFP-PHGAP2$^{1-566}$*. Scale bar 50 µm. (C-E) Boxplots comparing different pavement cell shape characteristics ((C) Area, (D) Perimeter, (E) Circularity) between wild type (WT), *phgap1-1 phgap2-1* (*1-1;2-1*), GFP-PHGAP2$^{1-764}$; *1-1;2-1* and GFP-PHGAP2$^{1-566}$*; 1-1;2-1* of cotyledons. The number of analysed pavement cells (n) from 4 seedlings per genotype are indicated (Kruskal-Wallis, Post Hoc: Dunn's-Test, Benjamini-Hochberg-adjusted p-values). Displayed are the data from a single experiment. Note that PHGAP2$^{1-566}$ did not complement the pavement cell phenotype of *phgap1-1 phgap2-1* double mutants. (F and G) Anticlinal face top view (left panels) of 3-day old seedlings co-expressing the microtubule marker RFP-MBP and (F) GFP-PHGAP2$^{1-764}$ or (G) GFP-PHGAP2$^{1-566}$ in the *phgap1-1 phgap2-1* (*1-1;2-1*) double mutant background.

Anticlinal face reconstruction (right panels) of a region of interest (ROI) revealed that GFP-PHGAP2$^{1-764}$ is accumulating on the anticlinal face co-localizing with microtubule bundles, while GFP-PHGAP2$^{1-566}$ does not.

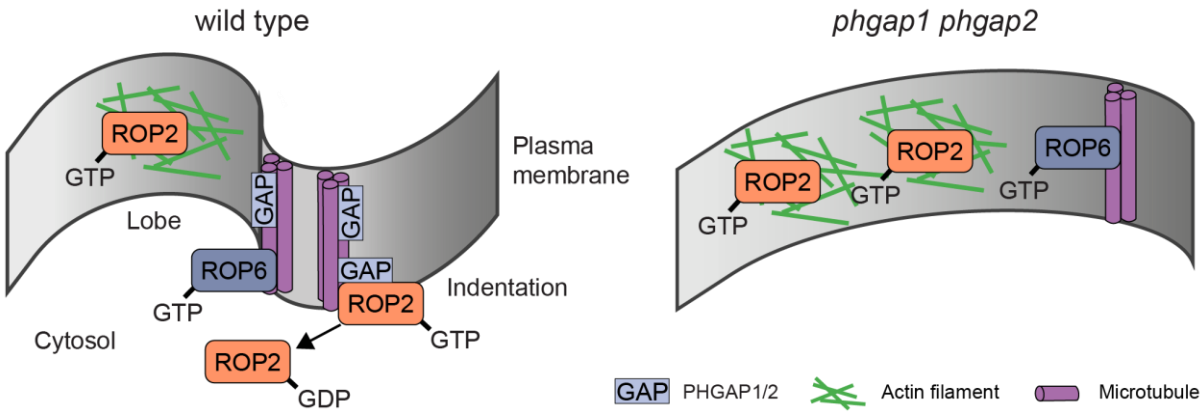

Figure 7: Proposed model of PHGAP function during pavement cell development

PHGAP1 and PHGAP2 are accumulated in a microtubule dependent manner on the anticlinal face of pavement cell indentation regions and co-localize with the microtubule bundles (magenta). PHGAPs interact and inactivate the active GTP-bound form of ROP2 in indentation regions creating a ROP2 activity gradient, with the maximum ROP2 activity in lobes and the minimum in indentations. Inactivation of ROP2 on the indentation side is necessary for proper ROP6-mediated microtubule bundling. Lack of ROP2 inactivation in *phgap1 phgap2* results in increased active ROP2 levels which negatively affect curvature formation as cell polarity is not correctly established, resulting in a loss of cell shape complexity. In conclusion, PHGAP1 and PHGAP2 mediate cell polarity maintenance during pavement cell shape establishment.

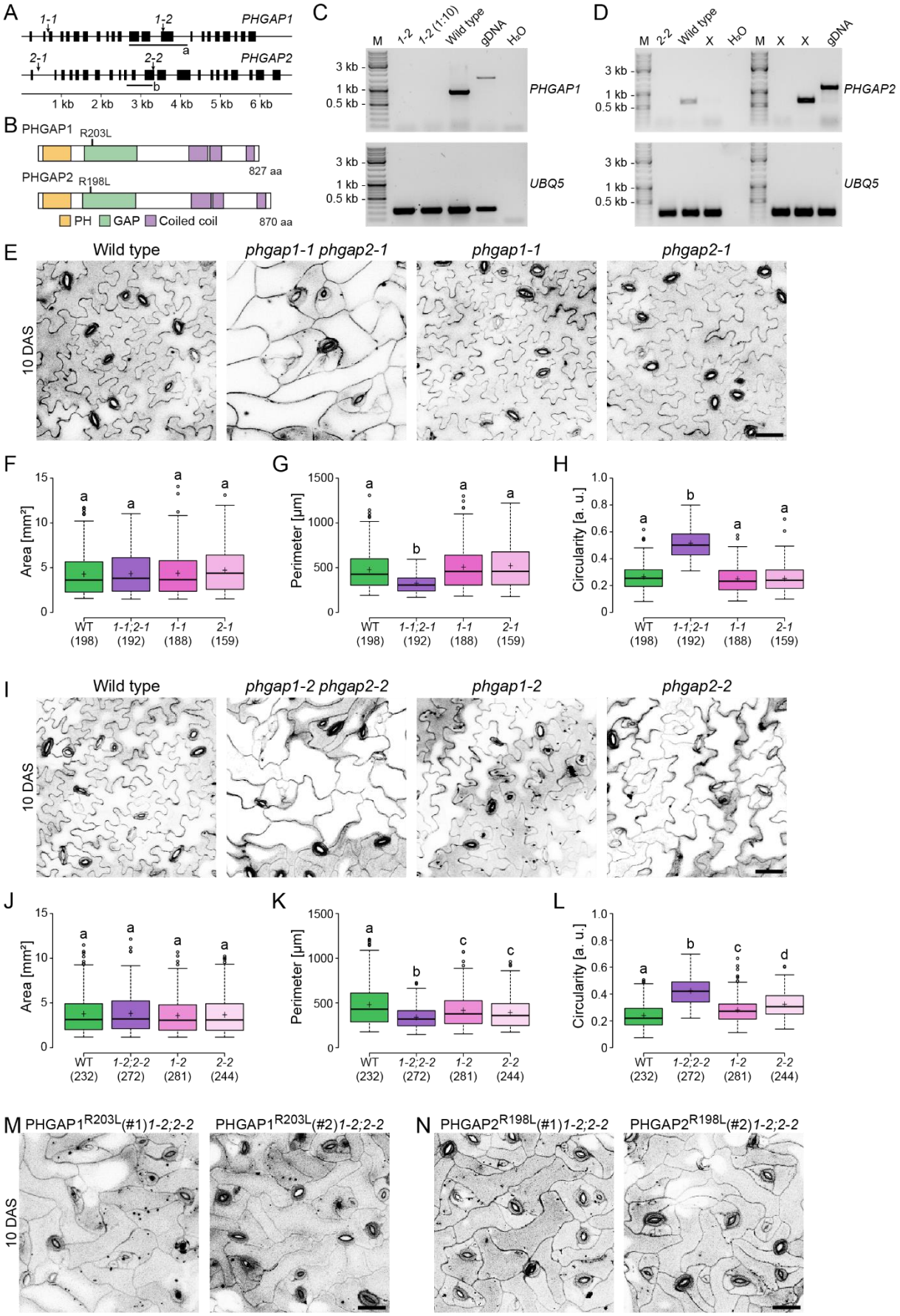
A
1-1
1-2
PHGAP1
a
2-1
2-2
PHGAP2
b
1 kb 2 kb 3 kb 4 kb 5 kb 6 kb
B
PHGAP1
R203L
827 aa
PHGAP2
R198L
PH GAP Coiled coil
870 aa
C
M 1-2 1-2 (1:10) Wild type gDNA H2O
3 kb
1 kb
0.5 kb
PHGAP1
UBQ5
D
M 2-2 Wild type X H2O M X X gDNA
PHGAP2
E
Wild type
phgap1-1 phgap2-1
phgap1-1
phgap2-1
10 DAS
F
Area [mm²]
G
Perimeter [µm]
H
Circularity [a. u.]
WT (198)
1-1;2-1 (192)
1-1 (188)
2-1 (159)
I
Wild type
phgap1-2 phgap2-2
phgap1-2
phgap2-2
J
K
L
WT (232)
1-2;2-2 (272)
1-2 (281)
2-2 (244)
M PHGAP1R203L(#1)1-2;2-2
PHGAP1R203L(#2)1-2;2-2
N PHGAP2R198L(#1)1-2;2-2
PHGAP2R198L(#2)1-2;2-2

Supplemental Figure 1: Gene organization, protein domain architecture and *phgap* mutant phenotypic analysis.

(A) *PHGAP1* (At5g12150) and *PHGAP2* (At5g19390) gene organization (Exons are indicated by bars and the positions of T-DNA insertions are marked by arrows). (B) Protein domain architecture of PHGAP1 and PHGAP2 showing pleckstrin homology (PH)-domain, central conserved GTPase activating protein (GAP) domain and coiled coil domains (predicted by Paircoil, http://paircoil2.csail.mit.edu). (C, D) Gel images of semi-quantitative RT-PCR showing transcript levels of *PHGAP1* and *PHGAP2* in *phgap1-2* and *phgap2-2* mutant alleles and wild type. a and b in (A) mark the position of the primer combinations used for the RT-PCR. Genomic DNA (genDNA) and H_2O were used as positive control and negative control, respectively. *UBIQUITIN* (*UBQ*) *5* fragments served as loading control. (E) Z-Projection of cotyledon pavement cells 10 days after sowing (DAS), stained with propidium iodide (10 µg/ml) from wild type, *phgap1-1 phgap2-1*, *phgap1-1* and *phgap2-1* seedlings. (F-H) Boxplots comparing pavement cell shape characteristics ((F) Area, (G) Perimeter, (H) Circularity) between wild type, *phgap1-1 phgap2-1*, *phgap1-1* and *phgap2-1*. Displayed are the results from one of two biological replicates. Pavement cells (n) from 3-5 seedlings per line were analysed (Kruskal-Wallis, Post Hoc: Dunn's-Test, Benjamini-Hochberg-adjusted p-values). Note that *phgap1-1* and *phgap2-1* single mutants are similar to wild type. (I) Z-Projection of cotyledon pavement cells from wild type, *phgap1-2 phgap2-2*, *phgap1-2* and *phgap2*-2 10 DAS, stained with propidium iodide. (J-L) Boxplots showing (J) Area, (K) Perimeter, (L) Circularity of pavement cells of *phgap1-2 phgap2-2*, *phgap1-2* and *phgap2-2*. Shown are representative results from one of three biological replicates. Five seedlings per line were used for analysis and the total number of cells (n) is indicated (Kruskal-Wallis, Post Hoc: Dunn's-Test, Benjamini-Hochberg-adjusted p-values). Note that *phgap1-2* and *phgap2-2* show a mild pavement cell phenotype. (M and N) Z-Projection of cotyledon pavement cells from (M) *pGAP1:GFP-PHGAP1*^{R203L}; *phgap1-1 phgap2-1* (independent line #1 and #2) or (N) *pGAP2:GFP-PHGAP2*^{R198L}; *phgap1-1 phgap2-1* (independent line #1 and #2) 10 DAS. These mutants with compromised GAP function do not complement the pavement cell phenotype. Scale bar in E, I, M and N indicates 50 µm. Boxplots: + represents the sample mean, different letters indicate significant statistical differences between genotypes.

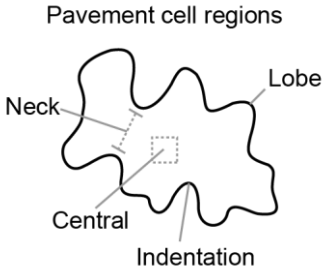

Figure S2: Denotation of pavement cell regions

Schematics illustrating the terminology that was used in this study to describe the different pavement cell regions. The convex side of a curvature is referred to as lobe and the concave side as indentation. The neck is the region between two indentations. The central region is defined as region that does not correspond to lobe, neck and indentation region.

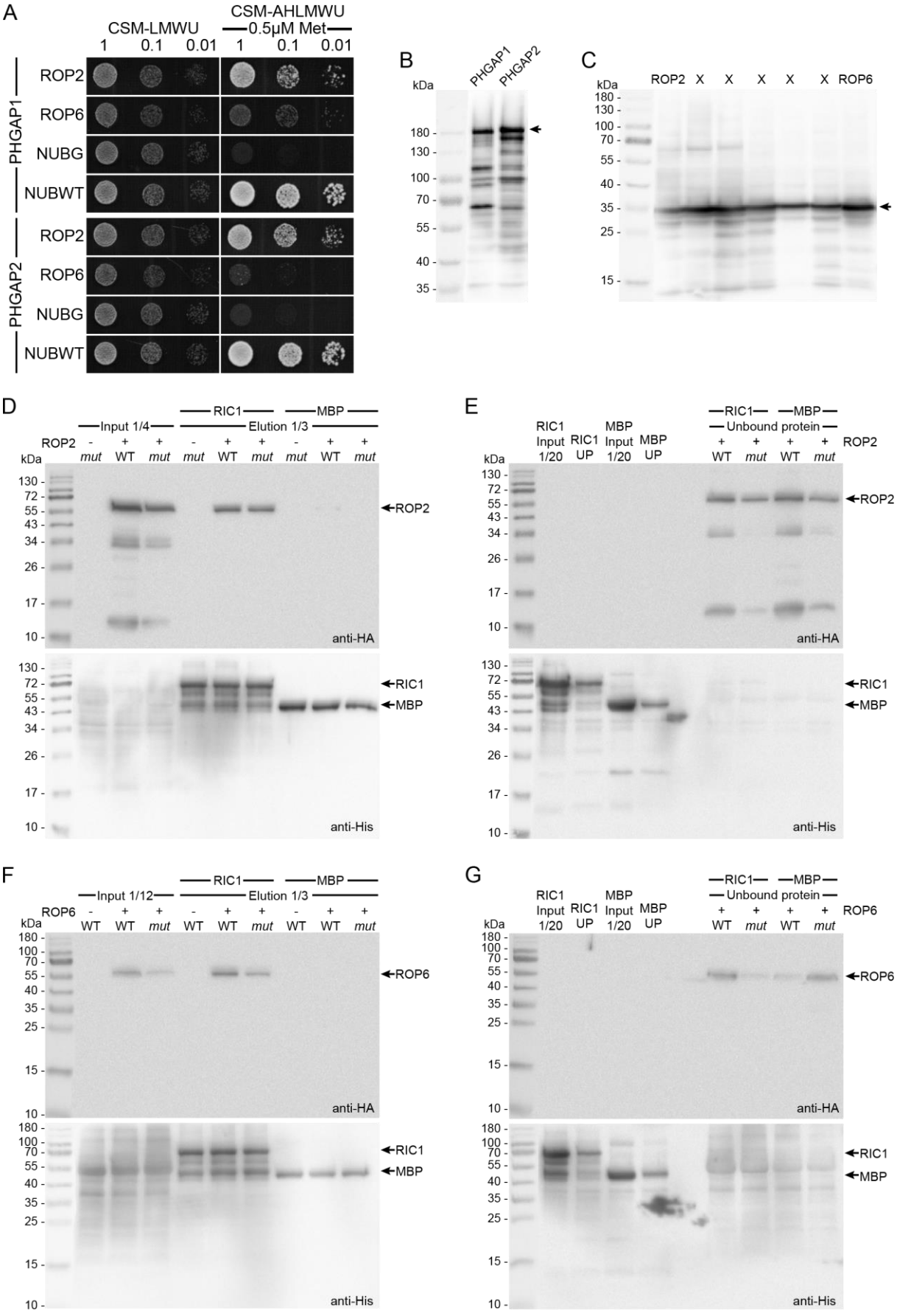
A
CSM-LMWU
CSM-AHLMWU
0.5µM Met
1 0.1 0.01 1 0.1 0.01
PHGAP1
PHGAP2
ROP2
ROP6
NUBG
NUBWT
B
kDa
PHGAP1
PHGAP2
C
kDa
ROP2 X X X X X ROP6
D
Input 1/4
RIC1
MBP
Elution 1/3
ROP2 - + + - + + - + +
mut WT mut mut WT mut mut WT mut
anti-HA
anti-His
ROP2
RIC1
MBP
E
RIC1 Input 1/20
RIC1 UP
MBP Input 1/20
MBP UP
Unbound protein
+ + + + ROP2
WT mut WT mut
F
Input 1/12
ROP6 - + + - + + - + +
WT WT mut WT WT mut WT WT mut
ROP6
G
RIC1 Input 1/20
RIC1 UP
MBP Input 1/20
MBP UP
Unbound protein
+ + + + ROP6
WT mut WT mut

Supplemental Figure 3: PHGAP1 and PHGAP2 predominantly interact with ROP2 and Pull-Down controls.

(A) Yeast mating-based split-ubiquitin system (SUS) assay was performed with PHGAP1 and PHGPA2 as baits (-Cub fusion) and ROP2 and ROP6 as prey proteins (NubG- fusion). Yeast diploids of bait plus prey or bait plus control (NUBG, negative control and NUBWT, positive control) were spotted on CSM-Leu-, Met-, Trp-, Ura- (CSM-LMWU) medium to confirm mating and on CSM-Ade-, His-, Leu-, Met-, Trp-, Ura- (AHLMWU) with 0.5 µM methionine to test for interaction. Colonies correspond to culture concentration 1, 0.1 and 0.001 at OD_{600} from left to right. The assay was performed three times with similar results. (B and C) Western blots confirming the expression of the baits (B) PHGAP1 (152 kDa) and PHGAP2 (157 kDa) (arrow) and the preys (C) ROP2 (30 kDa) and ROP6 (30 kDa) (arrow) used in (A). (D-G) Raw SDS-Page gel images used in Figure 3A and 3B. His-MBP-RIC1 conjugated beads were used to pull-down (D) active ROP2 (Elution) or (F) active ROP6 (Elution) from total protein extracts prepared from leaves/hypocotyls of wild type (WT) and *phgap1-1 phgap2-1* (*mut*) 5-day old seedlings. (F) WT and (D) *mut* extracts were used as negative controls. Additionally, the pull-down experiment was also performed with His-MBP-conjugated beads to exclude unspecific binding of HA-mCherry-ROPs to His-MBP. Input represents the amount of protein extract that was incubated with the beads, unbound protein (UP) shows the proteins that were not attached to the beads, while elution displays the protein amount that was bound to the beads (following number displays fraction of total amount that was loaded on the gel). (E and G) Shown are the Input and UP amount after incubation of MBP-Beads with His-MBP and His-MBP-RIC1, respectively. In addition, the UP amount, representing inactive ROPs, after incubation of extracts from (E) HA-mCherry-ROP2 or (G) HA-mCherry-ROP6 with His-MBP/-RIC1-conjugated Beads, is displayed. Arrows mark the position of His-MBP (47 kDa), His-MBP-RIC1 (69 kDa), ROP2 (54 kDa) and ROP6 (54 kDa) protein on the gels, after separation by SDS-Page and western blot.

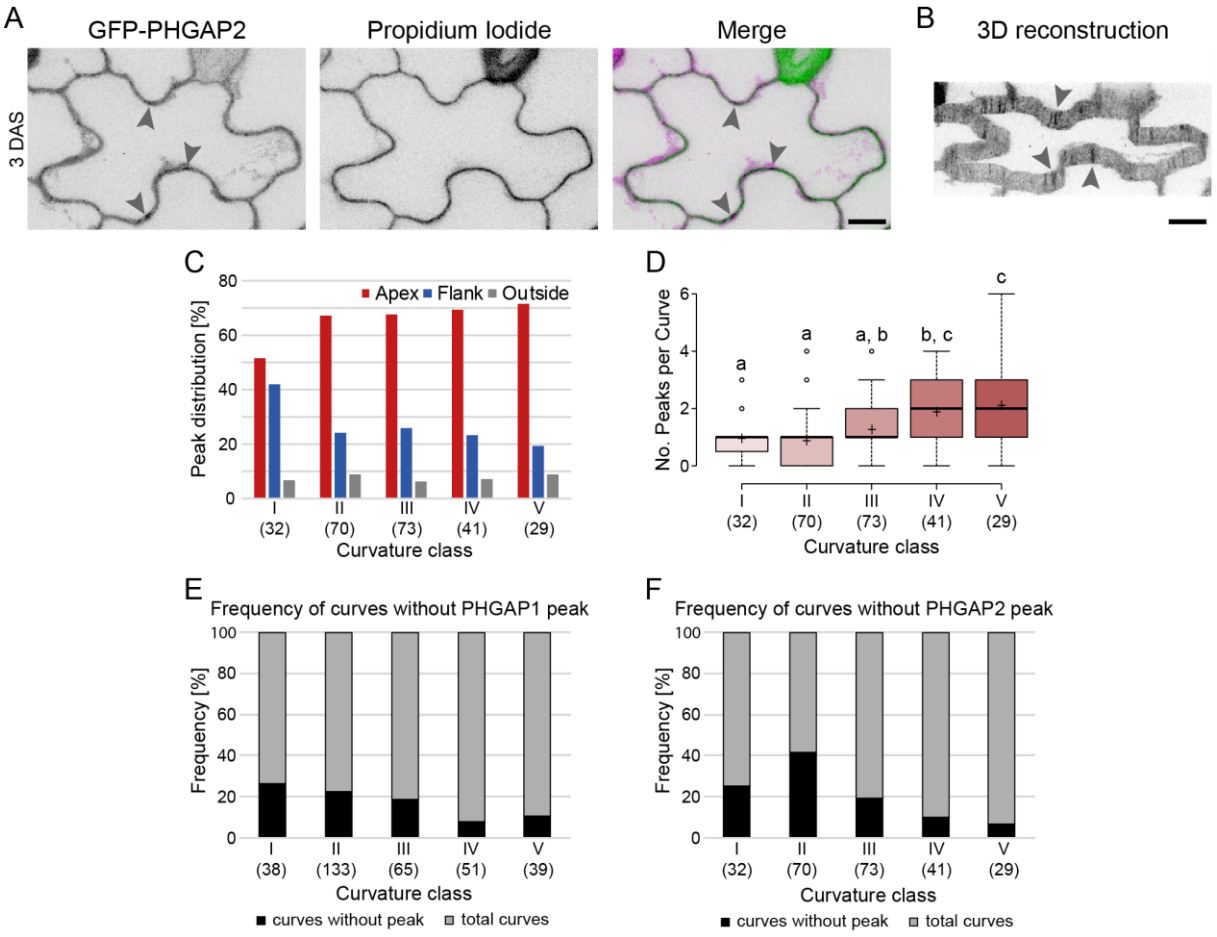

Supplemental Figure 4: Localization pattern of PHGAPs in developing pavement cells

(A) Maximum z-projection (anticlinal face in top view) of GFP-PHGAP2 localization in cotyledon pavement cells three days after sowing (DAS). Propidium iodide (10 µg/ml) staining visualized the cell wall. GFP-PHGAP2 localizes along the cell periphery and in dotted accumulations (arrow heads). (B) Three-dimensional (3D) reconstruction of the anticlinal face of the cell in (A). GFP-PHGAP2 accumulations along the anticlinal face (arrow heads) correspond to dots in (A). Scale bar in A and B 10 µm. (C) Bar chart of GFP-PHGAP2 peak distribution across curvature classes. GFP-PHGAP2 is predominantly localized in the apex region across all curvature classes. In total, 55 cells from 11 seedlings were analysed 2-3 DAS. The number of analysed curves for each class is indicted in brackets. Displayed are the data from two experiments. (D) Boxplot showing the number of GFP-PHGAP2 peaks per curvature (total number in brackets) in each class. Only peaks in apex and flank region of a curvature were considered. + represents the sample mean, the different letters indicate statistical significant differences between curvature classes (Kruskal-Wallis Chi^2=39.069, p<0.0001, Post Hoc: Dunn's Test, Bonferroni adjusted p-values). (E and F) Displayed is the frequency of curves that show no GFP-PHGAP1 peak (E) or no GFP-PHGAP2 peak (F) in comparison to total curves, in different curvature classes. In total, 66 cells from 12 seedlings were analysed for PHGAP1 and 55 cells from 11 seedlings were analysed for PHGAP2 2-3 DAS. Number of analysed curves for each stage are indicated in brackets.

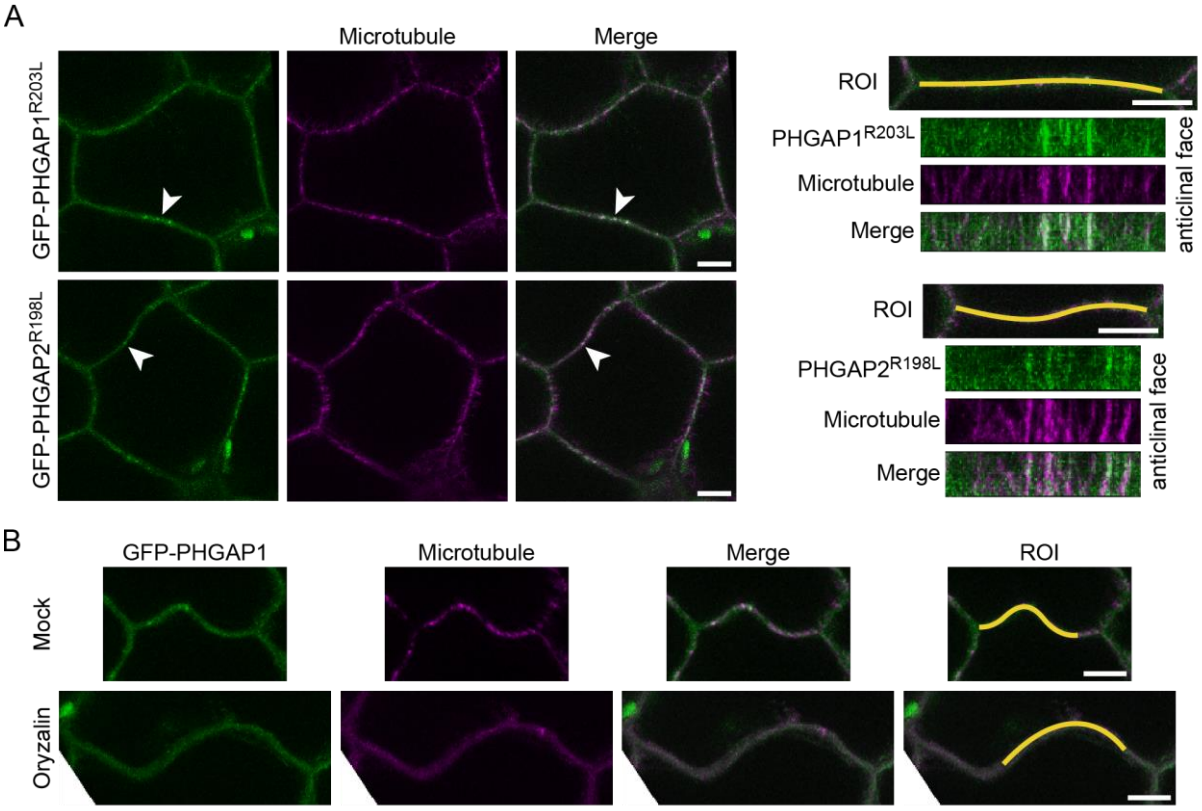

Supplemental Figure 5: A functional GAP domain is not required for anticlinal face localization

(A) Z-projection of cotyledon pavement cells co-expressing GFP-PHGAP1^{R303L} or GFP-PHGAP2^{R198L} and the microtubule reporter RFP-MBD in top view (left panels) three days after sowing (DAS). The reconstruction of the anticlinal face is also shown (right panels). Arrows mark PHGAP accumulation on the anticlinal face and the segment that was used for anticlinal face reconstruction. Point mutation in the GAP domain abolishing its catalytic function, has no effect on PHGAP/microtubule co-localization on the anticlinal face. Scale bar 10 µm. (B) Anticlinal face top view (z-projection) of GFP-PHGAP1 and microtubule (RFP-MBD) signal, after 3-day old seedlings were transferred on solid medium containing 100 µM Oryzalin or mock and incubated for 24 h. For the reconstruction of the anticlinal view a region of interest (ROI) was selected (Figure 5D). Scale bar 5 µm.

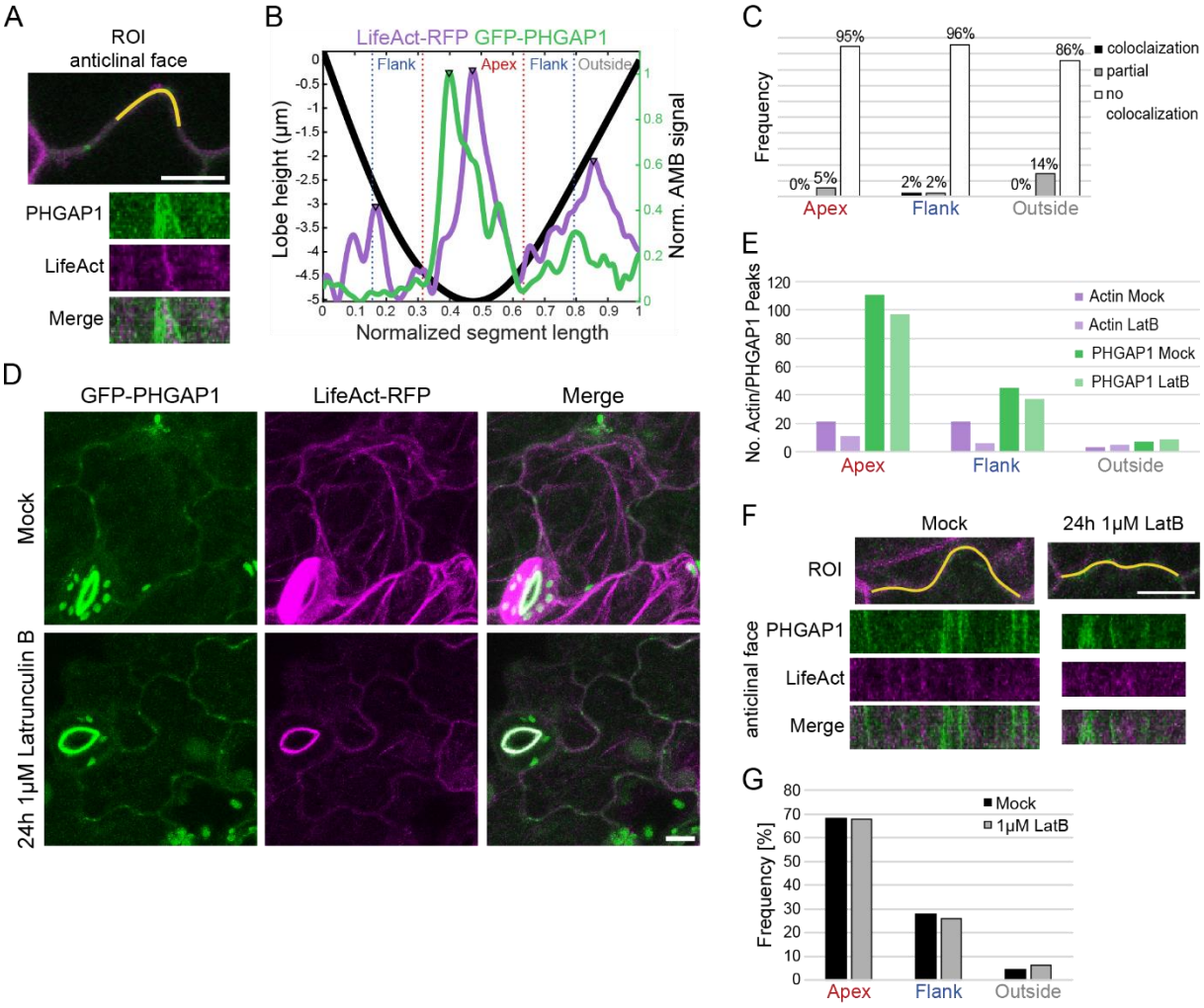

Supplemental Figure 6: PHGAPs do not co-localize with actin filament on anticlinal face and PHGAP localization is actin filament independent

(A) Anticlinal face reconstruction of a region of interest (ROI) of pavement cells from seedlings co-expressing GFP-PHGAP1 and the actin reporter LifeAct-RFP. Scale bar 10 µm. (B) Plot profile displaying GFP-PHGAP1 (green) and LifeAct-RFP (magenta) signal peaks (triangle) along the anticlinal face segment in (A). (C) Bar chart showing the frequency of GFP-PHGAP1 peaks that showed co-localization, partial overlap or no co-localization with actin filament peaks in apex, flank or outside of a curvature. Note that the majority of GFP-PHGAP1 peaks are not co-localizing with actin filaments. In total, 131 curvatures from 11 cells in 5 seedlings of one experiment were analysed. (D) Maximum z-projection of z-stacks covering the distance from the beginning of the external periclinal wall to the end of the anticlinal face of 3-day old seedlings co-expressing GFP-PHGAP1 and LifeAct-RFP after mock or 1 µm Latrunculin B (LatB) treatment for 24 h. Most of the actin filaments were depolymerized after treatment with LatB. Scale bar 10 µm. (E) PHGAP1 and actin filament peak frequency in absence and presence of LatB. Numbers of actin filaments and GFP-PHGAP1 peaks were counted in plot profiles. Only a minor portion of actin filaments are present on the anticlinal face which are even more reduced after LatB treatment, while the amount of GFP-PHGAP1 peaks is only slightly affected. In total, 131 curvatures from 11 cells in 5 seedlings of the mock control and 133 curvatures from 13 cells in 5 seedlings on LatB plates of one experiment were analysed. (F) Anticlinal face reconstructions of a pavement cell segment (ROI) of seedlings without and after LatB treatment for 24 h in (E). As already indicated by the bar chart in (F), GFP-PHGAP1 accumulation on the anticlinal face is only minimally affected after LatB treatment. (G) Frequency of GFP-PHGAP1 signal accumulation in apex, flank and outside of a curvature along the anticlinal face after mock or LatB treatment analysis reveal no difference.

8. Material and Methods

This section includes the material and methods used in the experiments performed in section 7.1 and in 7.2 (Manuscript).

Plant growth

Seeds were surface sterilized with 6% (v/v) sodium hypochlorite (Roth, Cat. 9062.3), placed on solid growth medium (½ Murashige and Skoog (MS), Duchefa-Biochemie, M0221.0005, 0.1% MES (Duchefa-Biochemie, M1503.0100), 1 % (w/v) agar (Serva, 11396.03), pH 5.7) and stratified at 4°C for 1-2 days in darkness. Afterwards, plants were grown in long day growth chambers (cycling 16 h light / 8 h dark) at 22 °C. For further propagation of plant lines, two week old seedlings were transferred to soil.

Plant and bacterial material

In this study *Arabidopsis thaliana* plants of the ecotype Columbia (Col-0, wild type) were used. For mutant analysis of *PHGAP* genes, T-DNA insertion lines *phgap1-1* (WiscDsLoxHs135_04D) and *phgap1-2* (WiscDsLoxHs357_G01) were obtained from the Arabidopsis biological resource centre (ABRC, Ohio, US) and *phgap2-1* (SALK_083351) and *phgap2-2* (SALK_131823) from the Nottingham Arabidopsis stock centre (NASC, Nottingham, UK) (Alonso et al., 2003). *phgap* double mutants were generated by crossing of the single mutants. The *trm6 trm7 trm8* triple mutant was provided by Dr. Martine Pastuglia (Schaefer et al., 2017). Transgenic lines, used for pavement cell shape complementation and for cell division analyses, were created by *Agrobacterium tumefaciens* (*A. tumefaciens*)-mediated transformation (Clough and Bent, 1998) of strain GV3101 carrying respective plasmids, into *phgap1-1 phgap2-1*, *phgap1-1/+ phagp2-1/+* or *trm6 trm7 trm8*. Lines used for Co-IP were obtained by transformation of *pEG104:HA-mCherry-ROP2* or *pEG104:HA-mCherry-ROP6* in *pGAP2:GFP-gGAP2 phgap1-1 phgap2-1* lines. Transgenic lines for pull-down experiments were generated by crossing the “Co-IP” lines with Col-0 and genotyping of the F2 generation to select plants expressing *pEG104:HA-mCherry-ROP2* and *pEG104:HA-mCherry-ROP6* in Col-0 and *phgap1-1 phgap2-1* background. For analysis of microtubule organization in Col-0, *phgap1-1 phgap2-1*, *ca-rop2* and *ca-rop6*, lines were crossed with the previously described microtubule reporter line *p35S:GFP-MAP4* (Marc et al., 1998). Co-localization studies and Oryzalin treatments were performed using the microtubule reporter line *pUBN:RFP-MBD* (Lipka et al., 2014) introduced in the *GFP-PHGAP1* or *GFP-PHGAP2 phgap1-1 phgap2-1* rescue line. For imaging of actin organization and treatments with Latrunculin B, the actin reporter *Life-Act-RFP* (Cvrčková and Oulehlová, 2017) was crossed with *GFP-PHGAP1* or *GFP-PHGAP2 phgap1-1 phgap2-1* rescue lines. For cloning, heat shock competent

Escherichia coli (*E. coli*) strains DH5α (Invitrogen) or TOP10 (Invitrogen) were used for plasmid amplification.

cDNA generation, PCR product amplification, ligation and semi quantitative RT-PCR

RNA was isolated from 100 mg flower material with the RNeasy Plant Mini Kit (Qiagen, Cat. 74904) as described in the manual. cDNA was synthesized from RNA with oligo $d(T)_{20}$ primer (Thermo Fisher Scientific, Cat. 18418020) using the Superscript Reverse Transcriptase II (Invitrogen, Cat. 18064022) as instructed by the company. Phusion DNA Polymerase (New England Biolabs, M0530L) was used to amplify PCR products for cloning. Ligation was performed using Quick Ligation Kit (New England Biolabs, M2200L). For the RT-PCR, PHGAP1_EcoRI_F x PHGAP1_1506_R were used to test for the presence of the *PHGAP1* transcript in *phgap1-2*, and PHGAP2_01F x PHGAP2_01R were used for amplification of *PHGAP2* transcript in *phagp2-2* (Stöckle, 2015). Ubiquitin coding sequence was amplified with NUBQ x CUBQ as RT-PCR control (Müller et al., 2006).

Generation of fluorescent fusion proteins

PHGAP fusions:

pPHGAP1:GFP-gPHGAP1 (Theresa Lauster): PHGAP1 promoter sequence was amplified from Col-0 DNA with proPHGAP1_3.5kb_F x proPHGAP1_BglII_GFP_R. The primer pair proPHGAP_BglII_GFP_F x linker_GFP_R was used to amplify and create the GFP linker fragment from pMDC99:pGAP2:GFP-gGAP2$^{1-566}$, that served as template. Genomic PHGAP1 was amplified with PHGAP1_ATG_F x PHGAP1_3'UTR_2R_NotI from Col-0 DNA. Promoter pPHGAP1, GFP-linker and genomic gPHGAP1 fragments were first subcloned into pENTR3C and subsequently combined via restriction digest and appropriate fragment ligation in the pENTR3C backbone. Finally, pENTR3C:pPHGAP1:GFP-gPHGAP1 was recombined with the pMDC99 destination vector (Curtis and Grossniklaus, 2003) in a Gateway LR reaction (LR clonase, Invitrogen, 11791-020).

pPHGAP1:GFP-gPHGAP1^{R203L} (Theresa Lauster): pENTR3C:pPHGAP1:GFP-gPHGAP1 and pENTR3C:cGAP1^{R203L} (Stöckle et al., 2016) were digested with StuI/BamHI and appropriate fragments were ligated to create pENTR3C:pPHGAP1:GFP-gPHGAP1^{R203L} which was recombined with the destination vector pMDC99 using LR clonase.

pUBN:GFP-cGAP1$^{1-459}$ (Jonathan Ryan, Steffi Zimmermann): PHGAP1 cDNA, generated from flowers via reverse transcription, was amplified using PHGAP1_ATG_F and PHGAP1_Stop_R and ligated into pGEM-T-easy vector (Promega, A1360). pGEM:cPHGAP1 and pENTR3C were digested with KpnI/NotI and appropriate fragments ligated to generate pENTR3C:cPHGAP1. A digest with EcoRV and re-ligation was used to delete the C-terminal

region and create pENTR3C:cPHGAP$^{1-459}$. pENTR3C:cPHGAP1$^{1-459}$ was recombined with the final destination vector pUBN:GFP-Dest. (Grefen et al., 2010) via LR clonase.

pPHGAP2:GFP-gPHGAP2 (Stöckle et al., 2016): gPHGAP2 fragments were generated with linker-PHGAP2_F x PHGAP2_01R, PHGAP2_3438_F x PHGAP2_STOP_R and deltaPHGAP2-400F x PHGAP2_3'UTR from BAC F7K24, pPHGAP2 promoter was amplified from Col-0 DNA with primers proPHGAP2_F x proPHGAP2-GFP_R and GFP-linker fragment from pUBN:GFP-Dest. (Grefen et al., 2010) with proPHGAP2_GFP_F x linker_GFP_R. All fragments were subcloned into pENTR3C individually, before they were combined in one pENTR3C backbone. Subsequently, an LR reaction was used to recombine pENTR3C:pPHGAP2:GFP-gPHGAP2 with the destination vector pMDC99.

pPHGAP2:GFP-gPHGAP2^{R198L} (Theresa Lauster): pENTR3C:pPHGAP2:GFP-gPHGAP2 and pENTR3C:cGAP2^{R198L} (Stöckle et al., 2016) were digested with SapI/Kpn2I and appropriate fragments were ligated. pENTR3C:pPHGAP2:GFP-gPHGAP2^{R198L} was recombined with the destination vector pMDC99 using LR clonase.

pPHGAP2:GFP-gPHGAP2$^{1-764}$ (Theresa Lauster): PCR fragment was amplified with PHGAP2_3438_F x PHGAP2_764aa_stop_R from pENTR3C:pPHGAP2:GFP-gPHGAP2. Afterwards, both the PCR fragment and the plasmid were digested with XhoI/XbaI and appropriate fragments were ligated. The resulting vector pENTR3C:pPHGAP2:GFP-gPHGAP2$^{1-764}$ was then used in a final LR reaction with the destination vector pMDC99.

pPHGAP2:GFP-gPHGAP2$^{1-566}$ (Theresa Lauster): PCR fragment was amplified with PHGAP2_01F x PHGAP2_566aa_stop_R from pENTR3C:pPHGAP2:GFP-gPHGAP2, both the PCR fragment and the plasmid were digested with XhoI/XbaI and appropriate fragments ligated. Further, the resulting vector pENTR3C:pPHGAP2:GFP-gPHGAP2$^{1-566}$ was used in an LR reaction with the destination vector pMDC99.

pUBN:GFP-cGAP2^{S447A} (Dorothee Stöckle, Steffi Zimmermann): cPHGAP2 was amplified from cDNA generated from flowers using PHGAP2_ATG_F x PHGAP2_Stop_R and cloned into pGEM-T-easy vector (Promega, A1360). pGEM:cPHGAP2 and pENTR3C were digested with BamHI/NotI and appropriate fragments were ligated. pENTR3C:PHGAP2 served as template for site directed mutagenesis PCR with the primer combination At5g19390 S447A for x At5g19390 S447A rev to generate pENTR3C:cGAP2^{S447A}. Finally, an LR reaction was performed to introduce cGAP2^{S447A} in the final destination vector pUBN:GFP-Dest. (Grefen et al., 2010).

pUBN:GFP-cGAP2^{S447E} (Dorothee Stöckle, Steffi Zimmermann): pENTR3C:cPHGAP2 was used in a site directed mutagenesis reaction with the oligonucleotides At5g19390 S447E for x

At5g19390 S447E rev to create pENTR3C:cGAP2^{S447E}. cGAP2^{S447E} was recombined with pUBN:GFP-Dest. (Grefen et al., 2010) in a final LR reaction.

ROP fusions:

pEG104:HA-mCherry-ROP2 (Theresa Lauster, Dorothee Stöckle, Steffi Zimmermann): pUNI51:ROP2 (ABRC, U09414) was used for a cre-lox recombination with pNIGEL17 (Niko Geldner). ROP2 was amplified from pNIGEL17:cROP2 with ROP2-ATG_F x ROP2_STOP_R and cloned via KpnI/EcoRV in pENTR3C. pENTR3C:cROP2 and pEG104:HA-mCherry (Gutierrez et al., 2009) were recombined in an LR reaction to generate pEG104:HA-mCherry-ROP2.

pEG104:HA-mCherry-ROP6 (Theresa Lauster, Steffi Zimmermann): pENTR223:ROP6 (ABRC, G69209) was recombined in an LR reaction with pGBKT7 vector (TaKaRa, Cat. 630443). pDGBK:cROP6 was recombined in an BP reaction (BP clonase, Invitrogen 11789-020) with pDONR207. pDONR207:cROP6 and pEG104:HA-mCherry (Gutierrez et al., 2009) were recombined in an final LR reaction to create pEG104:HA-mCherry-ROP6.

pEG104:HA-mCherry-CA-ROP2 (Theresa Lauster, Jonathan Ryan, Dorothee Stöckle): ROP2 was amplified with attB3ROP2F x attB2ROP2R from pUNI51:ROP2 (ABRC, U09414) adding flanking att sites for recombination using BP reaction into pDONR221-P3P2 (Invitrogen, part of MultiSite Gateway Pro Plus Kit Cat. 12537100). Site directed mutagenesis of pDONR221-P3P2:cROP2 with ROP2 G14V_F x ROP2 G14V_R was performed to introduce a point mutation in ROP2 sequence (resulting in glycine (G) to valine (V) substitution at amino acid position 14) rendering ROP2 constitutively active. Primers ROP2_KpnI_F x ROP2_EcoRV_R were used to amplify CA-ROP2 from pDONR221-P3P2. The PCR fragment and pENTR3C were restricted with KpnI/EcoRV and appropriate fragments were ligated, resulting in pENTR3C:CA-ROP2. pENTR3C:cROP2-CA was then recombined in an LR reaction with pEG104:HA-mCherry to create pEG104:HA-mCherry-CA-ROP2.

pEG104:HA-mCherry-CA-ROP6 (Natalie Krieger, Theresa Lauster): CA-ROP6 was amplified with BamHI-ROP6_F and XhoI_ROP6_R from pGBT9:CA-ROP6 (provided by Shaul Yalowsky) and cloned into pGEM-T-easy vector (Promega, A1360). pGEM:CA-ROP6 and pENTR2B were digested with BamHI/XhoI and appropriate fragments were ligated. pENTR2B:CA-ROP6 together with pEG104:HA-mCherry (Gutierrez et al., 2009) were recombined in an LR reaction to generate pEG104:HA-mCherry-CA-ROP6.

Imaging and image processing

Imaging was performed at constant room temperature (22°C). A Leica TCS-SP8 equipped with resonant scanner, Argon/Krypton mixed gas laser or He/Ne laser, hybrid detectors (HyD) and standard PMT detectors, objective 20x (NA=0.75) or 63x (NA=1.20) water immersion objective was used for imaging. For excitation of GFP and Alexa 488 the 488 nm laser line was used and fluorescence signal was detected between 493-547 nm (GFP) and 493-550 nm (Alexa 488). RFP, mCherry, Cy3, FM4-64, and propidium iodide were excited with 561 nm solid state laser and detection was accomplished with detection windows 576-939 nm, 566-642 nm, 574-633 nm, 570-627 nm and 577-632 nm, respectively.

Z-projection of image stacks were generated using Fiji (ImageJ, https://imagej.net/Fiji). Three-dimensional (3D) reconstructions of image stacks were generated with Leica TCS-SP8 software. Linear colour adjustments were applied using Adobe Photoshop CS5 v12.0 and colour merges were conducted using Fiji. Adobe Illustrator CS5 v15.0 was used to assemble the figures.

Cotyledon shape analysis

For cotyledon shape analysis, seedlings were grown on solid medium for 10 days. For imaging, cotyledons were prepared flat on the surface of solid medium, by gently pushing the hypocotyl in the agar using tweezers. Plates were scanned at 600 dpi. Only cotyledons that were lying plain were measured. In total, cotyledons from 50 seedlings were analysed. Dead seedlings were excluded.

For the analysis of the cotyledon shape (area, length, width), I developed and used the following MATLAB scripts.

Script for image segmentation:

```
function binarypicture (foldername,filename,format,firstfile,lastfile)
mkdir(foldername)    %generates new folder
cd(foldername)       %changes to new folder
text=('seg_');       %filename attention for segmented images
for i=firstfile:lastfile
    name=strcat(filename,int2str(i),format);
    F=imread(name);
    F=imadjust(F,[0 0.55],[0 0.99]);figure;imshow(F); %changes brightness
and contrast
    Z=size(F);
    z=Z(1); %number or rows
    s=Z(2); %number of columns
    for n=1:z
        for m=1:s
            if F(n,m,3)>150
                F(n,m,1)=0;F(n,m,2)=0;F(n,m,3)=0;
            else F(n,m,3)<=150;
                F(n,m,1)=255;F(n,m,2)=255;F(n,m,3)=255;
            end
```

```
        end
        n=n+1;
    end
    F=rgb2gray(F); %converts RGB in grayscale
    F=F>2; %converts grayscale in binary
    C=bwmorph(F,'clean',inf);
    D=bwmorph(C,'bridge');
    E=bwmorph(D,'close');
    G=bwareaopen(E,30);
    name2=strcat(text,name);
    imwrite(G,name2,'TIF')
    figure; imshow(G);
end
end
```

Script for cotyledon shape analysis:

```
function coty_shape_analysis(filename,format,pixelmm,Excelname)
    Excel=strcat(Excelname,'.xlsx');
    name=strcat(filename,format);
    namenumber=strcat(filename,'_num_',format);
    F=imread(name); figure; imshow(F);
    stats = regionprops(F,'Area');
    stats2 = regionprops(F,'MajorAxisLength');
    stats3 = regionprops(F,'MinorAxisLength');
    stats4 = regionprops(F,'Centroid');
    stats5 = regionprops(F,'Orientation');
    B=bwboundaries(F,'noholes'); %extracts all areas without holes
     for i=1:length(B)
        area = stats(i).Area;  %area of the cotyledon i is measured
        if area>500  %if the cotyledon area is bigger than 500 px the loop
continues if not it starts from the beginning with the next cotyledon
            length2=stats2(i).MajorAxisLength;
            width=stats3(i).MinorAxisLength;
            c=stats4(i).Centroid;
            o=stats5(i).Orientation;
            A(i+1,1)=i; %Matrix column 1, row  i, cotyledon number
            A(i+1,2)=area*(pixelmm^2); %Matrix column 2, row i, area
            A(i+1,3)=length2*pixelmm;
            A(i+1,4)=width*pixelmm;
            A(i+1,5)=(width*pixelmm)/(length2*pixelmm);
            cent = cat(1,stats4(i).Centroid); %determines the coordinates
of the ellipse centre
            metric_string = sprintf('%0.0f',i); %converts results for text
(%2.2 shows number of decimal place)
            T=text(cent(:,1),cent(:,2),metric_string,'Color','r',...
            'FontSize',10,'FontWeight','bold'); %writes the cotyledon
number in the cotyledon in the image
            theta = linspace(0,2*pi); %next 7 code lines to display the
ellipse in the image from the mathworks forum:
https://de.mathworks.com/matlabcentral/answers/495720-how-to-fit-an-
ellipse-to-an-image-in-matlab
            col = (length2/2)*cos(theta);
            row = (width/2)*sin(theta);
            P = makehgtform('translate',[stats4(i).Centroid,
0],'zrotate',deg2rad(-1*stats5(i).Orientation));
            D = P*[col;row;zeros(1,numel(row));ones(1,numel(row))];
            hold on
            plot(D(1,:),D(2,:),'r','LineWidth',1)
            saveas(T,namenumber,'tif') %Image with cotyledon number and
ellipse will be saved
```

```
        else area<=500;
            i=i+1;
        end
    end
    A(1,:)=0;
    A(~any(A,2),:)=[]; %deletes all rows with 0 in matrix A
    titels =["No.","area [mm²]","length [mm]","width
[mm]","width/length"];
    xlswrite(Excel,titels,1,'A1');
    xlswrite(Excel,A,1,'A2'); %matrix is saved in Excel file
end
```

Pavement cell shape analysis

To analyse pavement cell shape characteristics (area, perimeter, circularity), seedlings were grown on solid medium for 10 days. Cotyledons were cut off and put in a water filled syringe. To remove the leaf air, the syringe tip was plugged with the finger and the plunger pulled to create a slight vacuum. Cotyledons were mounted in propidium Iodide (10 mg/l) for 3-5 min, prior placing the cover slip. The cotyledon abaxial side was imaged. For analysis, the ImageJ plugin 'StackReg' was used to correct for drift during imaging and a maximum z-projection was generated. Brightness and contrast were adjusted with Photoshop CS5. Image segmentation was executed with a MATLAB Script (Lauster, 2013). Manual correction of the segmentation was performed with Photoshop CS5. The analysis of different pavement cell shape characteristics was conducted with the ImageJ Plugin PaCeQuant and statistical analysis was performed with the corresponding R script (Möller et al., 2017).

Pull-Down experiment

In preparation for the pull-down experiment, RIC1 cDNA, generated from flowers, was amplified with the primer combination RIC1-ATG _F x RIC1-STOP_R. The amplicon was ligated in pGEM T-easy vector (Promega, A1360). pGEM:cRIC1 and pET28:His-MBP-TEV (Currinn et al., 2016) were digested with BamHI/XhoI and appropriate fragments ligated to create pET28:His-MBP-TEV-cRIC1 (Späth, 2017). pET28:His-MBP-TEV and pET28:His-MBP-TEV-cRIC1 were transformed in BL21 *E. coli* expression strain (Genlantis, C700200-GL). 3 ml Luria-Bertani (LB) broth with 50 mg/l Kanamycin (Kan) were inoculated with one colony of BL21 containing either pET28:His-MBP-TEV or pET28:His-MBP-TEV-cRIC1, respectively and bacterial cultures were grown over-night in a shaking incubator (200 rpm) at 28°C. The next morning, 55 ml LB-Kan (25 mg/l) were inoculated with 1 ml pre-culture and grown at 37°C until the OD 0.6 was reached (approximately for 1h). Protein expression was induced by addition of IPTG to a final concentration of 1 mM. The bacterial culture was grown at 18°C for 17 h. Bacterial cells were pelleted in a centrifuge at 11000 rpm and 4°C for 5 min. His-MBP and His-MBP-RIC1 pellets were resuspended in 4.5 ml lysis-buffer (50 mM HEPES, 300 mM NaCl, 10 mM Imidazol, 10% Glycerine, 1 mM TCEP, 5x SigmaFast protease inhibitor

(SLCD0268), 0.0004% Benzonase, pH 8) and sonicated three times for 2 minutes at 4°C with 60% power of the sonicator (Bandelin Sonoplus, UW2070). Subsequently, 450 µl Lysozyme (1 mg/ml) were added and incubated slowly rotating at 4°C for 1 h. The extracts were centrifuged at 11000 rpm and 4°C for 5 min and the supernatant was transferred to a new tube. The protein concentration of the soluble proteins was measured using Bradford assay (Sigma, SLCC0151) and used in pull-down experiments.

Plant protein extracts for pull-down experiments were obtained as follows. Seedlings were grown on solid medium for 5 days. The shoot (leaf and hypocotyl) was separated from the root with a razor blade and frozen in liquid nitrogen. 400 µg of shoots were ground to fine powder in a mortar. 1.4 the amount of shoot material from lysis-buffer (571 µl, 50 mM Tris-HCl pH 7.5, 150 mM NaCl, 0.5% Triton X-100, 5x SigmaFast protease inhibitor) was added to the plant powder and incubated on ice for 30 min. The shoot extract was centrifuged twice at 8000 rpm and 4°C for 5 min. The protein concentrations in the supernatants were measured by Bradford assays and used in the pull-down experiments.

For the pull-down experiments, MBP-Trap (Chromotek) was washed three times with ice cold wash-buffer (10 mM Tris-HCl pH 7.5, 150 mM NaCl, 5x SigmaFast protease inhibitor). 50 µg His-MBP-RIC1 and 25 µg His-MBP protein extracts were mixed at 4°C (slow rotation) with 15 µl MBP-Trap (beads) for 1 h, respectively. The His-MBP-RIC1 and His-MBP-conjugated beads were washed three times with cold wash-buffer. Subsequently, 100-300 µg of HA-mCherry-ROP2 or 600-700 µg of HA-mCherry-ROP6 shoot extracts were added and the MBP-Traps were incubated at 4°C (slow rotation) for another 1 h. The beads were washed four times with wash-buffer and mixed with 60 µl 2x Lämmli-Buffer. Finally, the bound protein was eluted from the beads by incubation at 95°C for 10 min. Total proteins (input), unbound proteins (proteins that did not bind to the beads) and eluate were loaded on two 10% polyacrylamide gels performing SDS-Page. Proteins were transferred onto a 0.45 µm polyvinylidene fluoride (PVDF, Thermo Fisher Scientific, Cat. 88518) membranes for western blot immunodetection. The PVDF membranes were incubated with 5% dry milk in TBST (15 mM NaCl, 5 mM Tris-Base, 25 mM Tris-HCl, 0.1% Tween) at room temperature for 1h. Subsequently, anti-HA antibody coupled to Horseradish peroxidase (HRP, 1:10000, Roche, Cat. 12013819001) was used to detect HA-mCherry-ROPs on the first membrane and HRP-conjugated anti-His antibody (1:4000, Sigma, Cat. A-7058) was used to detect His-MBP and His-MBP-RIC1 on the second membrane. To visualize the protein bands, blots were incubated with BM Chemiluminescence Western Blotting Substrate POD (350 µl on an 8.5 cm x 6 cm PVDF membrane, Roche, Cat. 11500708001) and chemiluminescence was detected on a Fusion Fx7.

Coimmunoprecipitation (Co-IP)

For Co-IP experiments plant protein extracts were obtained as follows. Five day old seedlings were grown on solid medium and frozen in liquid nitrogen. 3.5 g plant material was pestled in a mortar to a fine powder. 5 ml lysis-buffer (50 mM Tris-HCl pH 7.5, 150 mM NaCl, 0.5% Triton X-100, 2x SigmaFast protease inhibitor) was added to the grinded tissue and incubated on ice for 30 min. The extract was centrifuged at 8000 rpm and 4°C for 5 min and filtered through Miracloth (Millipore, Cat. 475855-1R) tissue (Total). 3 ml of seedling extract were mixed with 1.5 ml of lysis-buffer. 25 µl GFP-Trap (Chromotek) were added and the mixture was incubated at 4°C with slow rotation for 1 h. Beads were washed five times with wash-buffer (50 mM Tris-HCl pH 7.5, 150 mM NaCl, 0.2% Triton X-100, 2x SigmaFast protease inhibitor). Subsequently, proteins were eluted by mixing the beads with 50 µl 2x Lämmli-Buffer and incubation at 95°C for 5 min. The supernatant was transferred to a new tube and the elution step repeated with 40 µl 2x Lämmli-Buffer. Total protein, unbound protein and mixed eluates (IP) fractions were loaded on two 10% polyacrylamide gels performing SDS-Page, followed by transfer onto a 0.45 µm PVDF membranes and immunodetection using western blot. The PVDF membranes were blocked with 5% dry milk in TBST (15 mM NaCl, 5 mM Tris-Base, 25 mM Tris-HCl, 0.1% Tween) at room temperature for 1h. Subsequently, anti-HA antibody coupled with HRP (1:10000) was used to detect HA-mCherry-ROPs on one membrane. The second membrane was incubated with the primary anti-GFP antibody from mouse (1:1000, Roche, Cat. 11814460001) and detected with the secondary goat anti-mouse IgG HRP antibody from goat (1:10000, Sigma, Cat. A2554) to detect GFP-PHGAP2. To visualize the protein bands, blots were incubated with BM Chemiluminescence Western Blotting Substrate POD (350 µl on an 8.5 cm x 6 cm PVDF membrane) and chemiluminescence was detected on a Fusion Fx7.

Mating-Based Split-Ubiquitin-System (SUS) assay

To generate PHGAP clones without Stop codon for SUS assays, fragments were amplified with the primer combinations PHGAP1_delta_PH_394_F x PHGAP1_w/o_Stop_R and deltaPHGAP2_400_F x PHGAP2_w/o_Stop_R using pENTR3C:cPHGAP1 and pENTR3C:cPHGAP2 (Stöckle et al., 2016) as templates. The PCR fragments and pENTR3C:PHGAP clones were digested with ScaI/NotI (PHGAP1) and NotI/BglII (PHGAP2) and appropriate fragments were ligated. Finally, pENTR3C:PHGAP1_w/o_stop and pENTR3C:PHGAP2_w/o_stop were recombined with the bait pMetOYC destination vector (Gabor, 2016; Grefen et al., 2007; Grefen et al., 2009), using LR clonase. pENTR3C:cROP2 and pDONR207:cROP6 were recombined with the pNX35-Dest destination vector (Grefen and Blatt, 2012) to generate the prey plasmids via LR reaction. The prey vectors pNX35:PHGAP1$^{130-827}$, pNX35:PHGAP1$^{1-459}$, pNX35:PHGAP2$^{135-870}$, pNX35:PHGAP2$^{1-566}$, pNX35:PHGAP2$^{1-764}$ were generated as previously described (Lotz, 2018).

pENTR3C:cPHGAP1 and pENTR3C:cPHGAP2 together with pNX35-Dest were recombined via LR reaction to obtain the full length PHGAP prey vectors (Stöckle et al., 2016).

The protein phosphatase subunit PP2AA3 was amplified from seedling cDNA with PP2AA3_ATG_KpnI_F x PP2AA3_3'UTR_XhoI_R and together with pENTR3C digested with Ac65I/XhoI and appropriate fragment were ligated. pENTR3C:PP2AA3 was recombined in an LR reaction with pNX35-Dest to generate pNX35:PP2AA3.

The mating-based SUS assay was performed as described previously (Stöckle et al., 2016). Prior mating, yeast cells from AP4 and AP5 strains, expressing the baits and prey plasmids, were harvested before mating to confirm expression of fusion proteins. To extract proteins, yeast pellets were resolved in Urea-Buffer and shredded with glass beads (TissueLyser II, Qiagen). After incubation at 65°C for 10 min and centrifugation at 13000 rpm for another 10 min, the supernatant was loaded on a 7.5% polyacrylamide gel in case of PHGAPs and PP2AA3 and on a 10% gel in case of ROPs performing SDS-Page, followed by transfer onto a 0.45 µm PVDF and 0.2 µm PVDF (ThermoFisher Scientific, Cat. 88520) membrane respectively for western blot immunodetection. For detection of NubG-2xHA fusion proteins (preys), anti-HA antibody coupled with Peroxidase (1:10000) was used. To detect OST4-PHGAP1-Cub-LexA-VP16 and OST4-PHGAP2-Cub-LexA-VP16 (baits), anti-VP16 (1:5000, GeneTex, Cat. GTX30776) was used as primary antibody, followed by incubation with secondary antibody goat anti-rabbit IgG (H+L) HRP conjugated (1:10000, Merck-Millipore, Cat. AP307P). To visualize the protein bands, blots were incubated with BM Chemiluminescence Western Blotting Substrate POD (350 µl on an 8.5 cm x 6 cm PVDF membrane) and chemiluminescence was detected on a Fusion Fx7.

Analysis of microtubule organization

For analysis of microtubule organization, seedlings were grown on solid medium for three days. Image z-stacks were obtained from the cotyledon adaxial side, covering the external periclinal face of the cell up to the median cell plane. The ImageJ plugin 'StackReg' was used to correct for drift, before generating maximum z-projections. The ImageJ plugin Fibril Tool (Boudaoud et al., 2014) was used to analyse the microtubule anisotropy, indicative of microtubule organization (0 indicates disorganization and 1 indicates parallel alignment). For quantification of microtubule organization in neck and central regions (described in Sampathkumar et al., 2014), the background was subtracted by ImageJ function 'Subtract Background' (rolling ball radius 30px) prior the analysis with Fibril Tool. Mean fluorescence intensity in lobes and corresponding indentation regions was analysed with ImageJ (similar analysis described in (Armour et al., 2015)). In brief, a region of interest (ROI) was selected in the lobe, mean grey value was measured, the ROI was rotated 180° and dragged to the corresponding indentation

region in the neighbouring cell to measure the mean grey value there. Lobe/Indentation signal intensity ratio was calculated by dividing lobe mean grey value by the indentation mean grey value.

PHGAP signal analysis on anticlinal cell faces

To analyse PHGAP signal distribution along the anticlinal face, seedlings were grown on solid medium for 2-3 days. The ImageJ Plugin 'StackReg' was used to correct for drift during imaging of the PHGAP z-stack. Only cell walls between two 3-way-junctions and not adjoining stomata were considered for analysis. Each curvature of a segment was analysed separately. A region of interest (ROI) was selected with the segmented line tool (Spline fit selected) and added to the ROI manager. A plot profile of PHGAP signal along the anticlinal face was generated with the ImageJ macro (AMB.IJM) and the MATLAB script (InputFiji.m), as previously described (Belteton et al., 2018). In ImageJ, the anticlinal face image of the ROI selection was generated by defining a substack of the original image that ranged from the top of the anticlinal face to its bottom. Then, the ROI of the curvature was selected from the ROI manager and displayed in the substack image, followed by performing the 'Straighten…' function. Subsequently, a 3D reconstruction of the straightened ROI image was generated and substack slice 85 of the 3D reconstruction selected, which represented the anticlinal face view of the initially selected curvature. The anticlinal face image was used to compare and confirm the PHGAP peaks in the plot profile, to exclude false peak calls in the different curvature regions (apex, flank, outside). As straight cell walls displayed no curvature regions in the plot profile, the normalized segment length was used to define these regions as follows: apex ranging from 0.35-0.65, the two flank regions from 0.2-0.35 and 0.65-0.8 and outside from 0-0.2 and 0.8-1. To determine the radius of the curvature, a maximum z-projection of the original image using the start and stop slice of the anticlinal face was generated. The ROI of the curvature was selected and the ImageJ macro curvature_radius.bsh (Olivier Burri, BIOP, https://gist.github.com/lacan/42f4abe856f697e664d1062c200fd21f) used to identify the curvature fitting circle. The macro provides several possible fitting circles as ROIs. The circle, best fitting the curvature, was selected and the area of the circle measured. The radius (r) was calculated with $r=\sqrt{(A/\pi)}$. Additionally, the length of the ROI (L), which equals the length of the curvature (sector size), was measured and the ratio of sector size (L) and radius (r) (ratio=L/r) was calculated. Based on the sector size/radius ratio, curvatures were classified into curvature classes I-V (Manuscript, Table Figure 4G).

PHGAP/Cytoskeleton co-localization studies and drug treatments

To analyse whether PHGAPs co-localize with microtubules or actin filaments along the anticlinal face, seedlings co-expressing GFP-PHGAP1 and RFP-MBD (microtubule reporter, Lipka et al., 2014) or LifeAct-RFP (actin filament reporter, Cvrčková and Oulehlová, 2017) were grown on solid medium for three days. Subsequently, the seedlings were transferred on solid medium containing 1 µM Latrunculin B (LatB, Sigma-Aldrich, Cat. 428020), 100 µM Oryzalin (Supelco, Cat. 36182), 0.83% DMSO (in case of LatB) or 0.1% ethanol (in case of Oryzalin) as mock control for 24 h. For analysis of microtubule, actin filament and PHGAP co-localization, the approach described for PHGAP signal analysis along the anticlinal face was performed. To evaluate co-localization, the MATLAB script (InputFiji.m, Belteton et al., 2018) was adjusted to display plot profiles of two fluorescence channels. In addition to the localization of GFP-PHGAP1/cytoskeleton in apex, flank or outside of a curvature, it was also scored whether the signal peaks co-localize, show partial overlap or do not co-localize.

Immunolocalization

Immunolocalization was performed as previously described (Lauber et al., 1997; Stöckle et al., 2016). In brief, 6 day old seedlings were harvested in liquid basal medium (BM, ½ Murashige and Skoog medium (MS), 1% sucrose, pH 5.8). Seedlings were transferred in 4% paraformaldehyde dissolved in microtubule-stabilizing buffer (MTSB, 50 mM Pipes, 5 mM EGTA, 5 mM $MgSO_4$, pH 7.0) and incubated for fixation in vacuum at room temperature for 1 h. After fixation, seedlings were washed three times with dH_2O. Seedlings were placed on charged slides (Thermo Scientific, Cat. J1800AMNZ) and dried over night at room temperature. The automated system InsituPro VSi (Intavis) was used for the following steps: Seedlings were rehydrated in dH_20 and MTSB for 5 min each, before the cell wall digestion with 2% Driselase (Sigma-Aldrich, Cat. D9515) in MTSB at 37°C for 1 h. Afterwards, the seedling slides were washed six times (10 min each) with phosphate buffered saline (PBS, 137 mM NaCl, 2.7 mM KCl, 10 mM Na_2HPO_4, 2 mM KH_2PO_4, pH 7.4) and the plasma membrane was permeabilized with 3% Nonident P40 in 10% DMSO-MTSB buffer at room temperature for 1h. After the seedlings were washed again six times for 10 min each with PBS and incubated in 5% bovine serum albumin (BSA, Sigma)/PBS at 37°C for 2 h. Next, the samples were incubated at 37°C with primary antibodies rat anti-tubulin (1:600, Abcam, Cat. ab6160) and rabbit anti-GFP (1:1000, Invitrogen, Cat. A6455) in 5% BSA in PBS for 3 h. The seedlings were washed five times (10 min each) with PBS, before incubation with the secondary antibodies goat anti-rat Cy3 (1:600, Dianova, Cat. 112-165-062) and goat anti-rabbit Alexa 488 (1:600, Invitrogen, Cat. A11008) in 5% BSA/PBS at 37°C for 3 h. After another round of washing five times (10 min each) with PBS, the DNA was stained with 4',6-diamidino-2-phenylindole (DAPI, 1:1000 in PBS) at room temperature for 15 min. Excessive DAPI was

removed by washing three times with PBS for 10 min. In a final step, the roots were mounted in Citifluor (Amersham) and sealed with nail polish. Images were obtained with the Leica TCS SP8 using the settings mentioned above.

Oligonucleotides

Primer	Sequence
Genotyping	
PHGAP1_p954F	actcttatgtacactacatcta
PHGAP1_723_R	acgcttcttccaggatgtccaa
PHGAP1_EcoRI_F	aggcaagacagaattcagtcctgaa
PHGAP1_EcoRI_R	tcttcaggactgaattctgtctt
PHGAP1_1506_R	tactgggagtaactgagggtata
proPHGAP2_F	ctgcagtcgttgttgccatggtttgtaca
PHGAP2_01F	tccggaacctaatagacgtctac
PHGAP2_01_R	tcattatcgtcatcagtcactg
PHGAP2_03_R	agtcgattcctcccagagtt
L4	tgatccatgtagatttcccggacatgaag
LBDsLox	aacgtccgcaatgtgttattaagttgtc
LBa1	tggttcacgtagtgggccatcg
RT-PCR	
PHGAP1_EcoRI_F	aggcaagacagaattcagtcctgaa
PHGAP1_1506_R	tactgggagtaactgagggtata
PHGAP2_01F	tccggaacctaatagacgtctac
PHGAP2_01R	tcattatcgtcatcagtcactg
NUBQ	ggtgctaagaagaggaagaat
CUBQ	ctccttctttctggtaaacgt
Cloning XFP-fusions	
proPHGAP1_3.5kb_F	ggtacctggagattttggcaccgagagcat
proPHGAP1_BglII_GFP_R	aacagctcctcgcccttgctcaccattgcagatctacacacttaatca
proPHGAP_BglII_GFP_F	tgattaagtgtgtagatctgcaatggtgagcaagggcgaggagctgtt
linker_GFP_R	ttcctattctctagaaagtataggaacttccccttgtacagctcgtccatgccgaga
PHGAP1_ATG_F	ggtaccatggaggcttctctagctgtta
PHGAP1_3'UTR_2R_NotI	gcggccgctacctcgttcttgttatgctcat
PHGAP1_ATG_F	ggtaccatggaggcttctctagctgtta
PHGAP1_Stop_R	gcggccgcctaattccatggtggagaaga
linker-PHGAP2_F	tatactttctagagaataggaacttcatggaggcttctttagcggctttgg
PHGAP2_3438_F	tcatttactgtgattatctatccat
PHGAP2_STOP_R	gcggccgcttagttccaaggtggagatgat
deltaPHGAP2-400F	ggatccatgggtcagaatggaatat
PHGAP2_3'UTR	attggcttggtcagaaactcaaga
proPHGAP2_F	ctgcagtcgttgttgccatggtttgtaca
proPHGAP2-GFP_R	aacagctcctcgcccttgctcaccattgcctcaacagcataatct
proPHGAP2_GFP_F	agattatgctgttgaggcaatggtgagcaagggcgaggagctgtt
PHGAP2_764aa_stop_R	tatctagattaacgagatggttgcctgctatt
PHGAP2_566aa_stop_R	tatctagattaatcaaaagacccatctgtggat
PHGAP2_ATG_F	ggatccatggaggcttctttagcggcttt

PHGAP2_Stop_R	gcggccgcttagttccaaggtggagatgat
At5g19390 S447A for	ttgctgatgacgctgatattga
At5g19390 S447A rev	tcaatatcagcgtcatcagcaa
At5g19390 S447E for	ttgctgatgacgaggatattga
At5g19390 S447E rev	tcaatatcctcgtcatcagcaa
ROP2-ATG_F	ggatccatggcgtcaaggtttataaag
ROP2_STOP_R	gaattctcacaagaacgcgcaacggttctt
attB3ROP2F	ggggacaactttgtataataaagttgta atggcgtcaaggtttataaagtgt
attB2ROP2R	ggggaccactttgtacaagaaagctgggtttcacaagaacgcgcaacggttctt
ROP2 G14V_F	tcggagatgttgccgtcggaaa
ROP2 G14V_R	tttccgacggcaacatctccga
ROP2_KpnI_F	atggtaccatggcgtcaaggtttataaagtgt
ROP2_EcoRV_R	atgatatctcacaagaacgcgcaacggttctt
BamHI-ROP6_F	ggatccaccatgagtgcttcaaggtttat
XhoI_ROP6_R	ctcgagatcagagtatagaacaaccttt
Cloning Pull-Down	
RIC1-ATG _F	ggatccccaatggcgacgacaatgaa
RIC1-STOP_R	ctcgagtcagataatatcgttacaggtt
Cloning Spilt-Ubiquitin	
PHGAP1_delta_PH_394_F	ggtaccatggcagcacttgtaattggtcaa
PHGAP1_w/o_Stop_R	atgcggccgcttattccatggtggagaaga
deltaPHGAP2_400_F	ggatccatgggtcagaatggaatat
PHGAP2_w/o_Stop_R	atgcggccgcttgttccaaggtggagatgat
PP2AA3_ATG_KpnI_F	ggggtaccatgtctatggttgatgagccttta
PP2AA3_3'UTR_XhoI_R	ccgctcgagattcgttgctgtcttctttacct

9. References

Thesis:

Gabor, K. E. (2016). Analyse der Protein-Interaktion von Rho of Plants und GTPase aktivierenden Proteinen (PHGAP) und Phänotypisierung von *phgap* Mutanten. Bachelorthesis, Eberhard Karls University Tübingen.

Haller, T. J. (2019). Intermolekulare Interaktionen GTPase aktivierender Proteine (GAPs). Bachelorthesis, Eberhard Karls University Tübingen.

Krieger, N. (2014). Characterization of the putative Rho GTPase activating proteins PHGAP1 and PHGAP2 in respect to auxin regulation and phosphoinositide binding. Masterthesis, Eberhard Karls University Tübingen.

Lauster, T. (2013). Charakterisierung von *gap1gap2* und *gap1gap2rop6* Mutanten und Analyse der Genexpression von GAP2 sowie der Lokalisation von ROP6 und RIC1 in *Arabidopsis thaliana*. Bachelorthesis, Eberhard Karls University Tübingen.

Lotz, P. (2018). Interaktionsstudien zwischen KINESIN-12 und GTPASE AKTIVERENDEN PROTEINEN (GAP) und phänotypische Charakterisierung von ausgewählten *gap* Mutanten. Bachelorthesis, Eberhard Karls University Tübingen.

Späth, E. (2017). Interaktionsstudien zwischen GTPase aktivierenden Proteinen und ausgewählten Interaktionspartnern. Bachelorthesis, Eberhard Karls University Tübingen.

Stöckle, D. (2015) *Arabidopsis thaliana* ROP GTPase activating proteins: At the crossroad of cell division and cell expansion. Dissertation, Eberhard Karls University Tübingen.

Publications:

Alonso, J.M., Stepanova, A.N., Leisse, T.J., Kim, C.J., Chen, H., Shinn, P., Stevenson, D.K., Zimmerman, J., Barajas, P., Cheuk, R*., et al.* (2003). Genome-wide insertional mutagenesis of Arabidopsis thaliana. Science *301*, 653-657.

Altartouri, B., Bidhendi, A.J., Tani, T., Suzuki, J., Conrad, C., Chebli, Y., Liu, N., Karunakaran, C., Scarcelli, G., and Geitmann, A. (2019). Pectin Chemistry and Cellulose Crystallinity Govern Pavement Cell Morphogenesis in a Multi-Step Mechanism. Plant Physiol *181*, 127-141.

Armour, W.J., Barton, D.A., Law, A.M., and Overall, R.L. (2015). Differential Growth in Periclinal and Anticlinal Walls during Lobe Formation in Arabidopsis Cotyledon Pavement Cells. Plant Cell *27*, 2484-2500.

Azimzadeh, J., Nacry, P., Christodoulidou, A., Drevensek, S., Camilleri, C., Amiour, N., Parcy, F., Pastuglia, M., and Bouchez, D. (2008). Arabidopsis TONNEAU1 proteins are essential for preprophase band formation and interact with centrin. Plant Cell *20*, 2146-2159.

Basu, D., Le, J., Zakharova, T., Mallery, E.L., and Szymanski, D.B. (2008). A SPIKE1 signaling complex controls actin-dependent cell morphogenesis through the heteromeric WAVE and ARP2/3 complexes. Proc Natl Acad Sci U S A *105*, 4044-4049.

Baxter-Burrell, A., Yang, Z., Springer, P.S., and Bailey-Serres, J. (2002). RopGAP4-dependent Rop GTPase rheostat control of Arabidopsis oxygen deprivation tolerance. Science *296*, 2026-2028.

Belteton, S.A., Sawchuk, M.G., Donohoe, B.S., Scarpella, E., and Szymanski, D.B. (2018). Reassessing the Roles of PIN Proteins and Anticlinal Microtubules during Pavement Cell Morphogenesis. Plant Physiol *176*, 432-449.

Berken, A., Thomas, C., and Wittinghofer, A. (2005). A new family of RhoGEFs activates the Rop molecular switch in plants. Nature *436*, 1176-1180.

Bidhendi, A.J., Altartouri, B., Gosselin, F.P., and Geitmann, A. (2019). Mechanical Stress Initiates and Sustains the Morphogenesis of Wavy Leaf Epidermal Cells. Cell Rep *28*, 1237-1250 e1236.

Blanchoin, L., Boujemaa-Paterski, R., Henty, J.L., Khurana, P., and Staiger, C.J. (2010). Actin dynamics in plant cells: a team effort from multiple proteins orchestrates this very fast-paced game. Curr Opin Plant Biol *13*, 714-723.

Boudaoud, A., Burian, A., Borowska-Wykret, D., Uyttewaal, M., Wrzalik, R., Kwiatkowska, D., and Hamant, O. (2014). FibrilTool, an ImageJ plug-in to quantify fibrillar structures in raw microscopy images. Nat Protoc *9*, 457-463.

Brembu, T., Winge, P., and Bones, A.M. (2005). The small GTPase AtRAC2/ROP7 is specifically expressed during late stages of xylem differentiation in Arabidopsis. J Exp Bot *56*, 2465-2476.

Camilleri, C., Azimzadeh, J., Pastuglia, M., Bellini, C., Grandjean, O., and Bouchez, D. (2002). The Arabidopsis TONNEAU2 gene encodes a putative novel protein phosphatase 2A regulatory subunit essential for the control of the cortical cytoskeleton. Plant Cell *14*, 833-845.

Cleary, A.L., and Smith, L.G. (1998). The Tangled1 gene is required for spatial control of cytoskeletal arrays associated with cell division during maize leaf development. Plant Cell *10*, 1875-1888.

Clough, S.J., and Bent, A.F. (1998). Floral dip: a simplified method for Agrobacterium-mediated transformation of Arabidopsis thaliana. Plant J *16*, 735-743.

Craddock, C., Lavagi, I., and Yang, Z. (2012). New insights into Rho signaling from plant ROP/Rac GTPases. Trends Cell Biol *22*, 492-501.

Currinn, H., Guscott, B., Balklava, Z., Rothnie, A., and Wassmer, T. (2016). APP controls the formation of PI(3,5)P(2) vesicles through its binding of the PIKfyve complex. Cell Mol Life Sci *73*, 393-408.

Curtis, M.D., and Grossniklaus, U. (2003). A gateway cloning vector set for high-throughput functional analysis of genes in planta. Plant Physiol *133*, 462-469.

Cvrčková, F., and Oulehlová, D. (2017). A new kymogram-based method reveals unexpected effects of marker protein expression and spatial anisotropy of cytoskeletal dynamics in plant cell cortex. Plant Methods *13*, 19.

Dixit, R., and Cyr, R. (2004). Encounters between dynamic cortical microtubules promote ordering of the cortical array through angle-dependent modifications of microtubule behavior. Plant Cell *16*, 3274-3284.

Drevensek, S., Goussot, M., Duroc, Y., Christodoulidou, A., Steyaert, S., Schaefer, E., Duvernois, E., Grandjean, O., Vantard, M., Bouchez, D.*, et al.* (2012). The Arabidopsis TRM1-TON1 interaction reveals a recruitment network common to plant cortical microtubule arrays and eukaryotic centrosomes. Plant Cell *24*, 178-191.

Eklund, D.M., Svensson, E.M., and Kost, B. (2010). Physcomitrella patens: a model to investigate the role of RAC/ROP GTPase signalling in tip growth. J Exp Bot *61*, 1917-1937.

Fu, Y., Gu, Y., Zheng, Z., Wasteneys, G., and Yang, Z. (2005). Arabidopsis interdigitating cell growth requires two antagonistic pathways with opposing action on cell morphogenesis. Cell *120*, 687-700.

Fu, Y., Li, H., and Yang, Z. (2002). The ROP2 GTPase controls the formation of cortical fine F-actin and the early phase of directional cell expansion during Arabidopsis organogenesis. Plant Cell *14*, 777-794.

Fu, Y., Wu, G., and Yang, Z. (2001). Rop GTPase-dependent dynamics of tip-localized F-actin controls tip growth in pollen tubes. J Cell Biol *152*, 1019-1032.

Fu, Y., Xu, T., Zhu, L., Wen, M., and Yang, Z. (2009). A ROP GTPase signaling pathway controls cortical microtubule ordering and cell expansion in Arabidopsis. Curr Biol *19*, 1827-1832.

Galletti, R., and Ingram, G.C. (2015). Communication is key: Reducing DEK1 activity reveals a link between cell-cell contacts and epidermal cell differentiation status. Commun Integr Biol *8*, e1059979.

Gao, Y., Zhang, Y., Zhang, D., Dai, X., Estelle, M., and Zhao, Y. (2015). Auxin binding protein 1 (ABP1) is not required for either auxin signaling or Arabidopsis development. Proc Natl Acad Sci U S A *112*, 2275-2280.

Glover, B.J. (2000). Differentiation in plant epidermal cells. J Exp Bot *51*, 497-505.

Goodson, H.V., and Jonasson, E.M. (2018). Microtubules and Microtubule-Associated Proteins. Cold Spring Harb Perspect Biol *10*.

Grefen, C., and Blatt, M.R. (2012). Do calcineurin B-like proteins interact independently of the serine threonine kinase CIPK23 with the K+ channel AKT1? Lessons learned from a menage a trois. Plant Physiol *159*, 915-919.

Grefen, C., Donald, N., Hashimoto, K., Kudla, J., Schumacher, K., and Blatt, M.R. (2010). A ubiquitin-10 promoter-based vector set for fluorescent protein tagging facilitates temporal stability and native protein distribution in transient and stable expression studies. Plant J *64*, 355-365.

Grefen, C., Lalonde, S., and Obrdlik, P. (2007). Split-ubiquitin system for identifying protein-protein interactions in membrane and full-length proteins. Curr Protoc Neurosci *Chapter 5*, Unit 5 27.

Grefen, C., Obrdlik, P., and Harter, K. (2009). The determination of protein-protein interactions by the mating-based split-ubiquitin system (mbSUS). Methods Mol Biol *479*, 217-233.

Gu, Y., Fu, Y., Dowd, P., Li, S., Vernoud, V., Gilroy, S., and Yang, Z. (2005). A Rho family GTPase controls actin dynamics and tip growth via two counteracting downstream pathways in pollen tubes. J Cell Biol *169*, 127-138.

Gu, Y., Li, S., Lord, E.M., and Yang, Z. (2006). Members of a novel class of Arabidopsis Rho guanine nucleotide exchange factors control Rho GTPase-dependent polar growth. Plant Cell *18*, 366-381.

Gutierrez, R., Lindeboom, J.J., Paredez, A.R., Emons, A.M., and Ehrhardt, D.W. (2009). Arabidopsis cortical microtubules position cellulose synthase delivery to the plasma membrane and interact with cellulose synthase trafficking compartments. Nat Cell Biol *11*, 797-806.

Hamant, O., Heisler, M.G., Jönsson, H., Krupinski, P., Uyttewaal, M., Bokov, P., Corson, F., Sahlin, P., Boudaoud, A., Meyerowitz, E.M.*, et al.* (2008). Developmental patterning by mechanical signals in Arabidopsis. Science *322*, 1650-1655.

Herrmann, A., Livanos, P., Lipka, E., Gadeyne, A., Hauser, M.T., Van Damme, D., and Muller, S. (2018). Dual localized kinesin-12 POK2 plays multiple roles during cell division and interacts with MAP65-3. EMBO Rep *19*.

Hodges, M., Jossier, M., Boex-Fontvieille, E., and Tcherkez, G. (2013). Protein phosphorylation and photorespiration. Plant Biol (Stuttg) *15*, 694-706.

Huang, J.B., Liu, H., Chen, M., Li, X., Wang, M., Yang, Y., Wang, C., Huang, J., Liu, G., Liu, Y.*, et al.* (2014). ROP3 GTPase contributes to polar auxin transport and auxin responses and is important for embryogenesis and seedling growth in Arabidopsis. Plant Cell *26*, 3501-3518.

Huesmann, C., Hoefle, C., and Huckelhoven, R. (2011). ROPGAPs of Arabidopsis limit susceptibility to powdery mildew. Plant Signal Behav *6*, 1691-1694.

Hwang, J.-U., Vernoud, V., Szumlanski, A., Nielsen, E., and Yang, Z. (2008). A Tip-Localized RhoGAP Controls Cell Polarity by Globally Inhibiting Rho GTPase at the Cell Apex. Current Biology *18*, 1907-1916.

Hwang, J.U., Wu, G., Yan, A., Lee, Y.J., Grierson, C.S., and Yang, Z. (2010). Pollen-tube tip growth requires a balance of lateral propagation and global inhibition of Rho-family GTPase activity. J Cell Sci *123*, 340-350.

Jacques, E., Verbelen, J.P., and Vissenberg, K. (2014). Review on shape formation in epidermal pavement cells of the Arabidopsis leaf. Funct Plant Biol *41*, 914-921.

Janski, N., Masoud, K., Batzenschlager, M., Herzog, E., Evrard, J.L., Houlne, G., Bourge, M., Chaboute, M.E., and Schmit, A.C. (2012). The GCP3-interacting proteins GIP1 and GIP2 are required for gamma-tubulin complex protein localization, spindle integrity, and chromosomal stability. Plant Cell *24*, 1171-1187.

Job, D., Valiron, O., and Oakley, B. (2003). Microtubule nucleation. Curr Opin Cell Biol *15*, 111-117.

Kirik, A., Ehrhardt, D.W., and Kirik, V. (2012). TONNEAU2/FASS regulates the geometry of microtubule nucleation and cortical array organization in interphase Arabidopsis cells. Plant Cell *24*, 1158-1170.

Klahre, U., and Kost, B. (2006). Tobacco RhoGTPase ACTIVATING PROTEIN1 spatially restricts signaling of RAC/Rop to the apex of pollen tubes. Plant Cell *18*, 3033-3046.

Kost, B. (2008). Spatial control of Rho (Rac-Rop) signaling in tip-growing plant cells. Trends Cell Biol *18*, 119-127.

Kost, B., Lemichez, E., Spielhofer, P., Hong, Y., Tolias, K., Carpenter, C., and Chua, N.H. (1999). Rac homologues and compartmentalized phosphatidylinositol 4, 5-bisphosphate act in a common pathway to regulate polar pollen tube growth. J Cell Biol *145*, 317-330.

Kulich, I., Vogler, F., Bleckmann, A., Cyprys, P., Lindemeier, M., Fuchs, I., Krassini, L., Schubert, T., Steinbrenner, J., Beynon, J.*, et al.* (2020). ARMADILLO REPEAT ONLY proteins confine Rho GTPase signalling to polar growth sites. Nat Plants *6*, 1275-1288.

Lauber, M.H., Waizenegger, I., Steinmann, T., Schwarz, H., Mayer, U., Hwang, I., Lukowitz, W., and Jürgens, G. (1997). The Arabidopsis KNOLLE protein is a cytokinesis-specific syntaxin. J Cell Biol *139*, 1485-1493.

Lee, G.Y., Cheung, K., Chang, W., and Lee, L.P. (2000). Mechanical interlocking with precisely controlled nano-and microscale geometries for implantable microdevices. Paper presented at: 1st Annual International IEEE-EMBS Special Topic Conference on Microtechnologies in Medicine and Biology Proceedings (Cat No 00EX451) (IEEE).

Lee, Y.J., Szumlanski, A., Nielsen, E., and Yang, Z. (2008). Rho-GTPase-dependent filamentous actin dynamics coordinate vesicle targeting and exocytosis during tip growth. J Cell Biol *181*, 1155-1168.

Lemmon, M.A. (2008). Membrane recognition by phospholipid-binding domains. Nat Rev Mol Cell Biol *9*, 99-111.

Li, H., Lin, D., Dhonukshe, P., Nagawa, S., Chen, D., Friml, J., Scheres, B., Guo, H., and Yang, Z. (2011). Phosphorylation switch modulates the interdigitated pattern of PIN1 localization and cell expansion in Arabidopsis leaf epidermis. Cell Res *21*, 970-978.

Li, H., Lin, Y., Heath, R.M., Zhu, M.X., and Yang, Z. (1999). Control of pollen tube tip growth by a Rop GTPase-dependent pathway that leads to tip-localized calcium influx. Plant Cell *11*, 1731-1742.

Liang, H., Zhang, Y., Martinez, P., Rasmussen, C.G., Xu, T., and Yang, Z. (2018). The Microtubule-Associated Protein IQ67 DOMAIN5 Modulates Microtubule Dynamics and Pavement Cell Shape. Plant Physiol *177*, 1555-1568.

Liang, S., Yang, X., Deng, M., Zhao, J., Shao, J., Qi, Y., Liu, X., Yu, F., and An, L. (2019). A New Allele of the SPIKE1 Locus Reveals Distinct Regulation of Trichome and Pavement Cell Development and Plant Growth. Front Plant Sci *10*, 16.

Lin, D., Cao, L., Zhou, Z., Zhu, L., Ehrhardt, D., Yang, Z., and Fu, Y. (2013). Rho GTPase signaling activates microtubule severing to promote microtubule ordering in Arabidopsis. Curr Biol *23*, 290-297.

Lin, Y., and Yang, Z. (1997). Inhibition of Pollen Tube Elongation by Microinjected Anti-Rop1Ps Antibodies Suggests a Crucial Role for Rho-Type GTPases in the Control of Tip Growth. Plant Cell *9*, 1647-1659.

Lipka, E., Gadeyne, A., Stockle, D., Zimmermann, S., De Jaeger, G., Ehrhardt, D.W., Kirik, V., Van Damme, D., and Muller, S. (2014). The Phragmoplast-Orienting Kinesin-12 Class Proteins Translate the Positional Information of the Preprophase Band to Establish the Cortical Division Zone in Arabidopsis thaliana. Plant Cell *26*, 2617-2632.

Lipka, E., Herrmann, A., and Mueller, S. (2015). Mechanisms of plant cell division. Wiley Interdiscip Rev Dev Biol *4*, 391-405.

Marc, J., Granger, C.L., Brincat, J., Fisher, D.D., Kao, T., McCubbin, A.G., and Cyr, R.J. (1998). A GFP-MAP4 reporter gene for visualizing cortical microtubule rearrangements in living epidermal cells. Plant Cell *10*, 1927-1940.

Martinez, P., Dixit, R., Balkunde, R.S., Zhang, A., O'Leary, S.E., Brakke, K.A., and Rasmussen, C.G. (2020). TANGLED1 mediates microtubule interactions that may promote division plane positioning in maize. J Cell Biol *219*.

Masoud, K., Herzog, E., Chaboute, M.E., and Schmit, A.C. (2013). Microtubule nucleation and establishment of the mitotic spindle in vascular plant cells. Plant J *75*, 245-257.

Mineyuki, Y., and Palevitz, B. (1990). Relationship between preprophase band organization, F-actin and the division site in Allium: Fluorescence and morphometric studies on cytochalasin-treated cells. Journal of Cell Science *97*, 283-295.

Mitchison, T., and Kirschner, M. (1984). Dynamic instability of microtubule growth. Nature *312*, 237-242.

Mitra, D., Klemm, S., Kumari, P., Quegwer, J., Moller, B., Poeschl, Y., Pflug, P., Stamm, G., Abel, S., and Burstenbinder, K. (2019). Microtubule-associated protein IQ67 DOMAIN5 regulates morphogenesis of leaf pavement cells in Arabidopsis thaliana. J Exp Bot *70*, 529-543.

Möller, B., Poeschl, Y., Plotner, R., and Burstenbinder, K. (2017). PaCeQuant: A Tool for High-Throughput Quantification of Pavement Cell Shape Characteristics. Plant Physiol *175*, 998-1017.

Morejohn, L.C., Bureau, T.E., Molè-Bajer, J., Bajer, A.S., and Fosket, D.E. (1987). Oryzalin, a dinitroaniline herbicide, binds to plant tubulin and inhibits microtubule polymerization in vitro. Planta *172*, 252-264.

Müller, S., Han, S., and Smith, L.G. (2006). Two kinesins are involved in the spatial control of cytokinesis in Arabidopsis thaliana. Curr Biol *16*, 888-894.

Müller, S., and Jürgens, G. (2016). Plant cytokinesis-No ring, no constriction but centrifugal construction of the partitioning membrane. Semin Cell Dev Biol *53*, 10-18.

Nagashima, Y., Tsugawa, S., Mochizuki, A., Sasaki, T., Fukuda, H., and Oda, Y. (2018). A Rho-based reaction-diffusion system governs cell wall patterning in metaxylem vessels. Sci Rep *8*, 11542.

Neuhaus, J.M., Wanger, M., Keiser, T., and Wegner, A. (1983). Treadmilling of actin. J Muscle Res Cell Motil *4*, 507-527.

Nibau, C., Tao, L., Levasseur, K., Wu, H.M., and Cheung, A.Y. (2013). The Arabidopsis small GTPase AtRAC7/ROP9 is a modulator of auxin and abscisic acid signalling. J Exp Bot *64*, 3425-3437.

Oda, Y., and Fukuda, H. (2012). Initiation of cell wall pattern by a Rho- and microtubule-driven symmetry breaking. Science *337*, 1333-1336.

Ohashi-Ito, K., Oda, Y., and Fukuda, H. (2010). Arabidopsis VASCULAR-RELATED NAC-DOMAIN6 directly regulates the genes that govern programmed cell death and secondary wall formation during xylem differentiation. Plant Cell *22*, 3461-3473.

Pan, X., Fang, L., Liu, J., Senay-Aras, B., Lin, W., Zheng, S., Zhang, T., Guo, J., Manor, U., Van Norman, J.*, et al.* (2020). Auxin-induced signaling protein nanoclustering contributes to cell polarity formation. Nat Commun *11*, 3914.

Paredez, A.R., Somerville, C.R., and Ehrhardt, D.W. (2006). Visualization of cellulose synthase demonstrates functional association with microtubules. Science *312*, 1491-1495.

Pastuglia, M., Azimzadeh, J., Goussot, M., Camilleri, C., Belcram, K., Evrard, J.L., Schmit, A.C., Guerche, P., and Bouchez, D. (2006). Gamma-tubulin is essential for microtubule organization and development in Arabidopsis. Plant Cell *18*, 1412-1425.

Pickett-Heaps, J.D. (1969). Preprophase microtubules and stomatal differentiation; some effects of centrifugation on symmetrical and asymmetrical cell division. J Ultrastruct Res *27*, 24-44.

Pickett-Heaps, J.D., and Northcote, D.H. (1966). Cell division in the formation of the stomatal complex of the young leaves of wheat. J Cell Sci *1*, 121-128.

Pollard, T.D., Blanchoin, L., and Mullins, R.D. (2000). Molecular mechanisms controlling actin filament dynamics in nonmuscle cells. Annu Rev Biophys Biomol Struct *29*, 545-576.

Pollard, T.D., and Cooper, J.A. (1986). Actin and actin-binding proteins. A critical evaluation of mechanisms and functions. Annu Rev Biochem *55*, 987-1035.

Ren, H., Dang, X., Yang, Y., Huang, D., Liu, M., Gao, X., and Lin, D. (2016). SPIKE1 Activates ROP GTPase to Modulate Petal Growth and Shape. Plant Physiol *172*, 358-371.

Rodionov, V.I., and Borisy, G.G. (1997). Microtubule treadmilling in vivo. Science *275*, 215-218.

Sampathkumar, A., Krupinski, P., Wightman, R., Milani, P., Berquand, A., Boudaoud, A., Hamant, O., Jonsson, H., and Meyerowitz, E.M. (2014). Subcellular and supracellular mechanical stress prescribes cytoskeleton behavior in Arabidopsis cotyledon pavement cells. Elife *3*, e01967.

Sapala, A., Runions, A., Routier-Kierzkowska, A.L., Das Gupta, M., Hong, L., Hofhuis, H., Verger, S., Mosca, G., Li, C.B., Hay, A.*, et al.* (2018). Why plants make puzzle cells, and how their shape emerges. Elife *7*.

Schaefer, A., Hohner, K., Berken, A., and Wittinghofer, A. (2011). The unique plant RhoGAPs are dimeric and contain a CRIB motif required for affinity and specificity towards cognate small G proteins. Biopolymers *95*, 420-433.

Schaefer, E., Belcram, K., Uyttewaal, M., Duroc, Y., Goussot, M., Legland, D., Laruelle, E., de Tauzia-Moreau, M.L., Pastuglia, M., and Bouchez, D. (2017). The preprophase band of microtubules controls the robustness of division orientation in plants. Science *356*, 186-189.

Shaw, S.L., Kamyar, R., and Ehrhardt, D.W. (2003). Sustained microtubule treadmilling in Arabidopsis cortical arrays. Science *300*, 1715-1718.

Smertenko, A., Assaad, F., Baluska, F., Bezanilla, M., Buschmann, H., Drakakaki, G., Hauser, M.T., Janson, M., Mineyuki, Y., Moore, I.*, et al.* (2017). Plant Cytokinesis: Terminology for Structures and Processes. Trends Cell Biol *27*, 885-894.

Sotiriou, P., Giannoutsou, E., Panteris, E., Galatis, B., and Apostolakos, P. (2018). Local differentiation of cell wall matrix polysaccharides in sinuous pavement cells: its possible involvement in the flexibility of cell shape. Plant Biol (Stuttg) *20*, 223-237.

Spector, I., Shochet, N.R., Kashman, Y., and Groweiss, A. (1983). Latrunculins: novel marine toxins that disrupt microfilament organization in cultured cells. Science *219*, 493-495.

Spinner, L., Gadeyne, A., Belcram, K., Goussot, M., Moison, M., Duroc, Y., Eeckhout, D., De Winne, N., Schaefer, E., Van De Slijke, E.*, et al.* (2013). A protein phosphatase 2A complex spatially controls plant cell division. Nat Commun *4*, 1863.

Staehelin, L.A., and Hepler, P.K. (1996). Cytokinesis in higher plants. Cell *84*, 821-824.

Staiger, C.J., Sheahan, M.B., Khurana, P., Wang, X., McCurdy, D.W., and Blanchoin, L. (2009). Actin filament dynamics are dominated by rapid growth and severing activity in the Arabidopsis cortical array. J Cell Biol *184*, 269-280.

Stöckle, D., Herrmann, A., Lipka, E., Lauster, T., Gavidia, R., Zimmermann, S., and Muller, S. (2016). Putative RopGAPs impact division plane selection and interact with kinesin-12 POK1. Nat Plants *2*, 16120.

Thomas, C., Tholl, S., Moes, D., Dieterle, M., Papuga, J., Moreau, F., and Steinmetz, A. (2009). Actin bundling in plants. Cell Motil Cytoskeleton *66*, 940-957.

Torres-Ruiz, R.A., and Jürgens, G. (1994). Mutations in the FASS gene uncouple pattern formation and morphogenesis in Arabidopsis development. Development *120*, 2967-2978.

Traas, J., Bellini, C., Nacry, P., Kronenberger, J., Bouchez, D., and Caboche, M. (1995). Normal differentiation patterns in plants lacking microtubular preprophase bands. Nature *375*, 676-677.

Vos, J.W., Dogterom, M., and Emons, A.M. (2004). Microtubules become more dynamic but not shorter during preprophase band formation: a possible "search-and-capture" mechanism for microtubule translocation. Cell Motil Cytoskeleton *57*, 246-258.

Walker, K.L., Müller, S., Moss, D., Ehrhardt, D.W., and Smith, L.G. (2007). Arabidopsis TANGLED identifies the division plane throughout mitosis and cytokinesis. Curr Biol *17*, 1827-1836.

Wang, W., Liu, Z., Bao, L.J., Zhang, S.S., Zhang, C.G., Li, X., Li, H.X., Zhang, X.L., Bones, A.M., Yang, Z.B.*, et al.* (2017). The RopGEF2-ROP7/ROP2 Pathway Activated by phyB Suppresses Red Light-Induced Stomatal Opening. Plant Physiol *174*, 717-731.

Wittinghofer, A., and Pai, E.F. (1991). The structure of Ras protein: a model for a universal molecular switch. Trends Biochem Sci *16*, 382-387.

Wu, G., Gu, Y., Li, S., and Yang, Z. (2001). A genome-wide analysis of Arabidopsis Rop-interactive CRIB motif-containing proteins that act as Rop GTPase targets. Plant Cell *13*, 2841-2856.

Wu, G., Li, H., and Yang, Z. (2000). Arabidopsis RopGAPs are a novel family of rho GTPase-activating proteins that require the Cdc42/Rac-interactive binding motif for rop-specific GTPase stimulation. Plant Physiol *124*, 1625-1636.

Wu, Y., Zhao, S., Tian, H., He, Y., Xiong, W., Guo, L., and Wu, Y. (2013). CPK3-phosphorylated RhoGDI1 is essential in the development of Arabidopsis seedlings and leaf epidermal cells. J Exp Bot *64*, 3327-3338.

Xu, T., Dai, N., Chen, J., Nagawa, S., Cao, M., Li, H., Zhou, Z., Chen, X., De Rycke, R., Rakusova, H.*, et al.* (2014). Cell surface ABP1-TMK auxin-sensing complex activates ROP GTPase signaling. Science *343*, 1025-1028.

Xu, T., Wen, M., Nagawa, S., Fu, Y., Chen, J.G., Wu, M.J., Perrot-Rechenmann, C., Friml, J., Jones, A.M., and Yang, Z. (2010). Cell surface- and rho GTPase-based auxin signaling controls cellular interdigitation in Arabidopsis. Cell *143*, 99-110.

Xu, X.M., Zhao, Q., Rodrigo-Peiris, T., Brkljacic, J., He, C.S., Müller, S., and Meier, I. (2008). RanGAP1 is a continuous marker of the Arabidopsis cell division plane. Proc Natl Acad Sci U S A *105*, 18637-18642.

Yalovsky, S., Bloch, D., Sorek, N., and Kost, B. (2008). Regulation of membrane trafficking, cytoskeleton dynamics, and cell polarity by ROP/RAC GTPases. Plant Physiol *147*, 1527-1543.

10. Appendix

Putative RopGAPs impact division plane selection and interact with kinesin-12 POK1

Dorothee Stöckle, Arvid Herrmann, Elisabeth Lipka, **Theresa Lauster**,

Richard Gavidia, Steffi Zimmermann and Sabine Müller

Nat Plants. 2016 Aug 8; 2:16120. doi: 10.1038/nplants.2016.120. PMID: 27501519.

Putative RopGAPs impact division plane selection and interact with kinesin-12 POK1

Dorothee Stöckle[1], Arvid Herrmann, Elisabeth Lipka, Theresa Lauster, Richard Gavidia, Steffi Zimmermann, Sabine Müller[*]

Developmental Genetics, Centre for Plant Molecular Biology (ZMBP), University of Tübingen
Auf der Morgenstelle 32, 72076 Tübingen, Germany

[1] current address: The Sainsbury Laboratory, University of Cambridge, Bateman Street, Cambridge CB2 1LR, United Kingdom

email: sabine.mueller@zmbp.uni-tuebingen.de

[*] Corresponding author: Sabine Müller

In plants, cell shape is defined by the surrounding cell walls. Thus, spatial control over cell division planes and cell expansion polarity are essential to maintain cell morphology. As in non-plant organisms cell polarity and expansion in plants are controlled by Rho GTPase signaling, regulating cytoskeletal reorganization and vesicle trafficking [1]. However, unlike non-plant eukaryotes, Rho signaling was not implicated in mitotic events in plants. Here, we report on a pair of putative Rho GTPase activating proteins (RhoGAPs) that interact with the mitosis-specific kinesin-12 POK1, a core component of the cortical division zone/site (CDZ/CDS) that is required for division plane maintenance in *Arabidopsis* [2-4]. While designated PHGAPs are cytoplasmic and plasma membrane associated in interphase, during mitosis they additionally localize to the CDZ/CDS in a POK-dependent manner. In contrast to *pok1 pok2* mutants, *phgap1 phgap2* double mutants show moderate cell wall positioning defects as a consequence of inaccurate positioning of the cortical division zone marker POK1. We conclude that loss of PHGAP function interferes with division plane selection in proliferative cell divisions.

In recent years, several CDZ/CDS-resident proteins were identified, memorizing the positional information given by the preprophase band (PPB). The kinesin-12 class motor protein, POK1 is one critical component of the CDZ/CDS, required for the efficient recruitment and maintenance of CDZ identity-markers TANGLED (TAN) and RanGAP1 [2-4]. In the *Arabidopsis* root meristem, simultaneous loss of POK1 and POK2 leads to phragmoplast guidance defects and severe cell plate mis-positioning resulting in deformed cells [4].

In search for novel POK1 interactors, we identified a pair of putative Rho-GAPs in a yeast two-hybrid screen. Commonly, GAPs stimulate the intrinsic GTPase activity of their respective small GTPase targets, rendering the GTPase inactive [5]. Rho-based regulatory mechanism control numerous cellular processes via polarity establishment, cytoskeletal reorganization and vesicle-trafficking in distinct subcellular domains of plant cells. Well documented examples are multipolar pavement cell formation, polar pollen tubes growth, secondary cell wall formation [1,6-8] in *Arabidopsis* and division asymmetry of maize stomatal complexes [9]. In non-plant eukaryotes, Rho-activity directs polarity establishment, motility and cell division [10,11]. However, there is no prior evidence of a role for ROP signaling in division plane orientation for symmetric divisions in the root meristem.

The novel POK1 interactors share conserved protein domain architecture (Figure 1a) with the *bona fide*, pollen-specific GAP, ROP1 enhancer (REN1) [12]. The N-terminal pleckstrin-homology (PH) domain is flanked by the GAP domain that contains a conserved arginin (R, Figure 1a) essential for GAP-function of REN1 and of mammalian RhoGAPs [12]. The C-terminal, coiled coil containing domain, interacted with POK1 (CC, Figure1a, 1c, 1d) in the initial yeast two-hybrid screen. We performed mating-based split-ubiquitin interaction assays in yeast [13] to confirm the interaction between PHGAPs and two POK1 C-terminal protein

truncations. The longer $POK1_{1213-2066}$ C-terminal is sufficient for CDZ/CDS localization, whereas the shorter $POK1_{1683-2066}$ is sufficient for interaction with TAN [4,14]. PHGAP1 and PHGAP2 interacted with both POK1-C terminal variants (Figure 1b, 1c). Furthermore, ratiometric bimolecular fluorescent complementation (rBiFC) experiments [15] between nYFP-$POK1_{1683-2066}$ and cYFP-PHGAP2 corroborated *in planta* protein interaction in *Arabidopsis* root protoplasts (Figure S1a-S1d). Thus, we conclude that PHGAP1 and PHGAP2, both interact with the C-terminus of POK1.

rBiFC experiments also support an expected interaction between PHGAP2 and ROPs. As proof of principle we tested interaction with ROP2 and ROP6 (Figure 1d, 1e, 1g), a pair of ROP proteins, antagonistically regulating cytoskeletal dynamic and organization during pavement cell development, as well as ROP1, ROP3 and ROP4 (Figure S1j, 1k, 1l). While PHGAP2 interacted with all tested ROPs, neither PHGAP2 nor ROPs showed explicit n/cYFP complementation when tested with TAN (Figure 1f, 1g, 1h, 1i and Figure S1) [4]. These results suggest interaction between PHGAPs and ROPs, as has been reported for the PHGAP homolog REN1, which regulates ROP1 activity in pollen tube expansion [12]. The BiFC experiments showed unspecific interaction of PHGAPs and ROPs. Thus, the physiologically relevant ROP-targets of PHGAPs still need to be determined.

We further characterized POK1 and PHGAP interactions by examining the subcellular localization of PHGAPs. Expression of PHGAPs using cDNA constructs *pUBN:GFP-PHGAP1* and *pUBN:GFP-PHGAP2*, and the full genomic construct *pPHGAP2:GFP-PHGAP2* resulted in comparable localization patterns in transgenic wild type plants (Figure 2 and S2). Interphase cells displayed cytoplasmic and plasma membrane associated fluorescent signal (Figure 2a-2f and S2a-S2j). However, a subset of cells showed continuous GFP-PHGAP1 and GFP-PHGAP2 rings at the plasma membrane (Figure 2a-d and S2a, S2b), reminiscent of the prominent YFP-POK1 rings at the CDZ/CDS [4]. As previously reported, YFP-POK1 is recruited to the PPB in prophase and occupies the CDZ/CDS throughout mitosis by a yet unknown mechanism [4].

Therefore, we determined the cell cycle stage of PHGAP ring-localization at the plasma membrane and its dependency on POK function. While cells displaying spindles, exhibit moderate GFP-PHGAP1 ring accumulation that exceeds the cytoplasmic and membrane associated GFP-PHGAP1 pool, distinctive GFP-PHGAP1 rings were observed during cytokinesis (Figure 2f, 2i, S2c). Co-expression of YFP-POK1 and RFP-PHGAP1 confirmed the expected co-localization in a subset of cells with YFP-POK1 rings (Figure 2j, n= 9 roots, displaying (n = 21) YFP-POK1 rings and (n = 12) RFP-PHGAP1 rings). We know from our previous POK1 analysis [4], that YFP-POK1 starts accumulating at the CDZ in prophase, while PHGAPs are uniformly distributed in the cytoplasm and at the plasma membrane in prophase

and visibly accumulate at the CDZ in meta- and anaphase(Figure 2f and S2c), when YFP-POK1 is already present.

Similarly, GFP-PHGAP2 faintly accumulates at the CDZ during meta-/anaphase (Figure 2e, S2d-S2g) and remains present during cytokinesis (Figure 2e and 2h, S2h-S2j). Therefore, we conclude that both PHGAP1 and PHGAP2 localize uniformly in the cytoplasm and the plasma membrane in prophase cells and enrichment at the CDZ becomes noticeable in meta-/anaphase and remains throughout cytokinesis (Figure 2 and S2).

Next we asked whether PHGAP localization at the CDZ/CDS depended on POK-function. In the *pok1-1 pok2-3* mutant GFP-PHGAP1 rings were absent from the CDZ/CDS in cells with PPBs (n = 4), spindles (n = 6) and phragmoplasts (n = 19), despite detectable cytoplasmic and plasma membrane associated GFP-PHGAP signal (Figure 2g). Likewise, GFP-PHGAP2 rings were never observed in *pok1-1 pok2-3* mutants (n = 20 cytokinetic cells with cell plates in eight mutant roots, Figure S2k). These observations suggest that POK function is critically required for the distinct accumulation of PHGAPs at the CDZ/CDS, as has been reported before, for the CDZ/CDS resident proteins TAN and RanGAP1 [3,4]. However, TAN and RanGAP1 recruitment to the PPB occurs independent of POKs during prophase and only their maintenance at the CDZ upon metaphase is POK-dependent. In contrast, PHGAPs are uniformly distributed in prophase and POK-dependent PHGAP accumulation at the CDZ becomes detectable only during metaphase. Remarkably, PHGAPs cytoplasmic and plasma membrane localization are not noticeably affected by the loss of POK function.

The protein interaction and dependency of PHGAPs on the mitosis specific POK1 motivated our analysis of PHGAPs roles in cell division using available T-DNA insertion lines (Figure S3a). *PHGAP1* transcript was abolished in the *phgap1* allele (Figure S3b) and *PHGAP2* transcript was massively diminished in the *phgap2* allele (Figure S3c). However, the *phgap1* and *phgap2* single mutants did not show appreciable mutant phenotypes. Thus, the double mutant *phgap1 phgap2* was used for further experimentation (Figure S3d, S3e, S3f).

The *Arabidopsis* root meristem exhibits regular cell divisions, reflected in a well ordered cell wall pattern. *phgap1 phgap2* seedling roots showed moderate reduction in root growth compared to wild type (Figure 3a). The complementation line, expressing *pPHGAP2:GFP-PHGAP2* showed a partial rescue of root growth, as it did not differ from wild type nor *phgap1 phgap2* mutant (Figure 3a). The *phgap1 phgap2* phenotype was less severe than the *pok1 pok2* double mutant (Figure S4a). On the cellular level, *phgap1 phgap2* root meristems displayed moderate cell wall positioning defects compared to wild type (Figure 3b, 3c), which were markedly diminished by *pPHGAP2:GFP-PH*GAP2 expression (Figure 3d).

The *pok1-1 pok2-3 phgap1 phgap2* quadruple mutant (Figure S3g, S3h, S3k, S3i) did show phenotype enhancement in aerial tissues, suggesting *PHGAP1* and *PHGAP2* might serve additional functions. While *pok1-1 pok2-3* double mutants, and *pok1-1 pok2-3 phgap1/+*

phgap2 or *pok1-1 pok2-3 phgap1 phgap2*/+ sesqui-mutants still produce viable progeny, the quadruple mutant *pok1-1 pok2-3 phgap1-1 phgap2-1* descendants contained mostly non-fertilized ovules and produced very few non- viable embryos (Figure S3g-m). However, root growth and cell division pattern in the root meristem were similar to that of *pok1-1 pok2-3* double mutant (Figure S4a, S4c).

Also *Arabidopsis* early embryo development follows a recurring sequence of cell divisions creating a typecast cell patterns [16]. Globular and early heart stage embryos of *phgap1 phgap2* double mutants displayed irregular cell patterns and abnormally positioned cell walls (Figure 3e-3j). Although the penetrance of the defect was 6.6 % of the investigated embryos (n = 366), expression of *pGAP2:GFP-gPHGAP2* (n = 638, Figure 3g) reduced the number of abnormal embryos to 2.6 %, while only 0.9% of wild type embryos (n = 685) were abnormal (Figure 3d, 3h). Thus, we suggest that redundant function of PHGAP1 and PHGAP2 play a role in cell division plane positioning in the root meristem and in the early stages of embryo development.

To determine PHGAPs requirement during cell division, we investigated the organization of mitotic microtubule arrays in the *phgap1 phgap2* double mutant root meristem and found instances, where PPBs and phragmoplasts deviated from the expected transverse orientation, predominant in wild type (Figure 4a-4d). Since POK1 is recruited to the PPB in prophase and preserves the PPBs positional information at the CDZ/CDS [4], we examined whether POK1 orientation co-aligned with PPBs and phragmoplasts in the *phgap1 phgap2* mutant (Figure 4e). We never observed miss-alignments of microtubule array orientation and POK1 orientation (n > 100 POK1 rings), indicating that POK1 orientation also reiterate the PPB position in the *phgap1 phgap2* double mutant, even in cases of oblique PPBs. Thus, we determined the position of POK1 rings relative to the expected transverse orientation, usually observed in wild type, as a read-out for division plane positioning defects. We defined different angle classes of deviation (>5° - ≤ 10°, >10° - ≤ 15°, > 15° and ellipse, which we observe when the division plane tilted perpendicular to the focal plane, Figure 4f) from the ideal transverse (0° to ≤5°) orientation. The mean deviation of POK1 from the transverse increased significantly in the *phgap1 phgap2* mutant (Figure 4g). While the majority of POK1 rings deviated only up to 5° from the expected transverse orientation in wild type (74 %), the frequency of POK1 rings in this class dropped in the *phgap1 phgap2* mutants (46 %) (Figure 4h). Instead, the frequency of POK1 rings, deviating between >5° - ≤ 10°, >10° - ≤ 15° and > 15° from the transverse, increased in the *phgap1 phgap2* mutant (Figure 4h). Thus, we conclude that loss of PHGAP function interferes with division plane selection and appropriate PPB positioning. To validate this notion, we compared PPB and phragmoplast orientations between wild type, the *phgap1 phgap2* mutant and the rescue line expressing *pPHGAP2:GFP-gPHGAP2* in *phgap1 phgap2*. Both, the mean PPB deviation angle and the mean phragmoplast deviation angle differed significantly in the *phgap1 phgap2* mutant compared to wild type and compared to the rescue

line (Figure 4i, 4j), while PPB orientation and phragmoplast orientations of the same genotype (i.e. wild type PPB vs. wild type phragmoplast, etc.) did not differ. Like POK1, PPBs and phragmoplasts, displayed a shift towards larger angle classes in the *phgap1 phgap2* double mutant compared to wild type, a tendency that was reversed in the rescue line (Figure 4k, 4l). These observations suggest that loss of PHGAP function leads to an inaccurate demarcation of the CDZ due to mis-oriented PPBs, which consequently affects POK1 positioning.

To determine, whether PHGAPs localization at the CDZ depend on their GAP function, we generated non-functional GFP-PHGAP mutants and introduced them into the *phgap1 phgap2* double mutant. In REN1, the conserved arginine of the GAP domain was required for REN1 activity towards ROP1. Mutation of the conserved catalytic arginine in GFP-PHGAPs (*pUBN:GFP-PHGAP1*^{R203L} and *pUBN:GFP-PHGAP2*^{R198L}, Figure 1a) did not alter their cell cycle dependent localization at the CDZ/CDS, indicating that GAP activity was not required for CDZ/CDS localization (Figure S4g, S4h). Furthermore, defects in root growth, cell wall positions and mitotic microtubule array orientation were similar to *phgap1 phgap2* suggesting that a functional GAP domain was required for accurate cell wall positioning (Figure S4d, S4e, S4f, S4i).

Our results suggest that PHGAPs and POK1 most likely act in a feedback loop, where PHGAPs act upstream of division plane selection and subsequent POK1 localization at the CDZ, but still require POK activity for their localized enrichment at the CDZ/CDS during mitosis. Loss of PHGAP activity leads to cell division phenotypes, that are modest compared to *pok1-1 pok2-3* double mutants (Figure 3c and S4b). However, knock-down of *Arabidopsis TAN* also causes mild cell wall miss-positioning in the root meristem [2], comparable to *phgap1 phgap2*. Similarly to *tan*, *PHGAP2* transcripts are not fully abolished in the *phgap2* allele and residual PHGAP2 activity might be present in most tissues. Furthermore, gene expression patterns of *PHGAP1* and *PHGAP2* are overlapping, but not identical in root meristematic tissue (Figure S3n, S3o) and unresolved redundant functions with CRIB domain containing RhoGAP proteins are likely [17,18]. In fact, functional redundancy of REN1 and ROPGAP1 has been reported in the case of in *Arabidopsis* pollen tube growth [19].

The potential interaction of PHGAPs and ROPs (Figure 1), together with the requirement of the catalytic arginine for PHGAP function (Figure S4) suggest, that PHGAPs act as genuine ROP GTPase activating proteins. Thus, we propose that loss of *PHGAP1* and *PHGAP2* likely leads to localized, subcellular imbalance of ROP activities. Indeed, down-regulation or loss of ROP3 affects early embryo development [20], resembling the *phgap1 phgap2* embryo phenotype.

However, the localization of PHGAPs at the CDZ/CDS is not affected by the arginine mutation (Figure S4g, S4h), indicating that the localization of PHGAPs at the CDZ/CDS *per se* is independent of its GAP function. Likely, the POK dependent localization of PHGAPs at the

CDZ/CDS is mediated by PHGAPs C-terminal domains and independent of GAP function. The interaction with the CDZ/CDS master-organizer POK1 and PHGAPs localization at the CDZ/CDS might indicate a localized down-regulation of ROP activities at the CDZ which could affect cytoskeletal organization and vesicle trafficking.

Our findings, that a pair of Rop-GAPs are necessary for accurate division plane selection and subsequent division plane establishment via POK1, might reflect the requirement for precautious spatio-temporal control over ROP activity and its downstream effects on cytoskeletal organization during cell division.

Methods

More information is provided in Supplemental Information.

Confocal Microscopy

Fluorescence was recorded using the Leica TCS SP8 equipped with resonant scanner with a 63x, NA = 1.20, water immersion objective lens or a 20x, NA = 0.75, water immersion objective lens. GFP fluorescence was excited with a 488-nm laser line from an argon/krypton laser and detected with a hybrid detector (HyD) set to 500 to 550 nm detection window. YFP excitation by the 514-nm laser line from an argon/krypton laser was detected between 520 and 550 nm with a HyD detector. RFP and Propidium Iodide, respectively, were excited with a 561-nm He/Ne laser, and fluorescence was detected with a HyD detector or standard PMT detector set at 570 to 650 nm.

Two-dimensional projections and three-dimensional reconstructions of Z stacks were generated with either Fiji (http://rsb.info.nih.gov/ij/) or Leica LF Image processing. Color merges were carried out with Adobe Photoshop CS5 v12.0.4 (Adobe Systems). Only linear adjustments to pixel values were applied. Figures were assembled in Adobe IllustratorCS5 v15.0.2.

Interaction studies using ratiometric Bimolecular Fluorescence Complementation (rBiFC)

Imaging of the protoplasts was carried out at least 22 h after transfection. For comparison of interaction strength rBiFC, identical confocal settings were used for respective experiments. YFP and RFP confocal images of individual transfected protoplasts were recorded. RFP is expressed from the same plasmid as the n-YFP and c-YFP fusion pairs. Image acquisition and quantification was performed as previously described [4]. YFP signal was selected with the segmented line tool in ImageJ 1.44, set to a width of 3 pixel. Average Fluorescence signal intensity was measured for YFP and RFP in the selected region. Calculation of mean YFP/RFP ratios were performed in Excel. Each protoplast represents an independent transformation event. Box plot was assembled in MATLAB.We also attempted to analyze PHGAP1 interactions with POK1-Cterminus and ROPs using BiFC, however, in no instance we observed fluorophore complementation.

Analysis of embryo development

Embryos were fixed in methanol:acetic acid (3:1) and cleared in chloral-hydrate, according to [14], and visualized using DIC optics with a Zeiss Axiophot microscope.

Quantification of microtubule array orientation and YFP-POK1 orientation.

For preprophase band and phragmoplast orientation we performed immuno-localization and measured intact root meristems. In case of YFP-POK1 we used life samples. We collected image stacks of root meristems at 2µm z-intervals. The longitudinal (main) axis of the root was determined and selected as a region of interest (ROI) using Imagej 1.50g (Fiji). The angle (α) between preprophase band, phragmoplast or YFP-POK1 and the main axis was determined in Fiji. The deviation from the expected transverse orientation (perpendicular, at 90 ° relative to the longitudinal main axis) was calculated. If $\alpha > 90°$, we calculated the deviation angle = α-90°, in case $\alpha < 90°$ we calculated the deviation angle = 90°-α. Thus, all deviation angle values were positive. We used BoxPlotR (http://boxplot.tyerslab.com/) to create boxplots depicting the mean deviation angle (plus) and the 95% confidence interval of the mean (grey bar flanking the mean). Altman Whiskers extend to 5th and 95th percentile. Significance was determined using one way ANOVA with post-hoc Turkey HSD. Number of analyzed roots was $\geq 6 \geq 12$. Using Excel, deviation angles were sorted into bins as indicated and the frequencies of angles in each bin were depicted in a bar chart. Significance of distribution was determined using Mann-Whitney U test.

Author contribution

We describe contributions to the paper using the CRediT taxonomy. Writing – Original Draft: S.M., D. S., A.H.; Writing – Review & Editing: S.M.; Conceptualization: D.S., S.M.; Investigation: D.S., A.H., E.L., T.L.,; Methodology: S.M.; Formal Analysis: D.S., A.H., E.L. and S.M.; Funding Acquisition: S.M.

Acknowledgements

We thank Dr. Manoj Singh for helpful discussion and Dr. Christopher Grefen for discussion and reagents. We thank anonymous reviewers for their constructive comments. Funding was provided by the Deutsche Forschungsgemeinschaft (DFG, grants MU3133/3-1 and SFB1101).

References

1 Yang, Z. Cell polarity signaling in Arabidopsis. *Annu Rev Cell Dev Biol* **24**, 551-575, doi:10.1146/annurev.cellbio.23.090506.123233 (2008).

2 Walker, K. L., Muller, S., Moss, D., Ehrhardt, D. W. & Smith, L. G. Arabidopsis TANGLED identifies the division plane throughout mitosis and cytokinesis. *Curr Biol* **17**, 1827-1836, doi:S0960-9822(07)02078-7 [pii]10.1016/j.cub.2007.09.063 (2007).

3 Xu, X. M. *et al.* RanGAP1 is a continuous marker of the Arabidopsis cell division plane. *Proc Natl Acad Sci U S A* **105**, 18637-18642, doi:0806157105 [pii]10.1073/pnas.0806157105 (2008).

4 Lipka, E. *et al.* The Phragmoplast-Orienting Kinesin-12 Class Proteins Translate the Positional Information of the Preprophase Band to Establish the Cortical Division Zone in Arabidopsis thaliana. *Plant Cell* **26**, 2617-2632, doi:10.1105/tpc.114.124933 (2014).
5 Cherfils, J. & Zeghouf, M. Regulation of Small GTPases by GEFs, GAPs, and GDIs. *Physiological Reviews* **93**, 269-309, doi:10.1152/physrev.00003.2012 (2013).
6 Craddock, C., Lavagi, I. & Yang, Z. New insights into Rho signaling from plant ROP/Rac GTPases. *Trends in Cell Biology* **22**, 492-501, doi:http://dx.doi.org/10.1016/j.tcb.2012.05.002 (2012).
7 Oda, Y. & Fukuda, H. Initiation of cell wall pattern by a Rho- and microtubule-driven symmetry breaking. *Science* **337**, 1333-1336, doi:10.1126/science.1222597 (2012).
8 Oda, Y. & Fukuda, H. Rho of plant GTPase signaling regulates the behavior of Arabidopsis kinesin-13A to establish secondary cell wall patterns. *Plant Cell* **25**, 4439-4450, doi:10.1105/tpc.113.117853 (2013).
9 Facette, M. R. *et al.* The SCAR/WAVE complex polarizes PAN receptors and promotes division asymmetry in maize. *Nature Plants* **1**, 14024, doi:10.1038/nplants.2014.24 (2015).
10 Guilluy, C., Garcia-Mata, R. & Burridge, K. Rho protein crosstalk: another social network? *Trends in Cell Biology* **21**, 718-726, doi:http://dx.doi.org/10.1016/j.tcb.2011.08.002 (2011).
11 Zuo, Y., Oh, W. & Frost, J. A. Controlling the switches: Rho GTPase regulation during animal cell mitosis. *Cellular signalling* **26**, 2998-3006, doi:http://dx.doi.org/10.1016/j.cellsig.2014.09.022 (2014).
12 Hwang, J. U., Vernoud, V., Szumlanski, A., Nielsen, E. & Yang, Z. A tip-localized RhoGAP controls cell polarity by globally inhibiting Rho GTPase at the cell apex. *Curr Biol* **18**, 1907-1916, doi:10.1016/j.cub.2008.11.057 (2008).
13 Karnik, R. *et al.* Binding of SEC11 Indicates Its Role in SNARE Recycling after Vesicle Fusion and Identifies Two Pathways for Vesicular Traffic to the Plasma Membrane. *The Plant Cell* **27**, 675-694, doi:10.1105/tpc.114.134429 (2015).
14 Muller, S., Han, S. & Smith, L. G. Two kinesins are involved in the spatial control of cytokinesis in Arabidopsis thaliana. *Curr Biol* **16**, 888-894, doi:S0960-9822(06)01331-5 [pii] 10.1016/j.cub.2006.03.034 (2006).
15 Grefen, C. & Blatt, M. R. A 2in1 cloning system enables ratiometric bimolecular fluorescence complementation (rBiFC). *Biotechniques* **53**, 311-314, doi:Doi 10.2144/000113941 (2012).
16 Yoshida, S. *et al.* Genetic control of plant development by overriding a geometric division rule. *Dev Cell* **29**, 75-87, doi:10.1016/j.devcel.2014.02.002 (2014).
17 Schaefer, A., Miertzschke, M., Berken, A. & Wittinghofer, A. Dimeric Plant RhoGAPs Are Regulated by Its CRIB Effector Motif to Stimulate a Sequential GTP Hydrolysis. *Journal of Molecular Biology* **411**, 808-822, doi:10.1016/j.jmb.2011.06.033 (2011).
18 Mucha, E., Fricke, I., Schaefer, A., Wittinghofer, A. & Berken, A. Rho proteins of plants – Functional cycle and regulation of cytoskeletal dynamics. *European Journal of Cell Biology* **90**, 934-943, doi:10.1016/j.ejcb.2010.11.009 (2011).
19 Hwang, J. U. *et al.* Pollen-tube tip growth requires a balance of lateral propagation and global inhibition of Rho-family GTPase activity. *J Cell Sci* **123**, 340-350, doi:10.1242/jcs.039180 (2010).
20 Huang, J. B. *et al.* ROP3 GTPase Contributes to Polar Auxin Transport and Auxin Responses and Is Important for Embryogenesis and Seedling Growth in Arabidopsis. *Plant Cell* **26**, 3501-3518, doi:10.1105/tpc.114.127902 (2014).

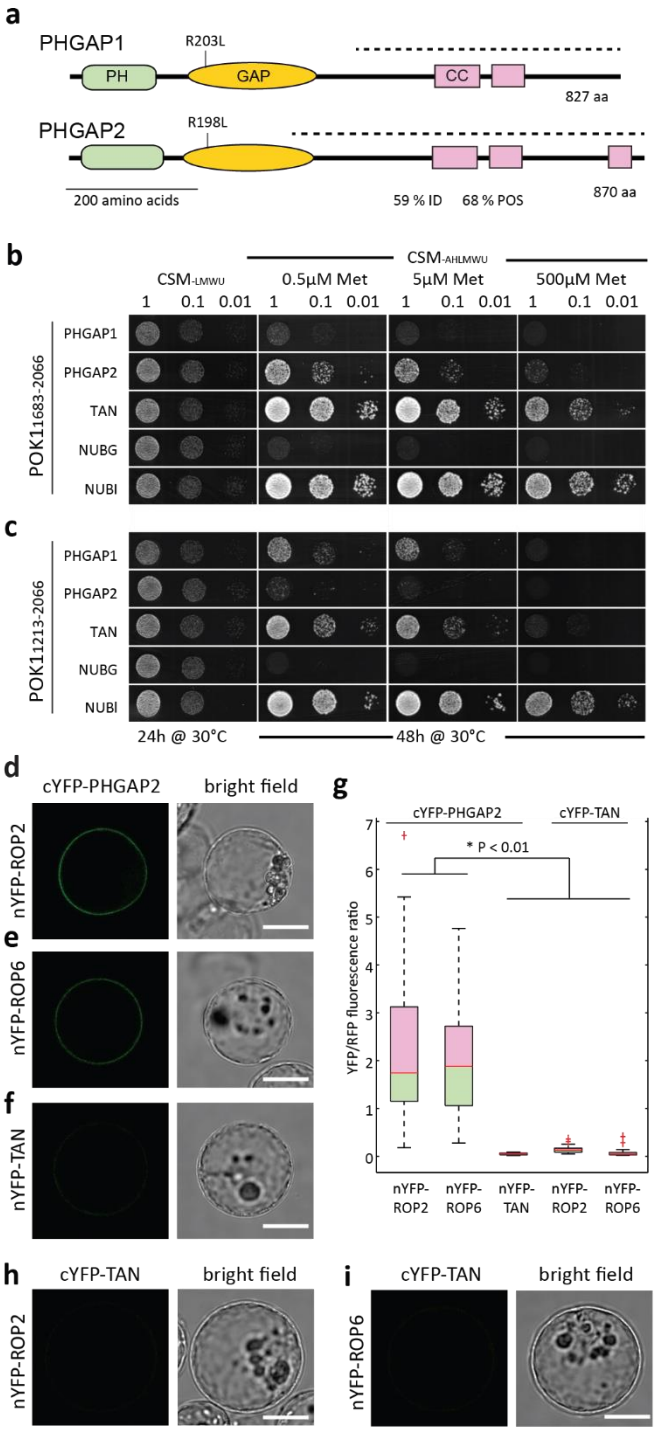
a
PHGAP1
R203L
PH
GAP
CC
827 aa
PHGAP2
R198L
200 amino acids
59 % ID
68 % POS
870 aa
b
CSM-LMWU
CSM-AHLMWU
0.5µM Met
5µM Met
500µM Met
1 0.1 0.01
POK1 1683-2066
PHGAP1
PHGAP2
TAN
NUBG
NUBI
c
POK1 1213-2066
24h @ 30°C
48h @ 30°C
d
cYFP-PHGAP2
bright field
nYFP-ROP2
e
nYFP-ROP6
f
nYFP-TAN
g
cYFP-PHGAP2
cYFP-TAN
* P < 0.01
YFP/RFP fluorescence ratio
nYFP-ROP2
nYFP-ROP6
nYFP-TAN
h
cYFP-TAN
bright field
nYFP-ROP2
i
cYFP-TAN
bright field
nYFP-ROP6

Figure 1: Organization of PHGAP protein domains and protein interaction assays. (a) PHGAP1 and PHGAP2 contain Pleckstrin homology (PH), GTPase activating protein (GAP) domains and coiled coil domains (CC, predicted by Paircoil, http://paircoil2.csail.mit.edu). The dashed lines indicate the shortest identified PHGAP clones found to interact with $POK1_{1213-2066}$ C-terminus in the initial yeast-two-hybrid experiment. PHGAP1 and PHGAP2 share 59% overall amino acid identity and 68% identical charge. (b and c) Yeast mating-based Split-Ubiquitin Cyto-SUS assay was performed with PHGAP1 and PHGAP2 with either (**b**) OST-$POK1_{1683-2066}$-Cub or (c) OST-$POK1_{1213-2066}$-Cub as baits. Yeast diploids were created with NubG-PHGAPx fusion construct together with controls (TAN, biological positive; NubG, negative; Nubl [wild type], positive) and spotted (left to right) on CSM- Leu-, Met-, Trp-, Ura- (CSM-LMWU) medium to verify mating, and on CSM-Ade-, His-, Leu-, Met-, Trp-, Ura- (AHLMWU) with the addition of different methionine concentrations to assay for interaction. Diploid yeast was dropped at 1.0, 0.1 and 0.001 OD_{600} in each case. Differences in interaction efficiency might be due to the heterologous system used for the assay and might not be biologically relevant. (d to i) Ratiometric bimolecular fluorescence complementation (rBiFC) analysis of interaction between PHGAP2 and (d) ROP2 and (e) ROP6 assayed in *Arabidopsis thaliana* protoplasts. Images show single optical sections of n/cYFP fluorescence and corresponding bright field. (f-h) TANGLED (TAN) was tested for interaction with (f) PHGAP2, (h) ROP2 and (i) ROP6 as a biological negative control. (g) Box plot of YFP/RFP fluorescence ratios for protein pairs as indicated. For each protein pair were imaged and n/cYFP fluorescence and co-expressed cytosolic RFP serving as an internal control (see Figure S1e-S1i) were recorded. Mean n/cYFP and RFP fluorescence intensities were determined and ratioed for each protoplast. No or less efficient interaction results in low YFP/RFP ration, while efficient n/cYFP complementation due to protein interaction, results in elevated YFP/RFP ratios. Significant differences (*$P<0.01$) were determined by One Way Anova ($n \geq 24$ protoplasts). Scale bars indicate 10 µm.

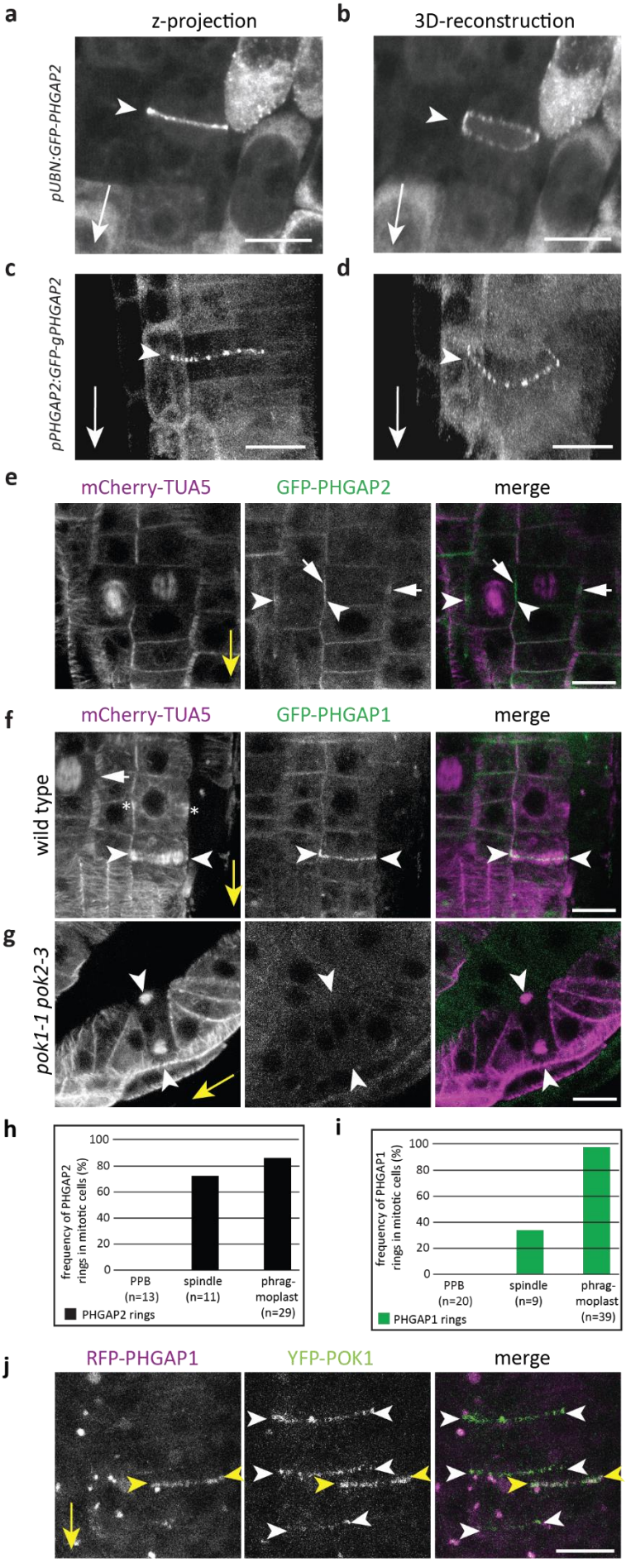
a
z-projection
b
3D-reconstruction
pUBN:GFP-PHGAP2
c
d
pPHGAP2:GFP-gPHGAP2
e
mCherry-TUA5
GFP-PHGAP2
merge
f
mCherry-TUA5
GFP-PHGAP1
merge
wild type
g
pok1-1 pok2-3
h
frequency of PHGAP2 rings in mitotic cells (%)
100
80
60
40
20
0
PPB (n=13)
spindle (n=11)
phrag-moplast (n=29)
PHGAP2 rings
i
frequency of PHGAP1 rings in mitotic cells (%)
100
80
60
40
20
0
PPB (n=20)
spindle (n=9)
phrag-moplast (n=39)
PHGAP1 rings
j
RFP-PHGAP1
YFP-POK1
merge

Figure 2: PHGAP accumulation at the cortical division zone is cell cycle- and POK-dependent. (a, b) Root meristem cells expressing *pUBN:GFP-PHGAP2.* (a) Arrowhead points to the distinct GFP-PHGAP2 localization, which represents the face view of a ring-shaped pattern, apparent in the 3-D reconstruction shown in (b, arrowhead). (c, d) Root meristem cells expressing *pPHGAP2:GFP-gPHGAP2.* (c) Arrowhead points to the distinct GFP-PHGAP2 localization, which represents the face view of a ring-shaped pattern, apparent in the 3-D reconstruction shown in (d, arrowhead). (e) Root meristem expressing *pUBN:GFP-PHGAP2* and the microtubule reporter construct *35S:mCherry-TUA5*. In cross sections, PHGAP2 is visible as lateral accumulations in cells with spindles (arrows) and phragmoplasts (arrow heads). (f) Root meristem expressing *pUBN:GFP-PHGAP1* and *35S:mCherry-TUA5*. Cells displaying PPB (arrows), spindle (asterisk) and phragmoplast (arrow heads). Cytokinetic cell (arrow heads) exhibits prominent GFP-PHGAP1 ring (arrow heads). (g) Root meristem of *pok1-1 pok2-3*. Note the absence of GFP-PHGAP1 from the cortical division site (arrow heads). Yellow arrows indicate the orientation of the root axis. (h, i) Correlation of PHGAP accumulation in a ring with cell cycle stage. (h) While prophase cells with preprophase bands (PPBs, n=13) do not show discernable rings, 73 % of cells with spindles (n=11) and 86 % of cells with phragmoplasts (n=29) show PHGAP2 rings. (i) Prophase cells with preprophase bands (PPBs, n=20) do not show discernable PHGAP1 rings, while 33 % of cells with spindles (n=9) and 97 % of cells with phragmoplasts (n=39) show PHGAP1 rings. In contrast, mitotic cells in the *pok1-1 pok2-3* double mutant never exhibit PHGAP1 rings. (j) Cells express *pPOK1:YFP-POK1* [4] and *p35S:RFP-PHGAP1*. Co-localization of YFP-POK1 and RFP-PHGAP1 (yellow arrow head) in root meristem. Note that some cells exhibit YFP-POK1 only (white arrow heads). Arrow heads indicate the cortical division site. Yellow arrows represent the long axis of the root. All images are z-projections of image stacks. Scale bars indicate 10 µm. See also Figure S2.

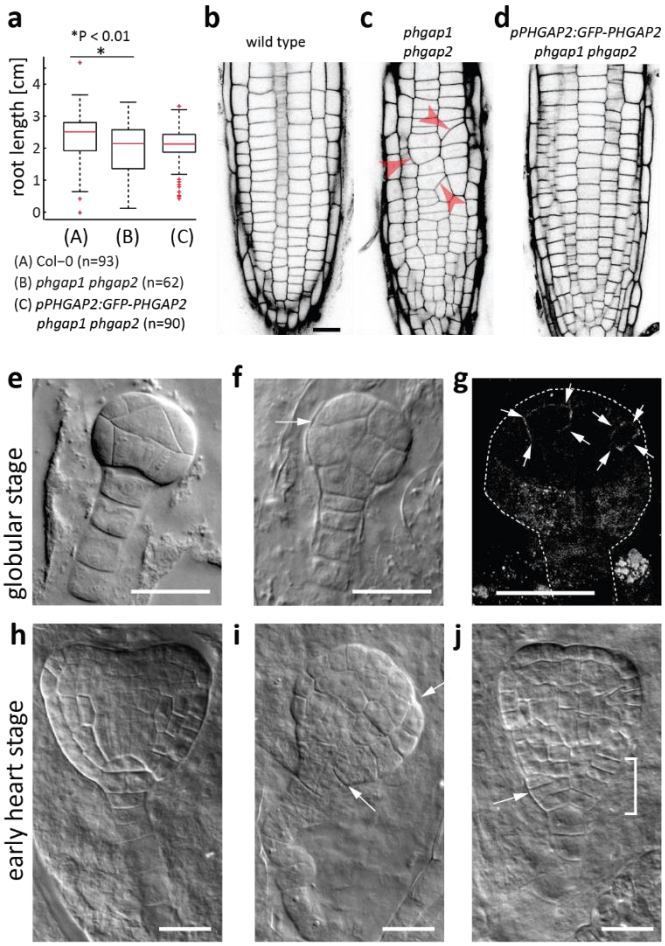

Figure 3: Phenotype analysis of *phgap1 phgap2* mutants compared to wild type. (a) Box plot comparing primary root length of wild type (A, Col-0, mean 2.5 cm ± 0.8 STD), (B) *phgap1 phgap2* double mutant (mean 2.1 cm ± 0.8 STD and (C) complementation line, expressing *pPHGAP2:GFP-PHGAP2* in the *phgap1 phgap2* double mutant (mean 2.3 cm ± 0.5 STD). Col-0 and *phgap1 phgap2* are significantly different (P< 0.01) (n = number of roots analyzed for each genotype. (b to d) Single confocal images of Propidium iodide stained primary root meristems visualizing cell wall patterns. (b) Wild type (Col-0), (c) *phgap1 phgap2* (d) complementation line *pPHGAP2:GFP-PHGAP2 phgap1 phgap2.* (e, f, h-j) DIC images of cleared embryos. **e,h** Wild type embryos display the typical regular, cellular pattern. (f, I, j) *phgap1 phgap2* embryos show abnormal cell pattern (brackets) and irregular positioned cell walls (arrows). (g) 3D reconstruction of globular stage embryo of complementation line expressing *pPHGAP2:GFP-PHGAP2 in phgap1 phgap2.* Arrows point to continuous ring-shaped GFP-PHGAP2 pattern. Dashed line indicates outline of embryo. Scale bars indicate 20 µm in all images.

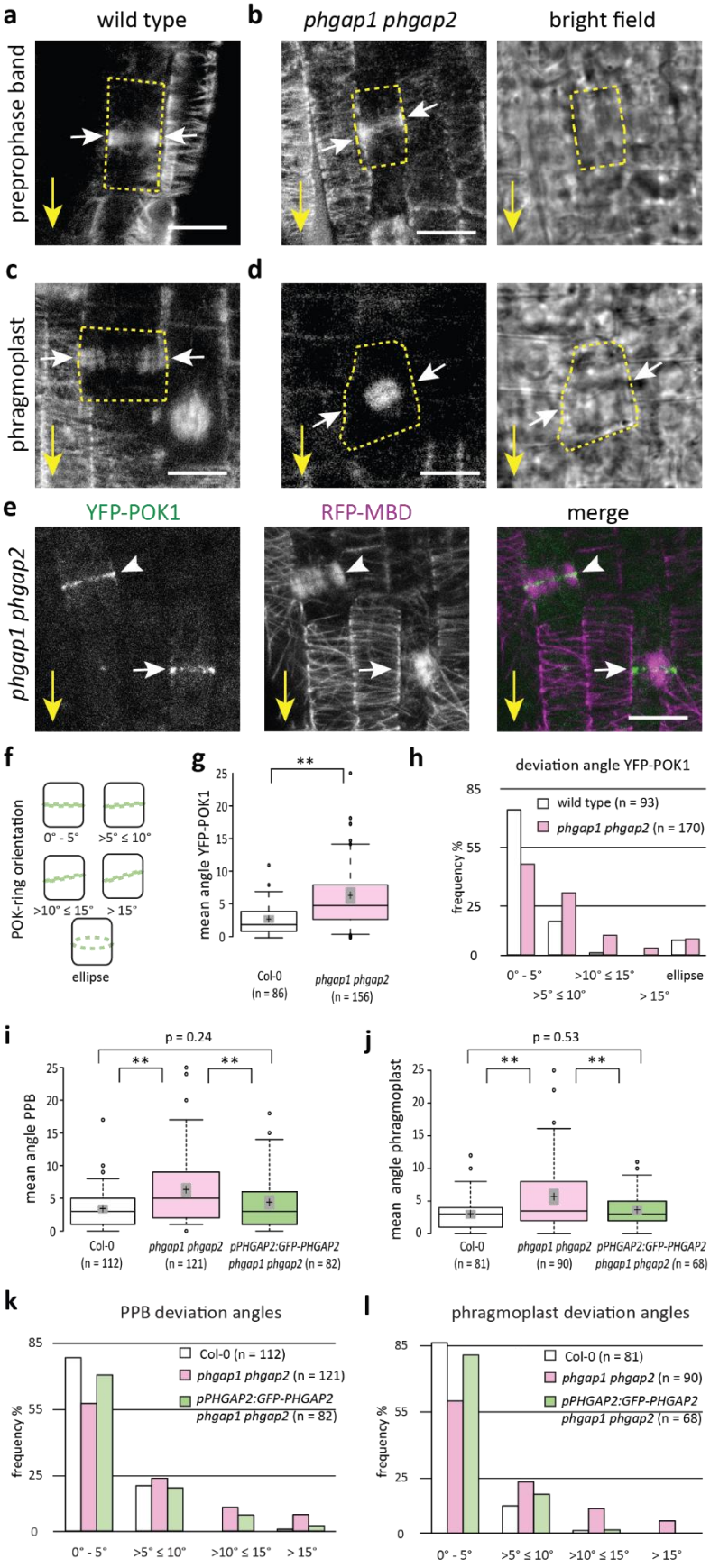
a
wild type
b
phgap1 phgap2
bright field
preprophase band
c
d
phragmoplast
e
YFP-POK1
RFP-MBD
merge
phgap1 phgap2
f
POK-ring orientation
0° - 5°
>5° ≤ 10°
>10° ≤ 15°
> 15°
ellipse
g
mean angle YFP-POK1
**
Col-0 (n = 86)
phgap1 phgap2 (n = 156)
h
deviation angle YFP-POK1
wild type (n = 93)
phgap1 phgap2 (n = 170)
frequency %
i
p = 0.24
mean angle PPB
Col-0 (n = 112)
phgap1 phgap2 (n = 121)
pPHGAP2:GFP-PHGAP2 phgap1 phgap2 (n = 82)
j
p = 0.53
mean angle phragmoplast
Col-0 (n = 81)
phgap1 phgap2 (n = 90)
pPHGAP2:GFP-PHGAP2 phgap1 phgap2 (n = 68)
k
PPB deviation angles
Col-0 (n = 112)
phgap1 phgap2 (n = 121)
pPHGAP2:GFP-PHGAP2 phgap1 phgap2 (n = 82)
l
phragmoplast deviation angles
Col-0 (n = 81)
phgap1 phgap2 (n = 90)
pPHGAP2:GFP-PHGAP2 phgap1 phgap2 (n = 68)

Figure 4: Mitotic microtubule array orientation and POK1-ring position. Microtubules are visualized using RFP-MBD. (a) and (b) prophase. (a) Transverse preprophase band (PPB, arrows) in wild type. (b) Oblique PPB (arrows) in *phgap1 phgap2*. (c) Transverse phragmoplast in wild type (arrows) and (d) obliquely expanding phragmoplast (arrows) and cell plate (arrow, bright field) in *phgap1 phgap2* cytokinesis. Dashed lines mark cell outlines. (e) Transverse (arrow) and obliquely (arrow head) oriented POK1 signal in *phgap1 phgap2*cytokinesis. Yellow arrows indicate longitudinal root axis. Images are z-projections or single images. Scale bars indicate 10 µm.
(f) Schematic of observed POK1-ring orientation. Deviation from the transverse (0° - 5°) were sorted into angle classes (>5° - ≤ 10°, >10° - ≤ 15°, >15°, ellipse). (g) Boxplot of YFP-POK1 orientation. Mean deviation angle (indicted by +, grey bar indicates the 95% confidence interval for the mean) of POK1 in wild type and in *phgap1 phgap2* differ significantly (** $p<0.01$ one-way ANOVA, post-hoc Turkey HSD). (h) Frequencies of different POK1-ring orientations in wild type (white bars) and *phgap1 phgap2* (pink bars). Distributions are significantly different from each other (Mann-Whitney U test, $p<0.01$). (i and j) Boxplots. Mean deviation angle is indicted by (+, grey bar indicates 95% confidence interval. (h) Deviation angle of PPBs, (i) deviation angle of phragmoplasts. Significant differences (** $p<0.01$, one-way ANOVA, post-hoc Turkey HSD) are indicated. P-values for PPBs versus phragmoplast of the same genotype were non-significant; Col-0 PPB versus phragmoplast P = 0.31; *phgap1 phgap2* PPB versus phragmoplast P = 0.41; *pPHGAP2:GFP-PHGAP2 phgap1 phgap2* PPB versus phragmoplast P = 0.21. (k and l) Frequencies of different PPB and phragmoplast orientations. Col-0 (white, *phgap1 phgap2* (pink); rescue line *pPHGAP2:GFP-PHGAP2 phgap1 phgap2* (green). Distributions in Col-0 and *phgap1 phgap2* and distributions in *phgap1 phgap2* and rescue line are significantly different (Mann-Whitney U test, $p<0.01$). Col-0 and rescue are non-significant ($p = 0.28$ for PPBs, $p = 0.11$ for phragmoplasts).

Supplemental Information:

Putative RopGAPs impact division plane selection and interact with kinesin-12 POK1

Plant Growth

For analysis of mutant phenotypes, localization studies, crosses and reproduction, seeds were surface sterilized and placed on ½ MS medium (Murashige and Skoog medium) followed by stratification at 4°C in the dark for at least two days. Then plants were grown in growth chambers under long day conditions (cycling 16 h light / 8 h dark) at 19°C to 22°C. For further experimentation and propagation two to three week old seedlings were transferred to soil.

In this study *Arabidopsis thaliana* plants, ecotype Columbia (Col-0, wild type) were used. For mutant analysis of *PHGAP* genes, T-DNA insertion lines *phgap1-1* (WiscDsLoxHs135_04D) and *phgap2-1* (SALK_083351) were obtained from the Arabidopsis biological resource center (ABRC, Ohio, US) and Nottingham Arabidopsis stock center (NASC, Nottingham, UK) [5]. All other transgenic lines in this study were created by *Agrobacterium tumefaciens* (*A. tumefaciens*) mediated transformation of respective plasmids into Col-0 [6].

For examination of the microtubule cytoskeleton the previously described microtubule reporter line *p35S:GFP-MBD* [7] was used.

Generation of fluorescent fusion proteins

For localization studies cDNA of *PHGAP1* and *PHGAP2* was reverse transcribed from RNA isolated from seedlings or flower buds and cloned into Gateway® compatible pENTR vectors. In addition, for *PHGAP2* a pENTR clone (G21877) was obtained from the ABRC [8]. *pENTR-PHGAP1* and *pENTR-PHGAP2* were subsequently recombined with destination vectors *pUBN:GFP* and *pUBN:RFP* [9] using LR clonase. Stable plant transformation was mediated by the *A. tumefaciens* strain GV3101. Transformants were selected on nutrient agar plates containing 0.05% phosphinotricin (Duchefa) or by spraying plants with 0.1% Basta (Bayer) respectively. Three independent *pUBN:GFP-PHGAP1* and ten independent *pUBN:GFP-PHGAP2* T1 lines were selected and propagated for further analysis. Analysis of localization patterns was performed using confocal microscopy in the T2 generation. All lines showed comparable localization pattern and fluorescence intensity. For co-localization studies selected lines expressing RFP-PHGAP1 were crossed with YFP-POK1 lines previously characterized in [1].

Investigation of the respective GAP domains in PHGAP1 and PHGAP2 was carried out by substitution of a highly conserved catalytic arginine residue within the GAP domain by leucin. As previously shown a conserved arginine in the GAP-domain is essential for GAP activity [10] . The respective residues in PHGAP1 (R203L) and PHGAP2 (R198L) were mutated to leucine by site directed mutagenesis using miss-match primers (Table S2) in a rolling cycle PCR

reaction and *pENTR cPHGAP1* and *pENTR cPHGAP2* as respective templates. (Table S2). Resulting mutants *pENTR cPHGAP1*^{R203L} and *pENTR cPHGAP2*^{R198L} were recombined to obtain *pUBN:GFP-PHGAP1* ^{R203L} (five independent T1 lines) and *pUBN:GFP-PHGAP2* ^{R198L} (seven independent T1 lines).

Interaction studies using ratiometric Bimolecular Fluorescence Complementation (rBiFC)

The Gateway compatible 2 in 1 system [11] was used to test putative interactions of PHGAP2 and POK1$_{1683-2066}$ as well as PHGAP2 and selected ROPs. Negative controls are indicated in figure legends. In brief, potential interaction partners were fused to either nYFP or cYFP on the same plasmid, each expressed und the control of a 35S promoter. In addition the plasmid include an internal expression control (p35S:RFP). Interaction strength was determined by the YFP/RFP ratio. Amplicons (primers listed in table 1) with appropriate recombination sites were cloned into either pDONOR221-P3P2 or pDONOR221-P1P4 by BP clonase, also described previously in [1]. Subsequent LR clonase reaction was performed with the pBiFCt-2in1-NN destination vector.

Polyethylene glycol (PEG) mediated transfections of plasmids into *A. thaliana* root cell protoplasts were carried out by the transformation unit of the ZMBP as described previously [1].

Mating-Based Cyto-SUS Assays

POK1$_{1213-2066}$ and POK1$_{1683-2066}$ coding sequences without stop codon were amplified from entry clones described by [1] and cloned into pENTR2B via BamHI/XhoI and into pENTR3C via EcoRI/XhoI. In a single Gateway LR reaction each ENTR clone was cloned into the OST-Cub destination vector [12], whereas cTAN [1], cGAP1 and cGAP2 with stop codon were cloned into the pNX35-Dest Destination vector [13]. The haploid yeast strains THY.AP4 and THY.AP5) [14] were transformed according to [15] and plated on selective media (CSM-Leu, Met (LM) for THY.AP4 and CSM-Met, Tyr, Ura (MTU) for THY.AP5. For liquid cultures 10 to 15 yeast colonies were selected and inoculated for overnight growth at 180 rpm and 28°C. Yeast mating was performed in sterile PCR tubes after harvesting and re-suspending of liquid cultures in YPD medium. Equal aliquots of cultures containing either OST-POK1$_{1213-2066}$-Cub or OST-POK1$_{1683-2066}$-Cub in THY.AP4 with the appropriate NubG-X in THY.AP5 were mixed. Aliquots of 5 µL from each mixture were dropped on YPD plates and incubated at 28°C for at least 6h. Then colonies were transferred from YPD on CSM- Leu, Met, Trp, Ura (LMWU) plates and incubated at 28°C overnight. After 16h colonies were inoculated in 2 ml of liquid CSM-LMWU media and grown at 180 rpm and 28°C overnight. 100µl of each mating combination were harvested and re-suspended in sterile water. Serial dilutions of 7µl per spot at OD600 1.0, 0.1 and 0.01 were dropped on CSM- Ade, His, Leu, Met, Trp, Ura (AHLMWU) plates with added methionine in increasing concentrations (0.5, 5, 50 and 500 µM) and on a CSM– LMWU control

plate to confirm mating efficiency. Plates were incubated at 28°C and images were taken after 24h for CSM – LMWU control plate and 48h for CSM-AHLMWU plates.

Immuno-localization

Immunofluorescence staining was essentially performed as previously described [16]. In brief, seven-day-old seedlings were fixed in 4% paraformaldehyde/microtubule-stabilizing buffer (MTSB, 50 mM Pipes, 5 mM EGTA, 5 mM MgSO4, pH 7.0) and washed three times in water. Seedlings were subsequently placed on charged slides (Thermo Scientific), protected with coverslips dipped in liquid nitrogen. Coverslips were removed and samples dried overnight. Seedlings were rehydrated in MTSB for 5 min before cell walls were partially digested with 2% driselase (Sigma-Aldrich) in MTSB for 1 h at 37°C. After three times of washing with phosphate buffered saline (PBS, 137 mM NaCl, 2.7 mM KCl, 10 mM Na2HPO4, 2 mM KH2PO4, pH 7.4), the plasma membrane was permeabilized with 3% Nonident P40 in 10% DMSO-MTSB for 1 h at 37°C followed again by washing six times with PBS. Samples were blocked in 5% bovine serum albumin (Sigma)/PBS overnight at 4° C Primary antibodies rat-anti-tubulin 1:600 (YL1/2, Abcam, 1:600) and rabbit-anti-GFP (Invitrogen, 1:1000) and secondary antibodies goat-anti-rabbit Alexa 488 (Invitrogen, 1:600) and goat-anti-rat Cy3 (Dianova, 1:600) in 5% BSA/PBS, were used. Primary and secondary antibodies were incubated at 37°C for 3h each and subsequently washed 3 times with PBS. DNA was stained with 4',6-diamidino-2-phenylindole (DAPI; 1:1000) for 15 min at room temperature. Samples were mounted in Citifluor (Amersham). Imaging was performed on Leica TCS SP8 with appropriate settings.

Table S1: Oligonucleotides used for cloning

cDNA cloning	
PH-GAP1 ATG_F	GGTACCATGGAGGCTTCTCTAGCTGTTA
PH-GAP1 Stop_R	GCGGCCGCCTAATTCCATGGTGGAGAAGA
PH-GAP2-ATG_F	GGATCCATGGAGGCTTCTTTAGCGGCTTT
PH-GAP2 Stop_R	GCGGCCGCTTAGTTCCAAGGTGGAGATGAT
promotor cloning	
PH-GAP1 1.5 kb pro_F	CTGCAGAGAGACGGAAGTGAGTTGCTGACTT
PH-GAP1 1.5 kb pro_R	CTGCAGTGCAGAAGTACACACTTAATC
proPHGAP2_Not_R	GCGGCCGCTGCCTCAACAGCATAATCTCCAGAT
proPHGAP2-2R	CTGCAGAAAGAAGCCTCCATTGCCTCAACA
GAP mutation	
PHGAP1 R198L_F	AGGGATATTACTGCAGTCTGCTGAT
PHGAP1 R198L_R	ATCAGCAGACTGCAGTAATATCCCT
PHGAP2 R203L_F	AGGAATTTTACTGCAGTCTGCAGATGT
PHGAP2 R203L_R	ACATCTGCAGACTGCAGTAAAATTCCT
rBiFC cloning	
attB3 POK1C-short _F	GGGGACAACTTTGTATAATAAAGTTGTAATGGATGAAG AAGTAAAAAGGCATCGT

attB2 POK1C-short_R	GGGGACCACTTTGTACAAGAAAGCTGGGTTTTACCGATATCTTGTACCAGAGCT
attB3 TAN1_F	GGGGACAACTTTGTATAATAAAGTTGTAATGGTTGCAAGAACCCCACAGAAGCA
attB2 TAN1_R	GGGGACCACTTTGTACAAGAAAGCTGGGTTCTACACTTTCCTGCTCTTCATTGGA
attB1 PHGAP2_F	GGGGACAAGTTTGTACAAAAAAGCAGGCTTAATGGAGGCTTCTTTAGCGGCTTT
attB4 PHGAP2_R	GGGGACAACTTTGTATAGAAAAGTTGGGTGTTAGTTCCAAGGTGGAGATGATG
attB4 TAN_r	GGGG AC AAC TTT GTA TAG AAA AGT TGG GTG CTACACTTTCCTGCTCTTCATTGGA
attB1 TAN	GGGG ACA AGT TTG TAC AAA AAA GCA GGC TTA ATGGTTGCAAGAACCCCACAGAAGCA
attB3 ROP4	GGGG ACA ACT TTG TAT AAT AAA GTT GTA ATGAGTGCTTCGAGGTTTATAAAGTGT
attB2 ROP4 r	GGGG AC CAC TTT GTA CAA GAA AGC TGG GTT TCACAAGAACACGCAGCGGTTCTT
attB3 ROP2	GGGG ACA ACT TTG TAT AAT AAA GTT GTA ATGGCGTCAAGGTTTATAAAGTGT
attB2 ROP2 r	GGGG AC CAC TTT GTA CAA GAA AGC TGG GTT TCACAAGAACGCGCAACGGTTCTT
attB3 ROP6	GGGG ACA ACT TTG TAT AAT AAA GTT GTA ATGAGTGCTTCAAGGTTTATCAAGT
attB2 ROP6 r	GGGG AC CAC TTT GTA CAA GAA AGC TGG GTT TCAGAGTATAGAACAACCTTTCTG
ROP1_attB2_R	GGGGACCACTTTGTACAAGAAAGCTGGGTTTCATAGAATGGAGCATGCCTTCT
ROP1_attB3_F	GGGG ACA ACT TTG TAT AAT AAA GTT GTAATGAGCGCTTCGAGGTTCGTAA
Split-Ubiquitin	
pAD-POK1-5047 EcoRI	GAATTCACCATGGATGAAGAAGTAAAAAGGCATCGTA
POK1C w/o STOP_XhoI	TACTCGAGTACCGATATCTTGTACCAGAGCTCT
genotyping	
PHGAP1_EcoRI-R	TCTTCAGGACTGAATTCTGTCTT
L4	TGATCCATGTAGATTTCCCGGACATGAAG
PHGAP2_ATG_F	GGATCCATGGAGGCTTCTTTAGCGGCTTT
PHGAP2_03R,	GGATCCATGGAGGCTTCTTTAGCGGCTTT
LBa1	TGGTTCACGTAGTGGGCCATCG
PH-GAP1_EcoR1-F	AGGCAAGACAGAATTCAGTCCTGAA
PH-GAP1 1506_R	TACTGGGAGTAACTGAGGGTATA
LBDs-Lox	AACGTCCGCAATGTGTTATTAAGTTGTC
PHGAP2 02_R	ATCTGCTCTCCAGCTTGTTGAT
PHGAP-g4913_F	TGCTGAAGCTGATGTCGCAAGGT
PHGAP1-01_R	ATACAGAGGCTCGAGCACATG
PHGPAP1-p954_F	ACTCTTATGTACACTACATCTA

References

1 Lipka, E. *et al.* The Phragmoplast-Orienting Kinesin-12 Class Proteins Translate the Positional Information of the Preprophase Band to Establish the Cortical Division Zone in Arabidopsis thaliana. *Plant Cell* **26**, 2617-2632, doi:10.1105/tpc.114.124933 (2014).

2 Muller, S., Han, S. & Smith, L. G. Two kinesins are involved in the spatial control of cytokinesis in Arabidopsis thaliana. *Curr Biol* **16**, 888-894, doi:S0960-9822(06)01331-5 [pii] 10.1016/j.cub.2006.03.034 (2006).

3 Blazquez, M. A., Soowal, L. N., Lee, I. & Weigel, D. LEAFY expression and flower initiation in Arabidopsis. *Development* **124**, 3835-3844 (1997).

4 Hauser, M. T. & Bauer, E. Histochemical analysis of root meristem activity in Arabidopsis thaliana using a cyclin : GUS (beta-glucuronidase) marker line. *Plant Soil* **226**, 1-10, doi:Doi 10.1023/A:1026421417979 (2000).

5 Alonso, J. M. *et al.* Genome-Wide Insertional Mutagenesis of Arabidopsis thaliana. *Science* **301**, 653-657, doi:10.1126/science.1086391 (2003).

6 Clough, S. J. & Bent, A. F. Floral dip: a simplified method forAgrobacterium-mediated transformation ofArabidopsis thaliana. *The Plant Journal* **16**, 735-743, doi:10.1046/j.1365-313x.1998.00343.x (1998).

7 Marc, J. *et al.* A GFP-MAP4 reporter gene for visualizing cortical microtubule rearrangements in living epidermal cells. *Plant Cell* **10**, 1927-1940 (1998).

8 Yamada, K. *et al.* Empirical Analysis of Transcriptional Activity in the Arabidopsis Genome. *Science* **302**, 842-846, doi:10.1126/science.1088305 (2003).

9 Grefen, C. *et al.* A ubiquitin-10 promoter-based vector set for fluorescent protein tagging facilitates temporal stability and native protein distribution in transient and stable expression studies. *Plant J* **64**, 355-365, doi:10.1111/j.1365-313X.2010.04322.x (2010).

10 Sermon, B. A., Lowe, P. N., Strom, M. & Eccleston, J. F. The Importance of Two Conserved Arginine Residues for Catalysis by the Ras GTPase-activating Protein, Neurofibromin. Journal of Biological Chemistry **273**, 9480-9485, doi:10.1074/jbc.273.16.9480 (1998).

11 Grefen, C. & Blatt, M. R. A 2in1 cloning system enables ratiometric bimolecular fluorescence complementation (rBiFC). *Biotechniques* **53**, 311-314, doi:Doi 10.2144/000113941 (2012).

12 Karnik, R. *et al.* Binding of SEC11 Indicates Its Role in SNARE Recycling after Vesicle Fusion and Identifies Two Pathways for Vesicular Traffic to the Plasma Membrane. *The Plant Cell* **27**, 675-694, doi:10.1105/tpc.114.134429 (2015).

13 Grefen, C. & Blatt, M. R. Do Calcineurin B-Like Proteins Interact Independently of the Serine Threonine Kinase CIPK23 with the K+ Channel AKT1? Lessons Learned from a Ménage à Trois. *Plant Physiology* **159**, 915-919, doi:10.1104/pp.112.198051 (2012).

14 Obrdlik, P. *et al.* K(+) channel interactions detected by a genetic system optimized for systematic studies of membrane protein interactions. *Proceedings of the National Academy of Sciences of the United States of America* **101**, 12242-12247, doi:10.1073/pnas.0404467101 (2004).

15 Grefen, C., Obrdlik, P. & Harter, K. in *Plant Signal Transduction* Vol. 479 *Methods in Molecular Biology* (ed Thomas Pfannschmidt) Ch. 14, 217-233 (Humana Press, 2009).

16 Lauber, M. H. *et al.* The Arabidopsis KNOLLE Protein Is a Cytokinesis-specific Syntaxin. *The Journal of Cell Biology* **139**, 1485-1493, doi:10.1083/jcb.139.6.1485 (1997).

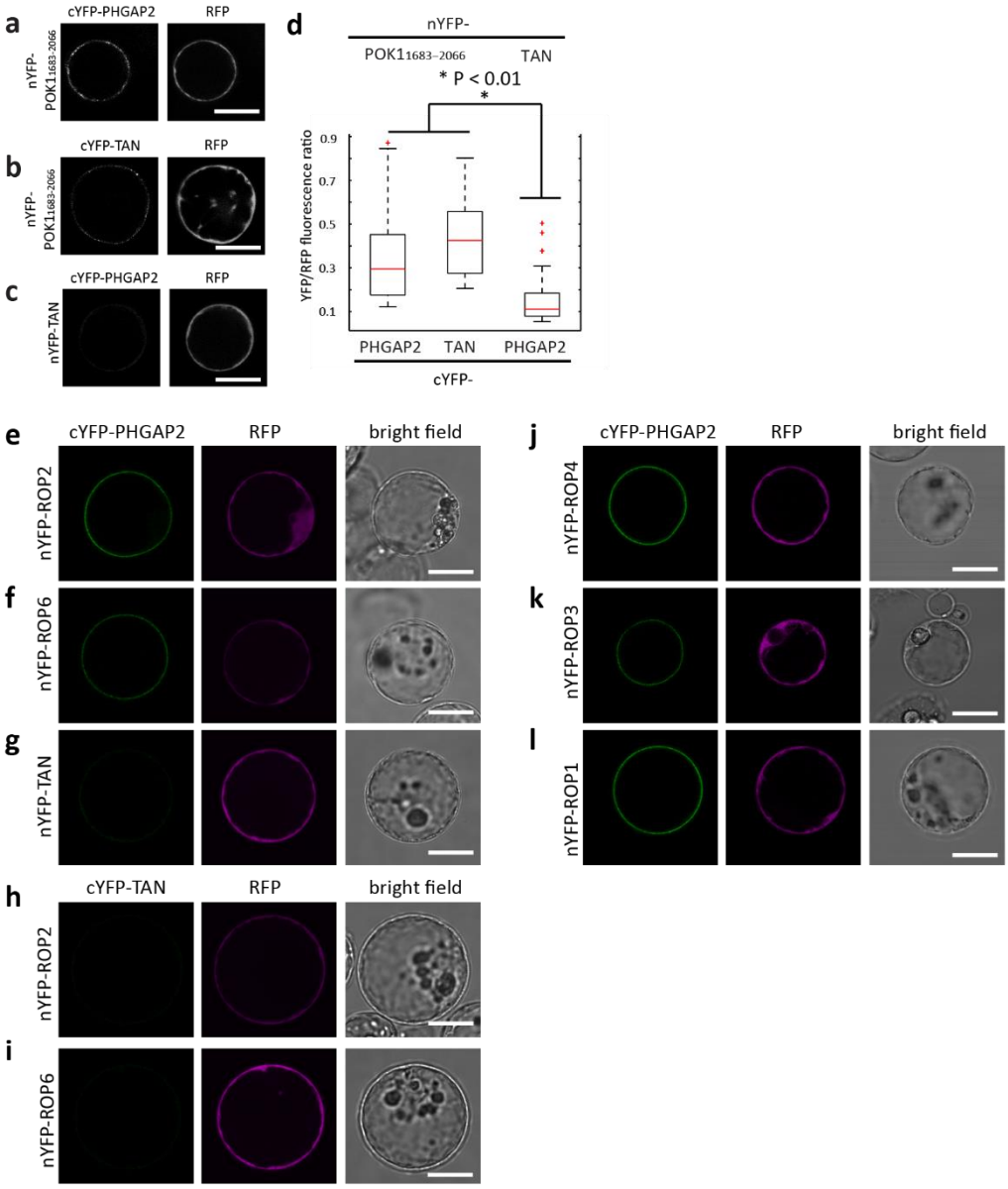

Supplemental Figure S1: Interaction assays. (a to c) Ratiometric bimolecular fluorescence complementation (rBiFC) analysis in *Arabidopsis thaliana* protoplasts assaying the interaction between (a) POK1$_{1683-2066}$ and PHGAP2, as well as (b) POK1$_{1683-2066}$ and its *bona fide* interactor TANGLED (TAN). (c) No n/cYFP complementation is observed between TAN and PHGAP2, serving as a biological negative control. Images in left panels show single optical sections of n/cYFP fluorescence. Right panels show cytoplasmic RFP fluorescence, co-expressed from the same plasmid like nYFP and cYFP-fusion proteins. (d) Boxplot of mean YFP fluorescence intensities ratioed against mean RFP fluorescence intensities (YFP/RFP fluorescence intensity). Boxplot depicts mean YFP/RFP fluorescence intensity ratio between POK1$_{1683-2066}$ and PHGAP2 (n = 27), POK1$_{1683-2066}$ and TAN (n = 30) and between PHGAP2 and TAN (n = 41). Significant differences (*P<0.01) between mean fluorescence intensity ratios were determined by One Way Anova. (e to i) Images correspond to samples in Figure 1d, 1e, 1f, 1h, 1i, but include the respective RFP images. Image acquisition and quantification was performed as previously described [1]. (j to l) BiFC and corresponding RFP and bright field images of *Arabidopsis thaliana* protoplasts. n/cYFP fluorescence indicating interaction between (j) ROP4 and PHGAP2, (k) ROP3 and PHGAP2 and (l) ROP1 and PHGAP2. Scale bars indicate 20 µm. Each protoplast represents an independent transformation event. Boxplot was assembled in MATLAB.

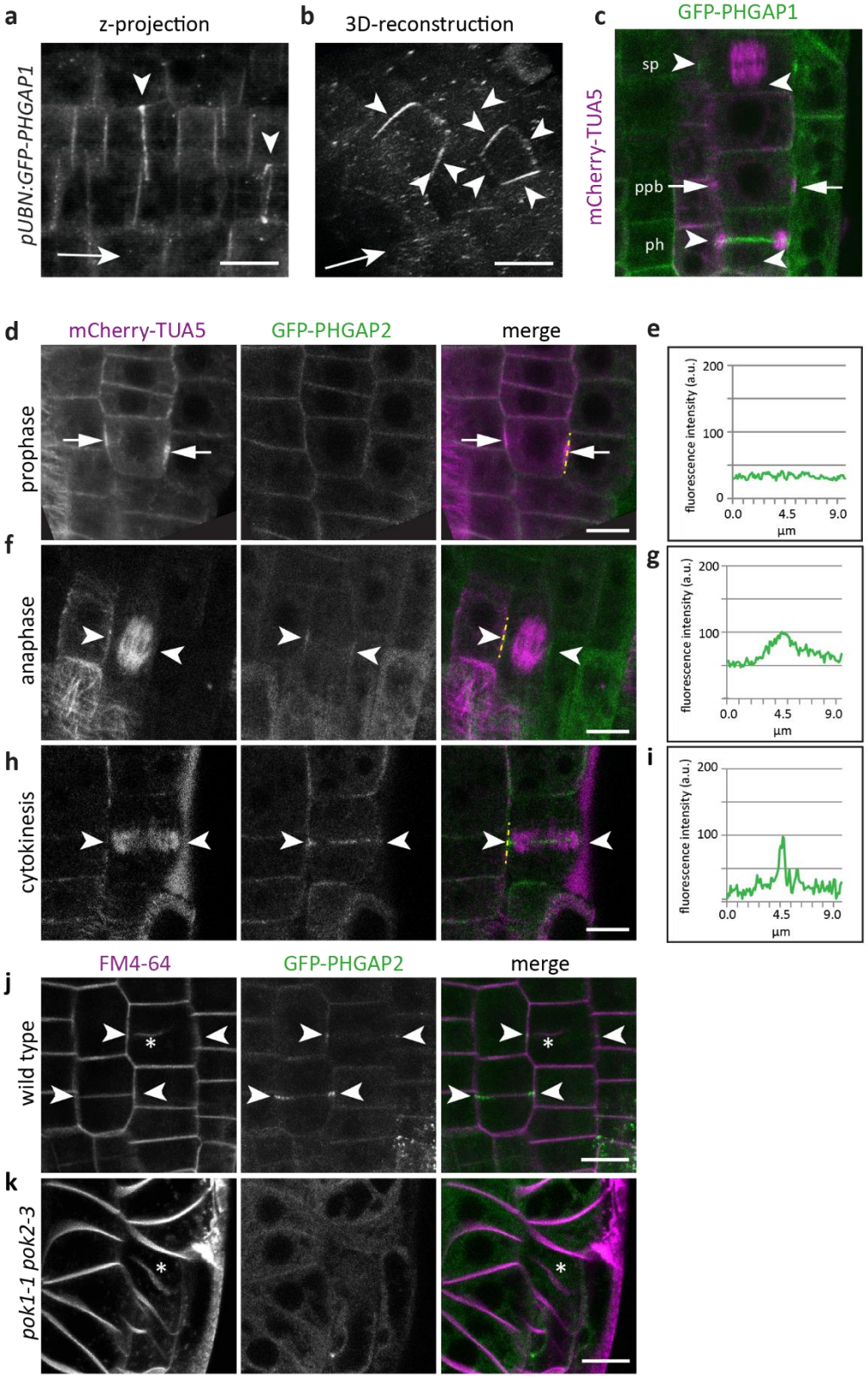
a
z-projection
pUBN:GFP-PHGAP1
b
3D-reconstruction
c
GFP-PHGAP1
mCherry-TUA5
sp
ppb
ph
d
mCherry-TUA5
GFP-PHGAP2
merge
prophase
e
fluorescence intensity (a.u.)
200
100
0
0.0
4.5
9.0
µm
f
anaphase
g
h
cytokinesis
i
FM4-64
j
wild type
k
pok1-1 pok2-3

Supplemental Figure S2: PHGAP localization and POK-dependency. (a, b) Root meristem cells expressing *pUBN:GFP-PHGAP1*. (a) GFP-PHGAP1 is present in the cytoplasm, associates with the plasma membrane and (b) accumulates in a continuous ring-like pattern (3D-reconstruction, arrows point out ring-shape. (c) Root meristem cells co-expressing *pUBN:GFP-PHGAP1* and the microtubule reporter construct *35S:mCherry-TUA5*. Mitotic figures are indicated. Note that only PPB is not associated with GFP-PHGAP1, while cells with spindle and phragmoplast display GFP-PHGAP1. (d,f,h) Root meristem cells co-expressing *pUBN:GFP-PHGAP2* and the microtubule reporter construct *35S:mCherry-TUA5*. (e) Plot profile of GFP-PHGAP2 intensity along dashed, yellow line in (d, merge). Note the uniform GFP-PHGAP2 intensity. (f) PHGAP2 accumulation (arrow heads) in cell with spindle. (g) Plot profile of PHGAP2 corresponding to yellow line in merge panel of (f). Note the shallow arch of GFP-PHGAP2 fluorescence intensity. (h) PHGAP2 accumulation (arrow head) in cytokinetic cell displaying phragmoplast. (i) Plot profile of PHGAP2 corresponding to yellow line in merge panel of (h). Note the GFP-PHGAP2 intensity peak. (j and k) Root meristem cells expressing *pUBN:GFP-PHGAP2*, stained with the endocytic sterol dye FM4-64 (Molecular Probes) to visualize cell walls and cell plates. (j) GFP-PHGAP2 accumulates at the cortical division site (arrow heads) in cytokinesis. Asterisk indicates the developing cell plate. (k) GFP-PHGAP2 localizes to cytoplasm and plasma membrane, but does not accumulate in a ring-pattern in a cytokinetic cell forming a new cell plate (asterisk). Scale bars indicate 10 µm. Relates to Figure 2.

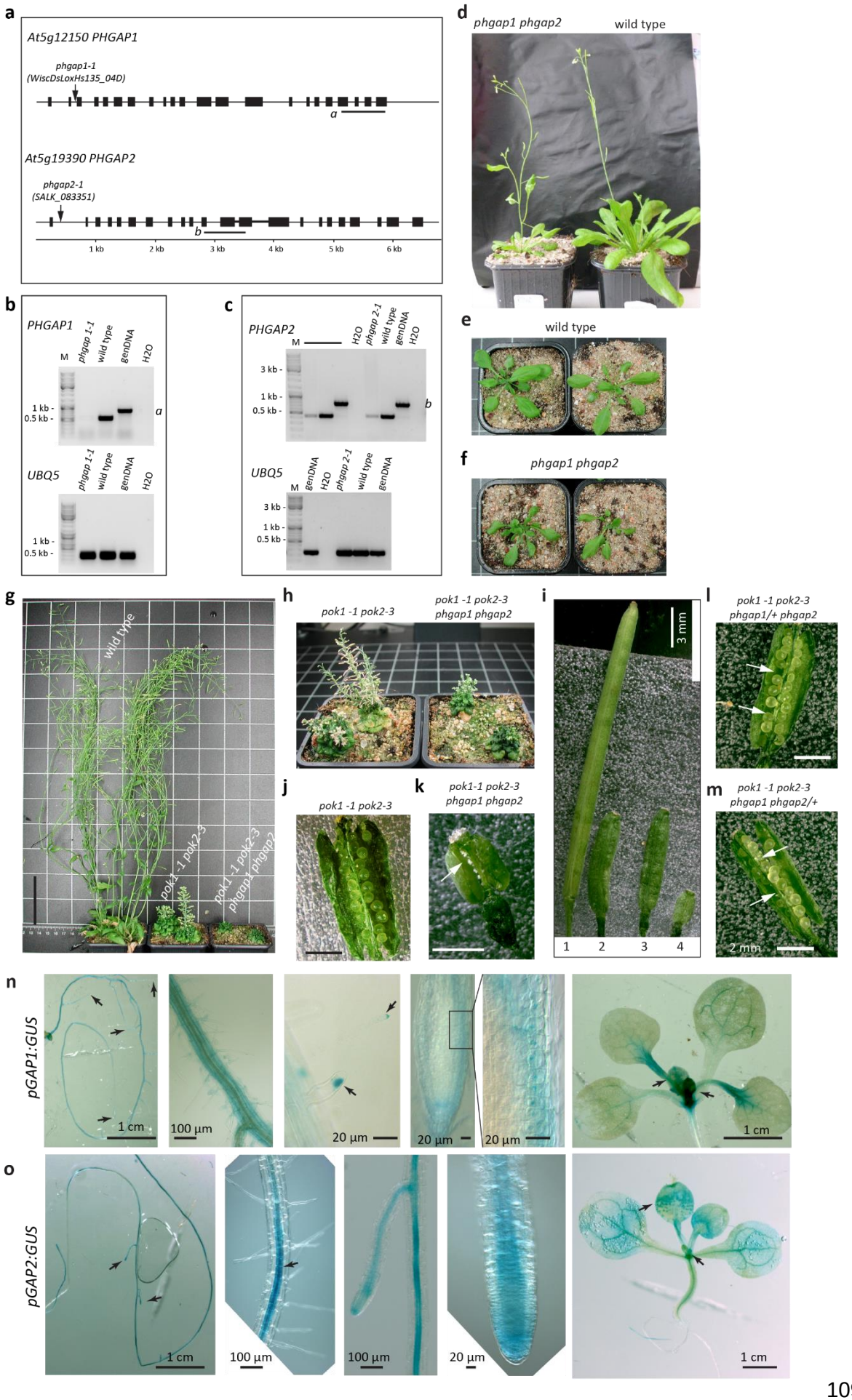
a
At5g12150 PHGAP1
phgap1-1
(WiscDsLoxHs135_04D)
a
At5g19390 PHGAP2
phgap2-1
(SALK_083351)
b
1 kb
2 kb
3 kb
4 kb
5 kb
6 kb
b
PHGAP1
M
phgap 1-1
wild type
genDNA
H2O
1 kb -
0.5 kb -
a
UBQ5
c
PHGAP2
M
H2O
phgap 2-1
wild type
genDNA
3 kb -
1 kb -
0.5 kb -
b
UBQ5
d
phgap1 phgap2
wild type
e
wild type
f
phgap1 phgap2
g
wild type
pok1 -1 pok2-3
pok1 -1 pok2-3
phgap1 phgap2
h
pok1 -1 pok2-3
pok1 -1 pok2-3
phgap1 phgap2
i
3 mm
1
2
3
4
l
pok1 -1 pok2-3
phgap1/+ phgap2
j
pok1 -1 pok2-3
k
pok1-1 pok2-3
phgap1 phgap2
m
pok1 -1 pok2-3
phgap1 phgap2/+
2 mm
n
pGAP1:GUS
1 cm
100 µm
20 µm
20 µm
20 µm
1 cm
o
pGAP2:GUS
1 cm
100 µm
100 µm
20 µm
1 cm

Supplemental Figure S3: Schematic representation of gene organization and position of T-DNA insertion sites. *PHGAP1* (At5g12150) and *PHGAP2* (At5g19390) gene organization is depicted and exons are indicated by bars. Respective positions of T-DNA insertions are specified by arrows. (b and c) Gel electrophoresis images of semi-quantitative RT-PCR comparing transcript levels of *phgap* mutant alleles and wild type. (b) For transcript amplification of *PHGAP1,* primer combinations (*a*), indicated in (a) were utilized. (c) *PHGAP2* amplification was accomplished using primers PHGAP2 01F and PHGAP2 01R (*b*), indicated in (a). Note that *PHGAP2* transcript was greatly reduced but not abolished. Genomic DNA (genDNA) and H_2O served as positive and no-template control for the PCR reactions, respectively. Amplification of *UBIQUITIN* (*UBQ*) *5* gene using primers NUBQ and CUBQ [2] served as loading control. cDNA synthesis was performed as described previously [2]. (g) Overview of wild type plants, *pok1-1 pok2-3* double mutant plants and *pok1-1 pok2-3 phgap1 phgap2* quadruple mutant plants at the same age. (h) Adult *pok1-1 pok2-3* double and *pok1-1 pok2-3 gap1 gap2* quadruple mutants. (i) Comparison of silique size (1) wild type, (2) *pok1-1 pok2-3* mutant, (3) *pok1-1 pok2-3 phgap1 phgap2/+* sesqui-mutant and (4) *pok1-1 pok2-3 phgap1 phgap2* quadruple mutant. (j to m) Comparison of the seed set in siliques. (j) *pok1-1 pok2-3* double mutant displays abnormally round, fertilized ovules. (k) Non-fertilized ovules (arrow) in silique of infertile *pok1-1 pok2-3 phgap1 phgap2* quadruple mutant. (l) *pok1-1 pok2-3 phgap1/+ phgap2* and (m) *pok1-1 pok2-3 phgap1 phgap2/+* sesqui-mutants. Arrows point out gaps in seed set, indicative of aborted ovules. Scale bars indicate 6 cm in (g), 2 mm in (j, k, l, m). (n and o) Analysis of gene expression patterns in lines expressing *PHGAP* promoter:*β*-Glucuronidase (GUS). (n) *PHGAP1* gene expression: GUS reporter gene expression was observed in elongated primary and lateral roots and in root hairs. In root meristems *PHGAP1:*GUS expression was predominant in the (e) epidermal and cortex cell files (zoom in of boxed area). In addition, GUS expression was evident in young leaf tissues and in the leaf vasculature. (o) *pPHGAP2*:GUS expression. In *pPHGAP2:*GUS lines, GUS reporter gene expression was evident in the root meristem and along the entire root system. Above the root meristem, expression becomes restricted to the vasculature in elongated and meristematic tissue. GUS expression was also prominent in young leaf tissues and in the leaf vasculature. While three hours of substrate incubation sufficed for strong staining in case of *pPHGAP2:GUS*, the samples expressing *pPHGAP1:GUS* were incubated for three days resulting in faint staining. Cloning into pWD137 and analysis was performed as previously described [2-4]. Images were taken at a Zeiss Axiophot.

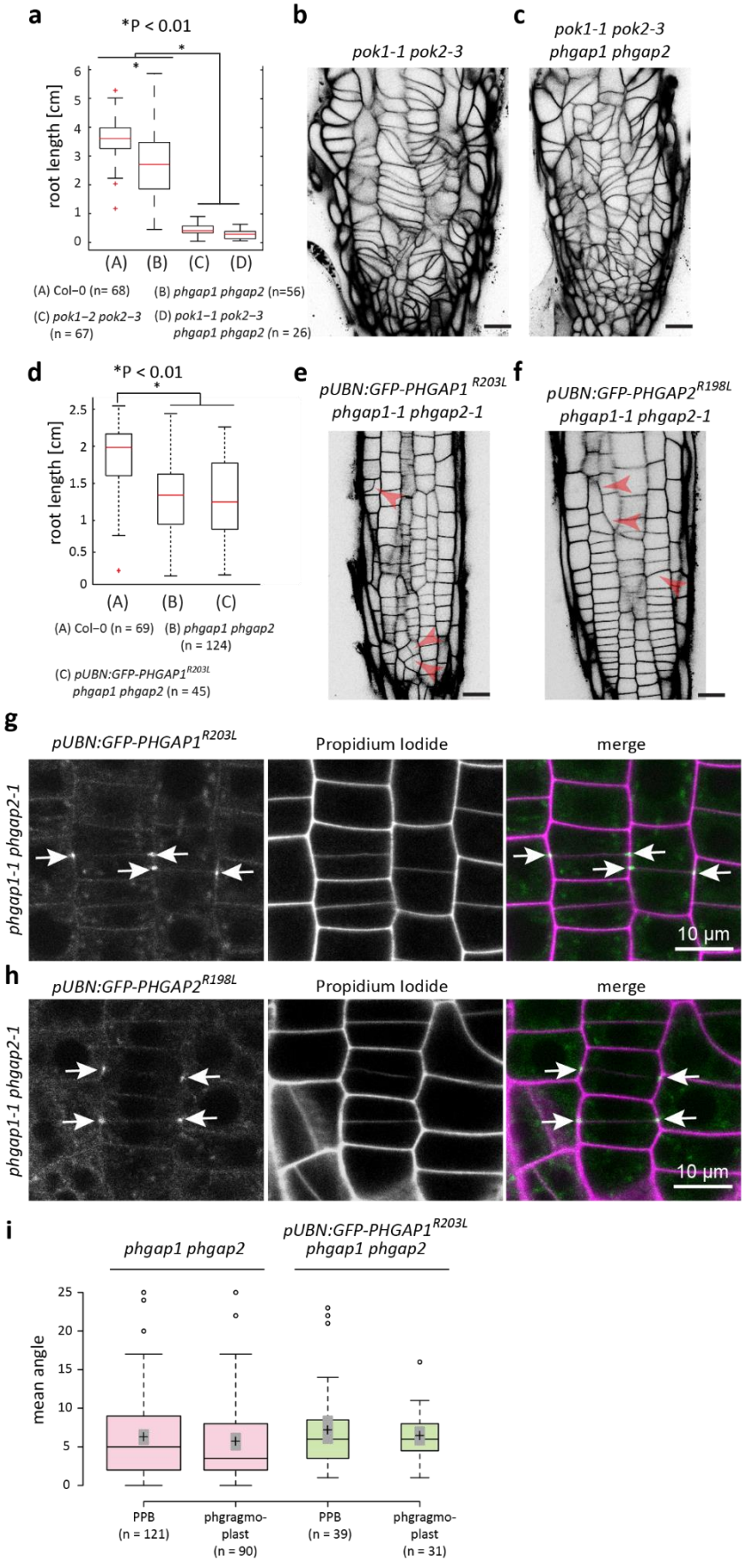
a
*P < 0.01
root length [cm]
(A) (B) (C) (D)
(A) Col–0 (n= 68)
(B) phgap1 phgap2 (n=56)
(C) pok1–2 pok2–3 (n = 67)
(D) pok1–1 pok2–3 phgap1 phgap2 (n = 26)
b
pok1-1 pok2-3
c
pok1-1 pok2-3 phgap1 phgap2
d
*P < 0.01
root length [cm]
(A) (B) (C)
(A) Col–0 (n = 69)
(B) phgap1 phgap2 (n = 124)
(C) pUBN:GFP-PHGAP1R203L phgap1 phgap2 (n = 45)
e
pUBN:GFP-PHGAP1 R203L phgap1-1 phgap2-1
f
pUBN:GFP-PHGAP2R198L phgap1-1 phgap2-1
g
pUBN:GFP-PHGAP1R203L
Propidium Iodide
merge
phgap1-1 phgap2-1
10 µm
h
pUBN:GFP-PHGAP2R198L
Propidium Iodide
merge
phgap1-1 phgap2-1
10 µm
i
phgap1 phgap2
pUBN:GFP-PHGAP1R203L phgap1 phgap2
mean angle
PPB (n = 121)
phgragmo-plast (n = 90)
PPB (n = 39)
phgragmo-plast (n = 31)

Supplemental Figure S4: Phenotype comparison. (a) Boxplot of primary root growth (10 day old seedlings) as indicated. Wild type (Col-0, A, mean 3.6 cm ± 0.7 STD) and *phgap1 phgap2* (B, mean 2.6 cm ± 1.2 STD) double mutants differ significantly in their root length (*P<0.01) and both, Col-0 and *phgap1 phgap2* are significantly (*P<0.01) different from *pok1-1 pok2-3* (C, mean 0.4 cm ± 0.2 STD) and *pok2-1 pok2-3 phgap1 phgap2* (D, mean 0.3 cm ± 0.2 STD) quadruple mutants. Significance was determined using One Way ANOVA. (b) Cell wall pattern of *pok1-1 pok2-3* root meristem. (c) Cell wall pattern of *pok2-1 pok2-3 phgap1 phgap2* quadruple mutant. (d) Boxplot of root growth of 7 day old seedlings as indicated. Wild type (A, mean 1.9 cm ± 0.4 STD) differs significantly (*P<0.01) from *phgap1 phgap2* (B, mean 1.3 cm ± 0.5 STD) and *pUBN:GFP-PHGAP1^{R203L};phgap1 phgap2* (C, mean 1.3 cm ± 0.5 STD). Significance was determined using One Way ANOVA. (e and f) Cell wall pattern of root meristems expressing either (e) *pUBN:GFP-PHGAP1^{R203L}* or (f) *pUBN:GFP-PHGAP2^{R198L}* in *phgap1 phgap2* double mutant. Arrow heads indicate examples of cell wall miss-positioning. (g and h) Root meristem cells expressing either (g) *pUBN:GFP-PHGAP1^{R203L}* or (h) *pUBN:GFP-PHGAP2^{R198L}* in *phgap1 phgap2* double mutant. Note that GFP-PHGAP1^{R203L} and GFP-PHGAP2^{R198L} still locate to the cortical division site (CDS) in *phgap1 phgap2* mutants. (i) Mean deviation angle of PPBs and phragmoplast in *phgap1 phgap2* (corresponds to data shown in Figure 4i and 4j) and *GFP-PHGAP1^{R203L} phgap1 phgap2* are not significantly different. One Way Anova, post-hoc Turkey HSD P ≥ 0.39 - 0.9. Boxplots were assembled in MATLAB and BoxPlotR (http://boxplot.tyerslab.com/).